



Classe di Scienze

PhD Thesis

A BIOPHYSICAL APPROACH TO THE STUDY
OF LIVING β -CELLS

Candidate:

Gianmarco Ferri

Supervisor:

Prof. F. Cardarelli

2019/2020

CONTENTS

List of Figures	vi
List of Tables	viii
Nomenclature	xiii
Foreword: a global emergency targeted...at the nanoscale	1
1 β -CELL FUNCTION: THE NEED FOR NEW BIOPHYSICAL APPROACHES	5
1.1 At the center of stage: the β -cell.	5
1.1.1 Inside the β -cell: insulin maturation steps.	7
1.1.2 The insulin secretory granule: more than merely a container.	9
1.2 From structure to function.	9
1.2.1 Step-1: a cascade of metabolic reactions transforms glucose in a trigger signal.	12
1.2.2 Step-2: ISGs mobilization and exocytosis.	12
1.3 Approaching the β -cell by quantitative biophysics.	14
1.3.1 Metabolic imaging of β -cells in physiology and disease: a new label-free paradigm.	14
1.3.2 Spatiotemporal fluctuation spectroscopy as a fast and robust screening method to study granule structural and dynamic properties.	16
2 PHASOR FLIM ANALYSIS OF β -CELL METABOLIC RESPONSE.	21
2.1 Imaging of NAD(P)H autofluorescence.	21
2.2 Phasor-FLIM approach to NAD(P)H-based metabolic fingerprint.	23
2.3 Experimental model of β -cells.	27
2.4 The β -cell metabolic status.	28
2.4.1 Preliminary fluorescence intensity analysis of NAD(P)H species in INS-1E cells.	28
2.4.2 FLIM analysis of NAD(P)H species in INS-1E cells in response to glucose stimulation.	30
2.4.3 The characteristic metabolic signature of the β -cells.	31
2.5 Effect of β -cell exposure to chronic hyperglycemic conditions.	34

- 2.5.1 Reduced response to glucose stimulation under hyperglycemic conditions correlates with production of intracellular oxidative stress. 35
- 2.6 Concluding remarks 35
- 3 IMSD ANALYSIS OF FLUORESCENTLY-LABELLED INSULIN GRANULES. 41
 - 3.1 Fluorescence correlation spectroscopy techniques. 42
 - 3.2 The *i*MSD approach. 43
 - 3.2.1 *i*MSD extracted parameters. 43
 - 3.2.2 Application of *i*MSD: from molecules to proteins, from nanoparticles to organelles. 46
 - 3.3 Application of *i*MSD to insulin secretory granules. 46
 - 3.3.1 Workflow of the experiment. 47
 - 3.3.2 The importance of temporal resolution and pixel size. 49
 - 3.4 The *i*MSD-based ISG structural-dynamic fingerprint. 51
 - 3.5 Fingerprint validation. 55
 - 3.5.1 Validation of *i*MSD by standard SPT analysis. 55
 - 3.5.2 Validation of *i*MSD-derived granule size by TEM. 58
 - 3.5.3 Functional validation of *i*MSD-derived parameters: glucose stimulation. 59
 - 3.5.4 Functional validation of *i*MSD-derived parameters: cholesterol overloading. 60
 - 3.6 Concluding Remarks. 62
- 4 EFFECT OF FLUORESCENCE LABELLING ON GRANULE PROPERTIES. 63
 - 4.1 Proteins used as molecular markers of ISGs. 64
 - 4.1.1 IAPP. 64
 - 4.1.2 Syncollin. 64
 - 4.1.3 Phogrin. 65
 - 4.2 *i*MSD based approach to compare ISGs' labelling strategies. 65
 - 4.3 Phogrin overexpression effect: possible explanations. 72
 - 4.4 Which future for label-free imaging of ISGs in living matter? 76
 - 4.4.1 Comparison between the light scattering properties of ISGs and lysosomes. 77
 - 4.5 Concluding remarks. 78

5	TOWARDS MULTIPLEXED BIOPHYSICAL ANALYSES IN THE LIVING ISLET.	83
5.1	Phasor-FLIM analysis on HIs.	84
5.1.1	Characterization of autofluorescence signal and lifetime in isolated human pancreatic islets.	84
5.2	Structural-dynamic fingerprint of ISGs in dispersed HI cells.	87
5.3	Concluding Remarks.	90
A	MATERIALS AND METHODS	93
A.1	Cell cultures.	93
A.2	Transfections and plasmids.	93
A.3	Human pancreatic islets cells.	94
A.4	Cellular staining.	95
A.5	Drugs treatments.	95
A.6	Insulin secretion assay.	95
A.7	Fluorescence confocal microscopy.	95
A.8	<i>i</i> MSD analysis.	96
A.9	Cluster similarity analysis.	97
A.10	Fluorescence-based expression level analysis.	99
A.11	Trajectory analysis.	99
A.12	Granule morphometric analysis from TEM micrographs.	99
A.13	Two-photon microscopy and phasor-FLIM measurements.	100
A.14	Data analysis on FLIM data.	100
A.15	Cross-STICS analysis.	101
B	<i>i</i> MSD PLOT: Y-AXIS INTERCEPT AND OBJECT SIZE	103
B.1	Instrumental waist.	103
B.2	Intercept of the <i>i</i> MSD curve.	103
B.3	Contribution of the particle size.	104
	BIBLIOGRAPHY	107

LIST OF FIGURES

Figure 1.1	Schematic representation of islet and pancreas cell types	6
Figure 1.2	Insulin maturation steps	8
Figure 1.3	The insulin secretory granule	10
Figure 1.4	β -cell functions	11
Figure 1.5	Granules' pools and biphasic insulin secretion	13
Figure 1.6	ISGs mobilization	15
Figure 1.7	Experimental approaches	18
Figure 2.1	Cellular autofluorescence spectra	22
Figure 2.2	Scheme of NAD(H) fractions upon metabolic changes	24
Figure 2.3	Phasor plot principles	25
Figure 2.4	Phasor-FLIM measurement on a NADH solution	26
Figure 2.5	Autofluorescence intensity analysis	29
Figure 2.6	NAD(P)H intensity and insulin secretion	30
Figure 2.7	Phasor-FLIM analysis	32
Figure 2.8	Segmentation analysis on INS-1E cells upon glucose stimulation	33
Figure 2.9	Phasor coordinates shift in different cell lines	34
Figure 2.10	Phasor FLIM analysis on hyperglycemic culturing condition	36
Figure 2.11	Segmentation analysis on INS-1E cells pre-incubated in hyperglycemic conditions	37
Figure 2.12	LSS species as oxidative stress signature induced by hyperglycemia	38
Figure 2.13	Model for coupling of glucose metabolism to insulin secretion	40
Figure 3.1	FCS principle	42
Figure 3.2	<i>i</i> MSD workflow	45
Figure 3.3	From time-lapse imaging to the <i>i</i> MSD of ISGs in living cells	48
Figure 3.4	Bleaching profile	49
Figure 3.5	D_M depending on the analyzed time window	50
Figure 3.6	Impact of scan speed on <i>i</i> MSD extracted size	52

Figure 3.7	From single <i>i</i> MSD traces to whole-cell-population analysis	53
Figure 3.8	C-peptide-EGFP labelled ISGs fingerprint	54
Figure 3.9	Example of typical acquisition of transfected ISGs	57
Figure 3.10	Impact of high mobility and brighter granules on <i>i</i> MSD analysis	58
Figure 3.11	TEM micograph of ISGs	59
Figure 3.12	Effect of glucose stimulation on ISG fingerprint	60
Figure 3.13	Effect of cholesterol overload on ISG fingerprint	61
Figure 4.1	<i>i</i> MSD derived parameters of IAPP-FP and Syncollin-FP labelled ISGs	66
Figure 4.2	Fingerprints of IAPP-FP and Syncollin-FP labelled ISGs	67
Figure 4.3	<i>i</i> MSD derived parameters of phogrin-FP labelled ISGs	69
Figure 4.4	Fingerprints of phogrin-FP labelled ISGs	70
Figure 4.5	fingerprint of cotransfected cells	71
Figure 4.6	Fluorescence expression level analysis of stably transfected cells	72
Figure 4.7	Actin cytoskeleton	73
Figure 4.8	Fingerprint of Latrunculin-B treated C-peptide-EGFP ISGs	74
Figure 4.9	Insulin secretion analysis	76
Figure 4.10	Backscattering analysis	77
Figure 4.11	Cross-correlation analysis	79
Figure 4.12	Amino acidic structure of insulin	80
Figure 5.1	Phasor FLIM analysis on HIs	85
Figure 5.2	Emission spectra of autofluorescence species	86
Figure 5.3	Phasor FLIM analysis on lipofuscin contribution	88
Figure 5.4	<i>i</i> MSD-based screening of ISGs in dispersed human β -cells	89
Figure B.1	PSF profiles	104
Figure B.2	Gaussian fitting and PSF profiles	105

LIST OF TABLES

Table 3.1	Summary of <i>i</i> MSD-derived parameters	55
Table 4.1	Summary of <i>i</i> MSD-derived parameters for chimeric FP used to labelled ISGs	66
Table 4.2	Summary of <i>i</i> MSD-derived parameters for Latrunculin-B treated cells	75
Table 4.3	Optical properties of the principal fluorescent amino acids	81
Table 5.1	Summary of <i>i</i> MSD-derived parameters for HIs	90

LIST OF PUBLICATIONS

Articles in peer-reviewed journals included in this Thesis:

1. **Ferri, G**, Digiacomio, L., D’Autilia, F., Durso, W., Caracciolo, G. & Cardarelli, F. Time-lapse confocal imaging datasets to assess structural and dynamic properties of subcellular nanostructures. eng. *Scientific Data* **5**, 180191 (2018).
2. **Ferri, G**, Bugliani, M., Marchetti, P. & Cardarelli, F. Probing the light scattering properties of insulin secretory granules in single live cells. *Biochemical and Biophysical Research Communications* **503**, 2710 (2018).
3. **Ferri, G**, Digiacomio, L., Lavagnino, Z., Occhipinti, M., Bugliani, M., Cappello, V., Caracciolo, G., Marchetti, P., Piston, D. W. & Cardarelli, F. Insulin secretory granules labelled with phogrin-fluorescent proteins show alterations in size, mobility and responsiveness to glucose stimulation in living β -cells. *Scientific Reports* **9** (2019).
4. **Ferri, G**, Tesi, M., Massarelli, F., Marselli, L., Marchetti, P. & Cardarelli, F. Metabolic response of Insulinoma 1E cells to glucose stimulation studied by fluorescence lifetime imaging. *accepted by Faseb BioAdvances* (2020).

Articles not included in this Thesis:

1. Palchetti, S., Digiacomio, L., Giulimondi, F., Pozzi, D., Peruzzi, G., **Ferri, G**, Amenitsch, H., Cardarelli, F., Mahmoudi, M. & Caracciolo, G. A mechanistic explanation of the inhibitory role of the protein corona on liposomal gene expression. *Biochimica et Biophysica Acta (BBA) - Biomembranes* **1862**, 183159 (2020).
2. Quagliarini, Di Santo, Palchetti, **Ferri, G**, Cardarelli, Pozzi & Caracciolo. Effect of Protein Corona on The Transfection Efficiency of Lipid-Coated Graphene Oxide-Based Cell Transfection Reagents. *Pharmaceutics* **10**, 11 (2020).

3. Moliterni, A., Altamura, D., Lassandro, R., Olieric, V., **Ferri, G.**, Cardarelli, F., Camposeo, A., Pisignano, D., Anthony, J. & Giannini, C. Synthesis, crystal structure, polymorphism and microscopic luminescence properties of anthracene derivative compounds. *Acta Crystallographica Section B: Structural Science, Crystal Engineering and Materials* **2**, 15 (2020).

Conference contributions:

5. Ferri, G. *Probing nucleocytoplasmic transport impairment upon defective nuclear lamina assembly.* in *Oral presentation* Sept. 8–11, 2013 (Methods and Application in Fluorescence MAF, Genova, Italy).
6. Ferri, G. *Probing the dynamic fingerprint of insulin secretory granules in living cells by spatiotemporal fluctuation spectroscopy.* in *Poster* May 18–19, 2017 (Biophysics @ Rome, Rome, Italy).
7. Ferri, G. *Probing the dynamic fingerprint of insulin secretory granules in living β -cells by spatiotemporal fluctuation spectroscopy.* in *Oral presentation* Oct. 1–5, 2018 (EASD, European Association for the Study of Diabetes., Berlin, Germany).
8. Ferri, G. *Effects of GLP-1R agonists on beta cell survival, function and granule motility.* in *Oral presentation* Sept. 16–19, 2019 (EASD, European Association for the Study of Diabetes., Barcelona, Spain).
9. Ferri, G. *2nd Practical Workshop on Advanced Microscopy.* in *Workshop* Dec. 1–4, 2015 (Nikon Center, IIT, Genova, Italy).
10. Ferri, G. *Corso di orientamento federato SNS, IUSS, Sant'Anna* in *Seminario* July 4, 2018 (Orientamento, San Miniato, Italy).
11. Ferri, G. *Probing the dynamic fingerprint of insulin secretory granules in living cells by spatiotemporal fluctuation spectroscopy.* in *Poster* May 6–8, 2019 (Quantitative Aspects of Membrane Fusion and Fission, Padova, Italy).
12. Ferri, G. *Screening delle proprietà strutturali e dinamiche del granulo di insulina in cellule vive* in *Poster* May 16–19, 2018 (Congresso nazionale SID, Società italiana di Diabetologia, Rimini, Italy).
13. Ferri, G. *Microscopia ottica non invasiva rivela la traiettoria metabolica di cellule INS-1E stimulate con glucosio* in *Poster* Dec. 1–5, 2020 (Congresso nazionale SID, Società italiana di Diabetologia, Rimini, Italy).

14. Ferri, G. *Phasor-FLIM analysis of β -cell metabolic trajectory upon glucose stimulation* in Submitted Sept. 21–25, 2020 (EASD, European Association for the Study of Diabetes., Wien, Austria).

NOMENCLATURE

		FLIM	Fluorescence lifetime imaging microscopy; an imaging technique for producing an image based on the differences in the exponential decay rate of the fluorescence from a fluorescent sample. It can be used as an imaging technique in confocal microscopy, two-photon excitation microscopy, and multiphoton tomography.
ATP/ADP	Adenosine triphosphate/Adenosine biphosphate; a complex organic chemical that provides energy to drive many processes in living cells		
CHO	Chinese hamster ovary (CHO) cells; an epithelial cell line derived from the ovary of the Chinese hamster, often used in biological and medical research and commercially in the production of therapeutic proteins	FP	Fluorescent protein; a protein that exhibits bright fluorescence when exposed to visible light
		FWHM	Full width half maximum; an expression of the extent of function given by the difference between the two extreme values of the independent variable at which the dependent variable is equal to half of its maximum value
DMSO	dimethyl sulfoxide; organic solvent, readily passes through skin, cryoprotectant in cell culture		
ELISA	Enzyme-linked immunosorbent assay; an assay to detect the presence of a ligand (commonly a protein) in a liquid sample using antibodies directed against the protein to be measured	GSIS	Glucose stimulated insulin secretion; secretion of insulin from pancreatic β -cells mediated by a raising of glucose concentration in bloodstream
		HI	Human Islet; Langerhans Islet; regions of the pancreas that contain its endocrine (hormone-producing) cells, discovered in 1869 by German pathological anatomist Paul Langerhans. The pancreatic islets constitute 1 to 2% of the pancreas volume and receive 10–15% of its blood flow. The pancreatic islets are arranged in density routes throughout the human pancreas, and are important in the metabolism of glucose
ER	Endoplasmatic reticulum; a type of organelle found in eukaryotic cells that forms an interconnected network of flattened, membrane-enclosed sacs or tube-like structures known as cisternae		
FCS	Fluorescence Correlation Spectroscopy; a correlation analysis of fluctuation of the fluorescence intensity. The analysis provides parameters of the physics under the fluctuations. One of the interesting applications of this is an analysis of the concentration fluctuations of fluorescent particles (molecules) in solution	IAPP	Islet amyloid poli-peptide; is a 37-residue peptide hormone. It is cosecreted with insulin from the pancreatic β -cells in the ratio of approximately 100:1 (insulin:amylin). Amylin plays a

	role in glycemic regulation by slowing gastric emptying and promoting satiety, thereby preventing post-prandial spikes in blood glucose levels	mGPDH	(mitochondrial) Glycerol-3-phosphate dehydrogenase is an enzyme that catalyzes the reversible redox conversion of dihydroxyacetone phosphate into glycerol 3-phosphate using NADH as cofactor. It permits to transport reducing agents across the inner mitochondrial membrane as NADH that cannot cross the membrane alone but it can reduce another molecule that can cross the membrane, so that its electrons can reach the electron transport chain.
ICS	Image correlation spectroscopy; fluorescence correlation technique in which autocorrelation on an image is calculated		
IDF	International Diabetes Federation		
iMSD	image-Mena square displacement; a measure of the deviation of the position of a particle with respect to a reference position over time. It is the most common measure of the spatial extent of random motion, and can be thought of as measuring the portion of the system "explored" by the random walker	mMDH	(mitochondrial) Malate Dehydrogenase is an enzyme that reversibly catalyzes the oxidation of malate to oxaloacetate using the reduction of NAD ⁺ to NADH. Together with mGPDH act as mitochondrial NADH shuttle
INS-1E	Insulinoma (clone) 1E; laboratory cell-model used to study pathophysiology of β -cell	NAD(P)H	Nicotinamide adenine dinucleotide (phosphate); a cofactor found in all living cells. The compound is called a dinucleotide because it consists of two nucleotides joined through their phosphate groups. One nucleotide contains an adenine nucleobase and the other nicotinamide. Nicotinamide adenine dinucleotide exists in two forms: an oxidized and reduced form, abbreviated as NAD ⁺ and NADH respectively
ISG	Insulin secretory granule; a complex intracellular organelle of pancreatic β -cell comprised of a many proteins with different catalytic activities and messenger functions. It contains insulin molecule.		
ISI	Insulin stimulation index; index calculated by dividing secreted insulin concentration after glucose stimulation (at the 28 mM glucose) by secreted insulin concentration at resting condition (2.8 mM glucose)	PIP	Phosphatidylinositol phosphate; a phospholipid found in cell membranes that helps to recruit a range of proteins, many of which are involved in protein trafficking, to the membranes
LLS	Long lifetime species; chemical species characterized by high fluorescence lifetimes (i.e. 8 ns); marker of ROS-induced damages of membranous compartments	PMT	Photomultiplier tube; extremely sensitive detectors of light in the ultraviolet, visible, and near-infrared ranges of the electro-

	<p>magnetic spectrum. These detectors multiply the current produced by incident light by as much as 100 million times, enabling (for example) individual photons to be detected when the incident flux of light is low</p>		<p>individual particles within a medium. The coordinates time series, which can be either in two dimensions (x, y) or in three dimensions (x, y, z), is referred to as a trajectory. The trajectory is typically analyzed using statistical methods to extract information about the underlying dynamics of the particle</p>
PSF	<p>Point spread function; the response of an imaging system to a point source or point object. A more general term for the PSF is a system's impulse response, the PSF being the impulse response of a focused optical system</p>	SRP	<p>Signal recognition particle; an abundant, cytosolic, universally conserved ribonucleoprotein (protein-RNA complex) that recognizes and targets specific proteins to the endoplasmic reticulum in eukaryotes and the plasma membrane in prokaryotes</p>
PTP	<p>Protein tyrosine phosphatase; group of enzymes that remove phosphate groups from phosphorylated tyrosine residues on proteins</p>		
RICS	<p>Raster image correlation spectroscopy; a noninvasive technique to detect and quantify events in a live cell, including concentration of molecules and diffusion coefficients of molecules; in addition, by measuring changes in diffusion coefficients, RICS can indirectly detect binding</p>	STICS	<p>Spatio-temporal image correlation spectroscopy; fluorescence correlation technique used to study the spatio-temporal evolution on a system (i.e. fluorescent proteins inside a cell)</p>
		T1D e T2D	<p>Type 1 diabetes e Type 2 diabetes</p>
		TEM	<p>Transmission electron microscopy; a microscopy technique in which a beam of electrons is transmitted through a specimen to form an image. The specimen is most often an ultrathin section less than 100 nm thick or a suspension on a grid. An image is formed from the interaction of the electrons with the sample as the beam is transmitted through the specimen</p>
RRP	<p>Ready releasable pool; It is functionally defined as a small subset of the many vesicles in a cell that is more readily released than other vesicles</p>		
SCD	<p>Statistical cluster distance; a global statistical analysis on whole-cell-population data based on the Mahalanobis approach</p>		
SIM	<p>Structured illumination microscopy; a type of wide-field super-resolution microscopy</p>	TICS	<p>Temporal image correlation spectroscopy; fluorescence correlation technique used to study the temporal evolution on a system (i.e. fluorescent proteins inside a cell)</p>
SPT	<p>Single particle tracking; the observation of the motion of</p>		

TIRFM	Total internal reflection fluorescence microscope; is a type of microscope with which a thin region of a specimen, usually less than 200 nm can be observed	
TPEN	N,N,N,N-tetrakis pyridinylmethyl)	(2- -1,2- ethanediamine; an intracellular membrane-permeable ion chelator. TPEN has a high affinity for many transition metals and should not be considered specific or selective for a particular ion

FOREWORD: A GLOBAL EMERGENCY TARGETED...AT THE NANOSCALE

463 million people worldwide suffer from Diabetes (both type I and II), as reported in the 2019 report of the International Diabetes Federation (IDF) [1]. It is a growing trend that involves primarily low- and middle-income countries but it is a global emergency affecting the health of individuals, societies and economics [1]. At the center of stage, the β -cells. These specialized cells naturally present in the Langerhans Islets of mammalian pancreas exert the complex function of secreting insulin in response to an augmented concentration of glucose in the blood (glycaemia) and this happens through a tight regulation of key molecular processes. In brief, after being transported into the cell cytoplasm, glucose gets readily phosphorylated and metabolically digested during glycolysis; the products of glucose oxidation, such as pyruvate and Nicotinamide Adenine Dinucleotide in its reduced form (i.e. NADH), are shuttled together with others substrates into mitochondria by mitochondrial transporters to participate to the Krebs Cycle and produce large quantities of NADH. NADH then acts as a potent electron carrier (being oxidized into NAD⁺) during the mitochondrial oxidative phosphorylation, fueling the production of ATP molecules. Increased ATP/ADP ratio levels induce closure of plasma-membrane-associated ATP-sensitive potassium channels, which in turn induces depolarization of the plasma membrane and activation of voltage-sensitive calcium channels. Ca²⁺ influx finally promotes and sustain insulin secretion by mobilization of specialized organelles within β -cells, the insulin secretory granules (ISGs) from the cytoplasm to the fusion with the plasma membrane. ISGs, are approximately 300 nm in linear size and contain a core of insulin molecules densely packed into crystalline-like arrays. Their structural and dynamic properties such as size, speed, mode of motion, number, etc. are tightly regulated throughout the metabolic process described. Hence, to summarize, the β -cells orchestrate their peculiar response to glucose by (i) a cascade of fast metabolic reactions and, subsequently, (ii) granule activation towards secretion. It is clear that a quantitative description of these processes, possibly within living cells/tissues, would be crucial for our understanding of β -cell function in physiology and its alterations in pathology. In this context, it is not surprising that, among others, the European scientific community

1

envisioned a road-map in Diabetes research that points to a fundamental role of multidisciplinary, quantitative approaches for future investigations of β -cell (dis)function [2]. Along the same reasoning, the overriding goal of my PhD project is to apply and adapt methods and concepts from the field of quantitative biophysics and optical microscopy to the study of the β -cell and increase our understanding of two main pillars of its function, as already mentioned above: the metabolic response to glucose and the subsequent regulation of insulin granule structural and dynamic properties to exert secretion. More in detail:

- The metabolic response of β -cells upon glucose stimulation is monitored by Fluorescence Lifetime IMaging (FLIM) microscopy on the intrinsic signal coming from NAD(P)H molecules.
- Granule structural and dynamic properties are investigated by spatio-temporal fluctuation spectroscopy, in particular by means of a fluorescence based spatio-temporal fluctuation analysis algorithm (named image-derived Mean Square Displacement, or *iMSD*), that extracts the average size and dynamics of granules directly from imaging, with no need to preliminarily assume any interpretative model.

This Thesis is the result of my research activity at the NEST Laboratory of Scuola Normale Superiore in Pisa and has greatly benefited from the collaboration with Prof. Piero Marchetti and his research group at the Department of Clinical and Experimental Medicine (Islet Cell Laboratory) of University of Pisa and Cisanello Hospital. They provided cells and tissues, together with the fundamental expertise in the field of β -cell and Langerhans Islets physio-pathology. For the sake of clearness, the main results of this Thesis were divided into separate Chapters, each addressing a different aspect of the biophysical analyses proposed. In brief: **Chapter 1** presents an overview on β -cell biology and on the techniques available to study its key molecular aspects. The rationale behind my Thesis work is described in the final section of this Chapter.

Chapter 2 introduces the use of FLIM microscopy, coupled to phasor analysis, to study the β -cell metabolic response to glucose concentration. By means of Phasor-FLIM on NAD(P)H signal, is possible to quantify the ratio of protein-bound and free NAD(P)H and it can be used to follow the metabolic shift that the β -cell experiences during glucose stimulation, both in a normal condition and in presence of glucotoxicity induced by a hyperglycemic culturing condition (and simulating a T2D case).

The second pillar of this Thesis, the study of granule structural/dynamic properties, is addressed in **Chapter 3** and **Chapter 4**.

In detail, **Chapter 3** describes how we tuned the *iMSD* analysis to obtain a systematic study of granule size and motion in the cell cytoplasm. In particular, the optical microscopy acquisition parameters (i.e. frame rate, pixel size, etc) were optimized and validated by means of stimuli known to affect ISGs properties (e.g. cholesterol overload, glucose stimulation) and by comparing with results obtained by orthogonal well-established techniques used in the field (e.g. Electron Microscopy for structural details, Single particle Tracking for the analysis of granule dynamics).

Chapter 4 builds on what learned before to achieve a comprehensive *iMSD*-based view of granule properties upon using different fluorescent tags for labelling. A short list of chimeric fluorescent proteins (FP) used to label ISGs is available in literature, differentiated from being localized inside the granule lumen or trans-membrane. In this Chapter the main ones are compared in terms of their impact on granules properties. While *iMSD* analysis produces similar results for the luminal markers, the use of a trans-membrane marker, phogrin-FP, shows a clearly altered result. Phogrin over-expression induces a substantial granule enlargement and higher mobility, together with a partial de-polymerization of the actin cytoskeleton and a reduced cell responsiveness to glucose stimulation. FP over-expression related artifacts are often underestimated, but they can seriously compromise the obtaining of reliable data. A few perspectives to tackle the limitation associated to FP over-expression for ISGs imaging are discussed in the final section of the Chapter.

Finally, **Chapter 5** reports on the initial steps towards the application of all aforementioned biophysical tools in a new biological context, i.e. an entire, intact, human pancreatic islet. Preliminary measurements and future perspectives are presented in this Chapter.

All materials and methods are gathered in **Appendix A**. **Appendix B** contains supplementary information on *iMSD* analysis, including a detailed derivation of *iMSD* equations.

β -CELL FUNCTION: THE NEED FOR NEW BIOPHYSICAL APPROACHES

1.1 AT THE CENTER OF STAGE: THE β -CELL.

The β -cell is localized in the Langerhans Islets [3] of mammalian pancreas and exert the complex function of secreting the peptide hormone insulin in response to an augmented concentration of glucose in the bloodstream. This function is essential in maintaining glucose homeostasis, whose imbalance causes damages to tissues and organs throughout the body. Langerhans Islets belong to the so-called "endocrine pancreas" and can be defined as micro-organs interspersed among the "exocrine pancreas" [4], constituted by cells secreting digestive enzymes. Each Islet contains different cell types: α , β , δ , ϵ , and PP cells, categorized according to the type of secreted endocrine peptide hormone: 15–20% of cells are α -cells [5], 75–80% are β -cells, 5% are δ -cells [6], 1% are ϵ -cells, and 4% are PP cells [7]. α -cells secrete the hormone glucagon that, together with the insulin secreted by β -cells, control glucose homeostasis; δ -cells secrete somatostatin that inhibits the secretion of insulin and glucagon; ϵ -cells promote appetite and secrete ghrelin that inhibits insulin secretion; finally, PP cells secrete Pancreatic Peptide whose function is yet to be fully understood (Fig.1.1) [3, 8].

Of all these cell types, the insulin secreting β -cells have been the primary focus of research in decades due to their recognized central role in Diabetes mellitus. In Type 1 Diabetes (T1D), in fact, a cellular autoimmune response results in the specific destruction of β -cells and consequent loss of insulin secretion [10, 11]. In Type 2 Diabetes (T2D), by the other hand, defects in the actions of insulin generate the so-called "insulin resistance" pathological state, in which a sensibly higher concentration of insulin is required to maintain normal glucose homeostasis [12, 13]. T2D occurs only when insulin secretion becomes abnormal and/or the levels of secreted insulin are insufficient to compensate for the increased demand from other organs. Such deregulation of protein production is one of the factors contributing to the stress of β -cells and consequent cell death. The dysfunction of insulin secretion and associated hyperglycemia ultimately leads to micro- and macro-vascular damage, causing long-term complications

Schematic representation of islet and pancreas cell types

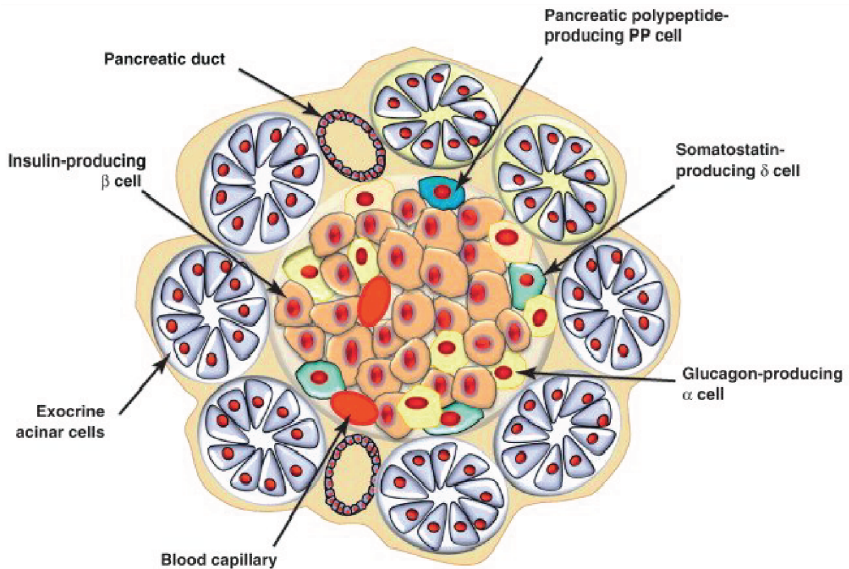


FIGURE 1.1: Most of the pancreatic tissue is composed of pancreatic acinar cells that produce digestive enzymes, which together with duct cells form the exocrine pancreas. The endocrine pancreas consists of four major cell types: α , β , δ and PP cells. These specialized cell types which are organized in compact islets secrete hormones into the bloodstream. The α and β cells that produce glucagon and insulin, respectively, regulate blood glucose levels. The δ and PP cells produce somatostatin and pancreatic polypeptide that modulate the secretory properties of the other cell types. *Adapted from Efrat and Russ (2012) [9].*

including neuropathy, nephropathy, retinopathy and cardiovascular disease that significantly affects quality of life and reduces life expectancy [14].

1.1.1 *Inside the β -cell: insulin maturation steps.*

A pancreatic β -cell acts, essentially, as a glucose sensor that responds to an acute hyperglycemic event (a temporary glycemic peak, typically postprandial) with the release of a dosed amount of insulin molecules, that are stored in specialized vesicles, produced and handled by the β -cell, the insulin secretory granules (ISGs) [15]. Each β -cell has an average volume of $763 \mu\text{m}^3$ and contains approximately 10,000 ISGs each with a diameter of around 300 nm [16]. Insulin molecules are packed into the granules during a maturation process, that starts, as for many other exocytosed vesicles, from the Golgi apparatus and ends with a mature ISG free in the cell cytoplasm and ready to be secreted [15].

In their mature form, ISGs contain a dense core composed of tightly packed crystals, composed by six molecules of insulin stabilized by the coordination of one calcium and two zinc ions [15, 17], in addition to a variety of soluble proteins and ions. Contextually to granule maturation, the insulin molecule undergoes several maturation steps too, that progressively change its structure and arrangement. First, pre-pro-insulin mRNA translation begins in the cytosol of pancreatic β -cells and consists of 110 amino acids (Fig. 1.2).

The immature peptide form, like most secreted proteins, contains an amino-terminal signal peptide (SP), which allows its interaction with ribonucleoprotein signal recognition particles (SRP) [19], followed by a B-chain, a C-chain (also known as C-peptide) and an A-chain. The signal peptide is recognized by the SRPs, which specifically translocate pre-pro-insulin across the membrane of the Endoplasmic Reticulum (ER). In the ER, the signal peptide is cleaved by signal peptidase to produce pro-insulin that has 86 amino acids consisting only of B-chain, C-peptide, and A-chain. Pro-insulin has three disulfide bonds in A6–A11, A7–B7, A20–B19 [20] and, within the ER, is finally folded through the concerted action of chaperone proteins and protein-thiol reductase. The molecule is then transported via repeated cycles of vesicle budding and fusion from the ER to the Golgi apparatus; within the trans Golgi network (TGN), pro-insulin is packaged along with multiple other components into nascent secretory granules (Fig. 1.2). As the immature granules bud from the TGN, the process of con-

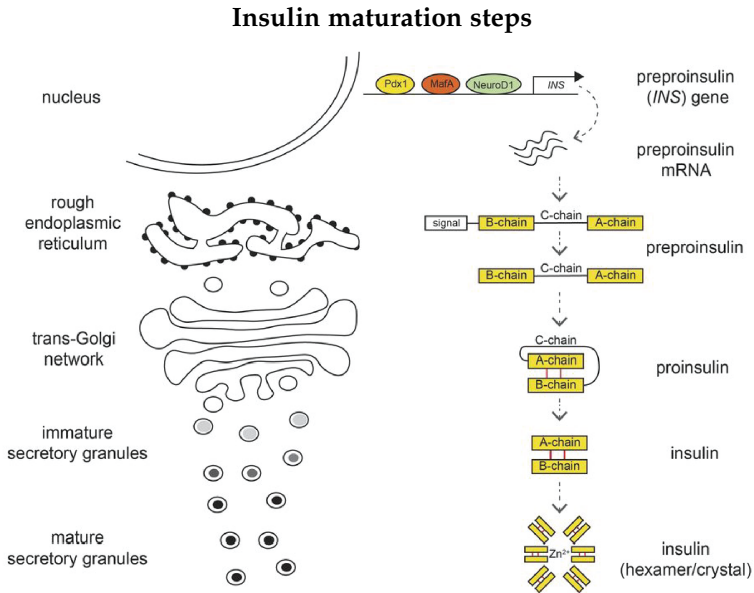


FIGURE 1.2: Insulin maturation along the granule secretory pathway. Pre-pro-insulin mRNA is transcribed from the *INS* gene and translated to pre-pro-insulin peptide. As this transits through the ER and TGN, the pre-pro-peptide is processed to its mature form and ultimately stored as hexameric insulin/ Zn^{2+} crystals within mature secretory granules. Adapted from *Tokarz (2018) [18]*.

densation and acidification [21] (priming) of the granule content begins along with the proteolytic conversion of pro-insulin and other intra-granule precursors to generate their mature forms [22, 23], ready to be secreted. In these final steps, pro-protein convertases (PC1/3) remove C-peptide from pro-insulin, originating mature insulin molecules composed only by A- and B-chains (Fig. 1.2). The maturation process impacts also ISGs size, since this process involves further condensation of the matrix constituents, reduction in granule diameter and the dissociation of the coat proteins [24, 25].

1.1.2 *The insulin secretory granule: more than merely a container.*

Apart from the insulin-related peptides, ISGs contain more than 100 proteins, comprised of other precursor proteins, processing enzymes, and various membrane proteins [26] (Fig. 1.3). Electron microscope micrographs [27, 28] revealed that ISGs contains an electron-dense core separated from the surrounding membrane by a characteristic halo (Fig 1.3.A), composed by the semi-crystal structure made by hexamers of mature insulin molecules [29]. The halo contains the "soluble part" of the ISG, i.e. several co-secreted proteins and ions.

The insulin granule was previously thought as merely a container, but accumulating evidence [16, 30] suggests that it also acts as a signaling hub (Fig. 1.3.B). Regulatory pathways originate from the ISG capable to influence granule movement, β -cell transcription and proliferation. Moreover, many co-secreted compounds possess regulatory functions, that affect both the β -cell activity and that of neighbor cell types [31, 32]. The concert of this multitude of signals ensures the coordination of several cellular processes and tissues to achieve nutrient homeostasis.

1.2 FROM STRUCTURE TO FUNCTION: GLUCOSE-STIMULATED INSULIN SECRETION.

The metabolic response of the β -cell to glucose is essential for the maintenance of systemic glucose homeostasis. This process can be roughly divided into two main steps: (i) the events of glucose entry and metabolism by the β -cell enzymatic machinery and (ii) the mobilization of ISGs for insulin secretion.

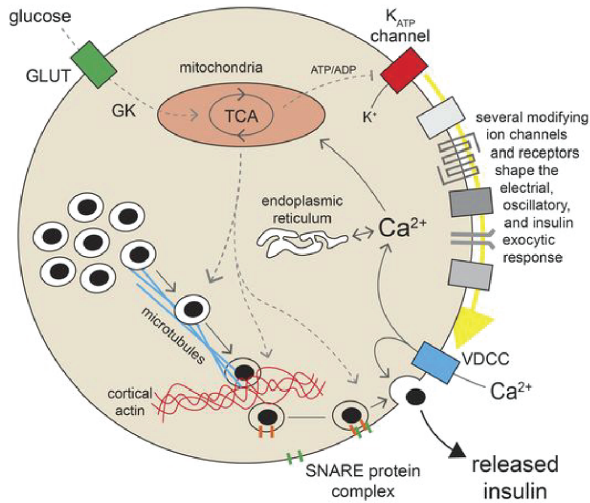
β -cell functions

FIGURE 1.4: Glucose sensing and metabolic signals leading to insulin granule secretion. The release of insulin via exocytosis of secretory granules from pancreatic β -cells is controlled by a series of metabolic and electrical signals arising as a result of glucose entry through GLUTs, phosphorylation by GK, and entry into the TCA cycle. The closure of ATP-dependent K^+ (K_{ATP}) channels triggers electrical events that culminate in Ca^{2+} entry through voltage-dependent Ca^{2+} channels (VDCCs), which triggers exocytosis mediated by SNARE complex proteins. The overall secretory response is modulated by numerous receptors, channels, intracellular Ca^{2+} stores, metabolic signals, and cytoskeletal elements. *Adapted from Tokarz (2018) [18].*

1.2.1 *Step-1: a cascade of metabolic reactions transforms glucose in a trigger signal.*

The rise in circulating glucose levels that normally follow consumption of a meal lead to increased influx of glucose into the cytoplasm of β -cells through the low affinity glucose transporter 2 (GLUT) [33] (Fig. 1.4). The transported glucose is then rapidly converted to glucose-6-phosphate by a low affinity glucokinase, which is the rate-limiting step of glycolysis [34]. The products of glucose oxidation, pyruvate in the first place, and Nicotinamide Adenine Dinucleotide in its reduced form (i.e. NADH) (which is shuttled into mitochondria by mitochondrial glycerol phosphate dehydrogenase (mGPDH) and mitochondrial malate dehydrogenase (mMDH) [35]) together with others substrates participate in the Krebs cycle to produce larger quantities of NADH [36, 37]. NADH then acts as a potent electron carrier (being oxidized into NAD⁺) during the mitochondrial oxidative phosphorylation, fueling the ATP production. Increased ATP/ADP ratio levels induce closure of plasma-membrane-associated ATP-sensitive potassium (K-ATP) channels (Fig. 1.4), which in turn induces depolarization of the plasma membrane and activation of voltage-sensitive calcium channels. Ca²⁺ influx finally promotes and sustain insulin secretion [38], through granule docking and fusion with the plasma membrane via soluble N-ethylmaleimide-sensitive factor attachment protein receptor (SNARE) complexes and release of the granule's content into the blood stream [18] (Fig. 1.4).

1.2.2 *Step-2: ISGs mobilization and exocytosis.*

The second step is granule-mediated insulin secretion, a concerted and complex process which typically happens in a bi-phasic manner [39]. The first phase develops rapidly after glucose stimulation and lasts for a few minutes followed by a second sustained phase that rises slowly and lasts for 1 hours until glycaemia returns to resting levels (Fig. 1.5.A). Notably, the lack of the first phase and a reduction of the second phase of insulin secretion are characteristic features of T2D [38].

The existence of two distinct phases, delayed in time, implies that ISGs experience regulated movements within the β -cell [41–43] (Fig. 1.5.B). In fact, similarly to secretory vesicles in numerous other cell types, ISGs exist within the cell in various functional pools [40, 44]: these include a readily

Granules' pools and biphasic insulin secretion

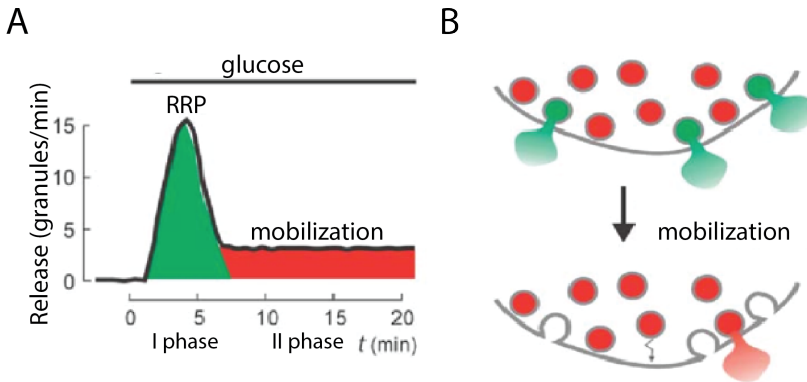


FIGURE 1.5: **A)** Schematic of glucose-induced insulin secretion. **B)** A limited pool of granules is immediately available for release, corresponding to I phase of secretion (RRP, green granules). Most granules initially belong to a reserve pool (red granules) must undergo a series of preparatory reactions in order to be secreted (mobilization). *Adapted from Rorsman (2003) [40].*

releasable pool (RRP) (Fig. 1.5), chemically "primed" for exocytosis, responsible of the first phase and an intracellular reserve pool, that must be mobilize and recruited for the long-lasting second phase [45]. Studies performed in living cells by Total Internal Reflection Fluorescence (TIRF) microscopy demonstrated that second phase secretion results largely from the exocytosis of insulin granules newly recruited to the plasma membrane [46] that comes from the cytoplasm along microtubules through conventional motor proteins [42] and isotropic movements. Near the plasma membrane, insulin granules are transported along the cortical actin network in an ATP-dependent manner, likely by myosin. Actin remodeling stimulated by glucose is also suggested to be an important pre-requisite for granule recruitment and insulin secretion [47, 48] (Fig. 1.6).

1.3 APPROACHING THE β -CELL BY QUANTITATIVE BIOPHYSICS: STATE OF THE ART AND MOTIVATION OF MY WORK.

As described so far in this Chapter, the peculiarity of the β -cell consists in the tight and regulated coupling between (i) glucose uptake and processing through the common metabolic reactions of cell respiration (i.e. glycolysis and oxidative phosphorylation) and (ii) subsequent mobilization and exocytosis of the secretion units the ISGs. This peculiar scheme of processes is altered in T1D and T2D with the final failure and/or loss of insulin-secreting β -cells [49, 50]. It is clear that facing these processes experimentally is multifaceted challenge. The processes described, in fact, occur in a context that evolves within the whole cellular space. For this reason, non-invasive techniques (i.e. capable not to alter cell native status) simultaneously able to address quantitatively the above-mentioned processes in time and space are highly desirable. The arsenal of biophysical techniques available at present hold the potential to tackle these tasks directly in living matter.

1.3.1 *Metabolic imaging of β -cells in physiology and disease: a new label-free paradigm.*

Concerning the first point, i.e. the metabolic response triggered by glucose intake, label-free techniques capable not to alter the chemical identity and endogenous stoichiometry of the key biochemical components of the secretion process are fundamental. The molecular-based biochemical ap-

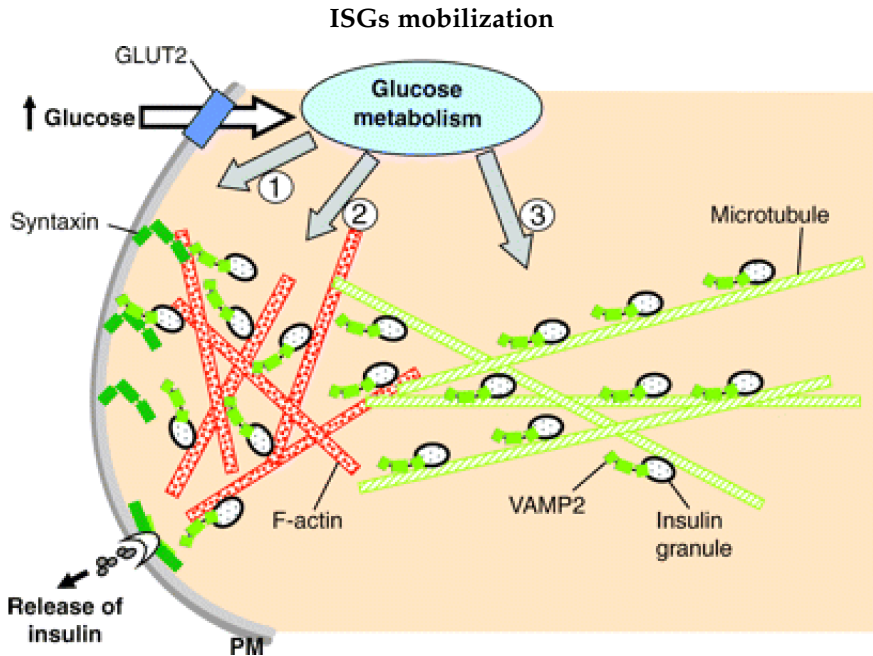


FIGURE 1.6: Glucose enters through the GLUT transporter and rapidly undergoes intracellular metabolism. Through the classic stimulus-secretion coupling ISGs in proximity of the plasma membrane give rise to the first phase of insulin secretion. Concurrently, the metabolic signal also induces actin reorganization and granules' recruitment to the plasma membrane to support the sustained second phase of insulin secretion. *Adapted from Wang (2009) [48].*

proaches presented so far, although very useful, suffer from several issues: the use of over-expressed fluorescence probes to monitor the events in living matter (i.e. fluorescent NADH sensor [51] or fluorescent ATP sensor [52]), with the risk of altering the stoichiometry of the molecular actors involved, or the need to study these processes outside the natural context of a living cell, as for classical biochemical studies. In this regard, two-photon microscopy offers a unique platform for imaging the intrinsic enzyme cofactors NADH and NADPH (which share same excitation and emission properties, hereafter referred to as NAD(P)H) in living cells. NAD(P)H molecules are involved in almost all the metabolic reactions of cellular respiration and glucose processing. NAD(P)H fluorescence imaging was applied to the specific context of the β -cell by Patterson et al. [53] to characterize the response to glucose-stimulation in rodent Langerhans islets. Yet, intensity-based measurements may contain artifacts due to the heterogeneity of NAD(P)H concentration and to differing quantum yields (i.e. different fluorescence emission) of the molecule in the free and bound (to many different proteins/enzymes) forms. A way to overcome the limitation of intensity-based analyses consists in measuring NAD(P)H fluorescence lifetime (the time a fluorophore spends in the excited state before returning to the ground state by emitting a photon) instead of its intensity. Fluorescence Lifetime IMaging (FLIM) microscopy was applied for the first time to the intrinsic signal of intracellular NAD(P)H molecules by Stringari and collaborators [54]. The lifetime of NAD(P)H changes according to its molecular state: if molecules are bound to enzymes they show higher lifetimes (and can be associated to a more oxidative metabolism) as compared to the case they are free (a metabolic status often defined as more "glycolytic"). By exploiting the differences in NAD(P)H lifetime measured by FLIM technique, contrast based on an intrinsic signal can be obtained and can be used to generate a representative map of the metabolic state of the cell. Chapter 2 describes how this technique was applied to study β -cell response to changing glucose levels.

1.3.2 *Spatiotemporal fluctuation spectroscopy as a fast and robust screening method to study granule structural and dynamic properties.*

The β -cell's metabolic response to glucose described above rapidly triggers insulin secretion by granule mobilization and fusion to the plasma membrane. An increasing amount of evidences show that a tight regula-

tion of both ISGs structural (e.g. size, number) and dynamic (e.g. speed, diffusion mode) properties is pivotal to assure their function (i.e. proper regulation of glucose homeostasis through insulin secretion) at cellular, and then systemic, level [40]. In fact, defects in granule structural and dynamic properties are found as hallmarks of pancreatic β -cells dysfunction and, in turn, of the onset of the pathological condition. For instance, it was recently proposed that hypercholesterolemia is capable of increasing granule size and, at the same time, impairing its membrane trafficking properties [55]. Despite the huge research interest and experimental efforts, however, no method proposed thus far is capable of providing fast, robust and simultaneous access to both structural and dynamic information on ISGs in living cells, i.e. is able to probe both the spatial and temporal dimension at the scale of interest. Historically, the insulin secretion process has been addressed measuring the temporal profile of insulin release by means of absorbed antibodies and colorimetric reaction, such as in the ELISA assay (Fig. 1.5.A and Fig. 1.7.A). In this method, still used and fundamental to monitor the efficiency of the overall secretion process, the spatial dimension of the process is inevitably missing. Only indirect evidences of granule spatial organization within the cell cytoplasm (e.g. the presence of RRP) can be retrieved from these measurements, as mentioned above (see section 1.2.2). On the other hand, high spatial resolution can be achieved at the expense of the temporal dimension by means of Transmission Electron Microscopy (TEM) (Fig. 1.3.A and Fig. 1.7.B). Here, at the wavenumbers of electron, it is possible to dissect the finest details of the granule structure, number, and spatial distribution within the β -cell. It is worth noting, however, that this approach has been recently questioned as could be prone to fixation artifacts as demonstrated by Fava *et al.* [56] in fact, chemical fixation with aldehydes induces morphological alterations due to dehydration of the sample which can, eventually, lead to errors in granule size estimation. Recent attempts to tackle this limit by Structured Illumination Microscopy (SIM) (i.e. sub-diffraction resolution applied to living cells exploiting fluorescence) were severely hampered by the dynamic nature of ISGs [40].

Concerning this latter property of ISGs, on the other hand, most of our knowledge comes from the use of fluorescence-based optical microscopy on live cells either by total internal reflection fluorescence (TIRF) imaging [39, 46, 57] and/or by Single Particle Tracking (SPT) studies [58–62]. The former is technically limited to study the cell/glass interface in adherent cells. It was used to clarify the process of docking and fusion at the plasma membrane of fluorescently-labelled granules (Fig. 1.7.C). The

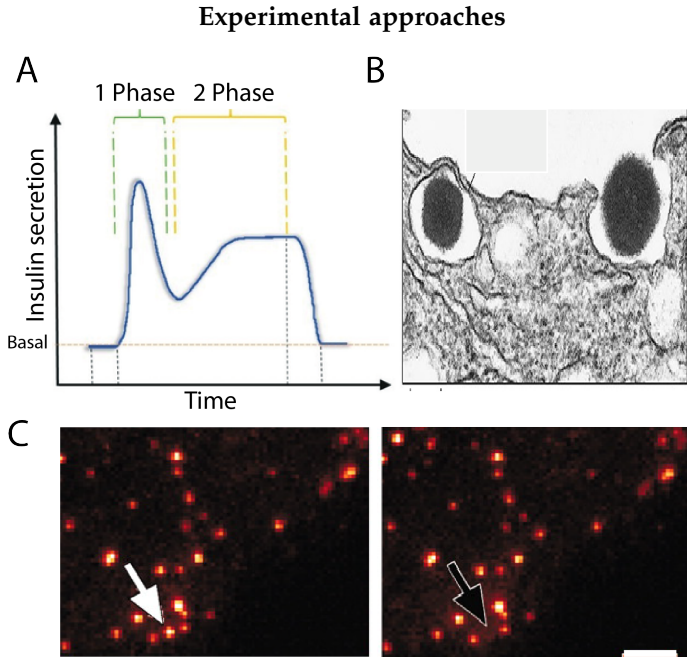


FIGURE 1.7: **A)** Insulin secretion temporal profile with first and second phases. *Adapted from Castiello (2015).* **B)** TEM micrograph of ISG exocytosis. *Adapted from Duvoor (2017).* **C)** TIRF microscopy image shows fluorescently labelled ISGs during exocytosis. *Adapted from Ma (2004).*

latter is inherently time-consuming and technologically-challenging. Yet, it was pivotal to extend the spatial scale of interest, allowing ISGs intracellular trafficking properties to be fully characterized, at the level of single granules [58]. It must be noted, however, that neither of the two strategies was exploited to extract structural information on the trafficking ISGs. In this scenario, fluorescence-based spatio-temporal fluctuation analysis was recently proposed in my laboratory as a powerful quantitative tool to simultaneously extract average structural and dynamic properties of diffusing objects, from molecules [63, 64] to entire sub-cellular nanostructures/organelles [65, 66] directly from standard imaging on living cells, with no need for complex instrumentation, no need for preliminary assumptions/-knowledge on the system, and no need to extract individual trajectories. In Chapter 3 and Chapter 4 of this Thesis I will present the application of a fluctuation spectroscopy method in particular, the *image-derived* Mean Square Displacements (*iMSD*) technique, to retrieve information on ISGs' structural and dynamic properties. It appears clear how fluorescence-based techniques are at present the only capable to satisfy the need spatiotemporal investigations in living cells with the only limitation being that the overexpression of fluorescence probes can, in principle, alter the stoichiometry of the molecular actors involved, generating potential artifacts and leading to misinterpretation of data. This is specifically addressed in Chapter 4 with a close examination of how fluorescent proteins used to tag ISGs impact on granule structural and dynamic properties. Because of these general concerns, the need of label-free approaches is constantly increasing in the scientific community and some (not many) endogenous "contrast-generator" are available within biological systems, but needed to be validated before performing reliable imaging experiments [67]. Some of these, specific for granule, will be described in the final section of Chapter 4.

PHASOR FLIM ANALYSIS OF β -CELL METABOLIC RESPONSE TO GLUCOSE STIMULATION

Most of the content of this Chapter is included in the following manuscript, recently accepted by Faseb Bioadvances:

- Metabolic response of Insulinoma INS-1E cells to glucose stimulation studied by fluorescence lifetime imaging.

Ferri G., Tesi M., Massarelli F., Marselli L., Marchetti P., Cardarelli F.

Once docked to the cell membrane, granules are ready to be secreted. A cascade of highly regulated biochemical processes, extensively summarized in section 1.2.1, connects glucose stimulation to insulin secretion (GSIS). In spite of the central role of the β -cell biochemistry for systemic glucose homeostasis, there is a lack of non-invasive and fast strategies to identify the metabolic state of living β -cells in the physiological state and its possible alteration in the pathological condition. To tackle this issue, NAD(P)H species are used here as intrinsic metabolic biomarkers and the phasor approach to FLIM microscopy applied to extract the metabolic signature of β -cells in terms of the ratio between protein-bound and free NAD(P)H under different conditions. Here, Insulinoma 1E (INS-1E) β -like cells are elected as model for recapitulating primary β -cell functions. Their metabolic response to glucose stimulation in terms of bound/free NAD(P)H is measured by phasor-FLIM analysis in normal and hyperglycemic condition. Moreover, with phasor-FLIM is possible to concomitantly monitor the appearance of hyperglycemia-induced ROS damages to intracellular membranous compartments, recognizable as long-lifetime species (LLS).

2.1 IMAGING OF NAD(P)H AUTOFLUORESCENCE.

Given its biological importance, the possibility to monitor NAD(P)H level in living cells could represent a valid marker for qualitative/quantitative assessments on cellular metabolic state. In this sense, the pioneering studies of Chance *et al.* [69, 70] have laid the ground for future works

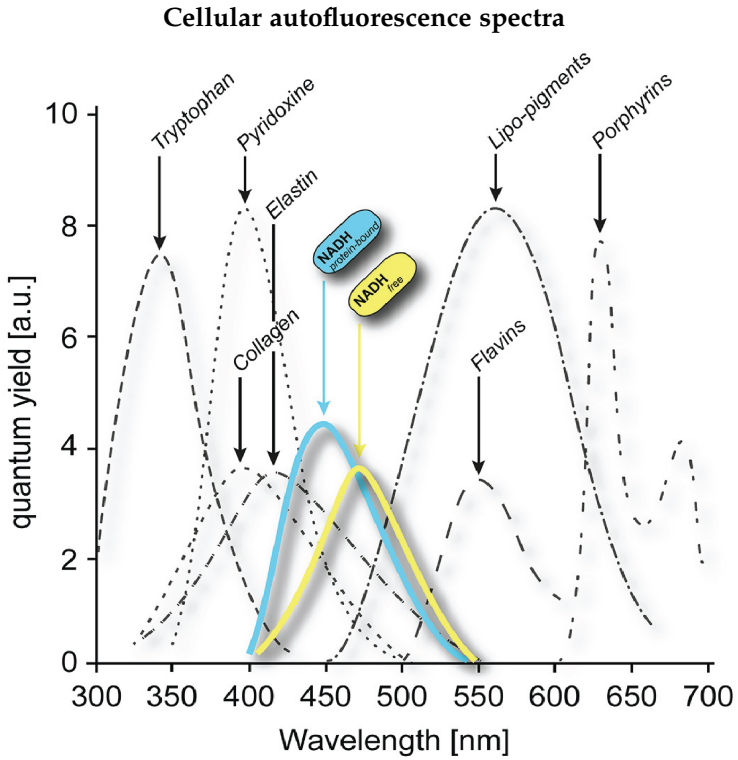


FIGURE 2.1: Emission spectra of NAD(P)H bound (blue) and NAD(P)H free (yellow) are shown. The emission is peaked around 460 nm. Adapted from Schaefer et al. (2019). *Adapted from Schaefer (2019) [68].*

based on NAD(P)H optical properties. In fact, both oxidized NAD(P)⁺ and reduced NAD(P)H show strong absorption in the UV region around 260 nm; however, only NAD(P)H absorbs appreciably at 350–365 nm and emits fluorescence with a peak at \sim 460 nm (Fig. 2.1). In the emission interval between 400 – 500 nm the contribution of other autofluorescence species is negligible except for collagen which is not present in laboratory cultured cells [71]. Within intrinsic fluorophores, NAD(P)H also has a good two-photon cross section around 720 nm [72], allowing two-photon excitation and therefore achievement of a good penetration depth and minimal perturbation/damage of the sample. However, intensity-based measurements may contain artifacts due to the heterogeneity of fluorophore concentration and to differing quantum yields of NAD(P)H in the free and bound (to proteins) form [53, 73].

2.2 PHASOR-FLIM APPROACH TO NAD(P)H-BASED METABOLIC FINGERPRINT.

To overcome these issues, Lakowicz et al. [74, 75] introduced a new methodology based on Fluorescence Lifetime IMaging (FLIM) microscopy in which the "contrast" depends on the fluorescence lifetime (i.e. a measure of the time a fluorophore spends in the excited state before returning to the ground state by emitting a photon) and not on the local concentration and/or intensity of the fluorophore (the number of emitted photons). The main advantage of FLIM microscopy is that it can selectively discriminate the free and protein-bound forms of NAD(P)H molecules [74]. In turn, then, the ratio of bound/free NAD(P)H species can be used to identify different metabolic states of cells (e.g. the glycolytic phenotype, with a low bound/free ratio, and the oxidizing condition, with a high bound/free ratio). In fact, free NAD(P)H has a relatively short decay time of 0.4 ns. The mean fluorescence lifetime of protein-bound NAD(P)H varies between 2.0 and 4.0 ns [75], dependent on its microenvironment. As the absolute amount of NAD(P)H bound to proteins is usually relatively stable [75], the ratio of free to protein-bound NAD(P)H coincides with the NAD(P)H redox state. It can be concluded that a shift in cellular metabolism toward glycolysis and/or lower mitochondrial respiration corresponds with a shortening of NAD(P)H lifetime and vice versa (Fig. 2.2) [68].

In particular, the ratio of bound/free NAD(P)H species was used to identify different metabolic fingerprints of cell states, including disease

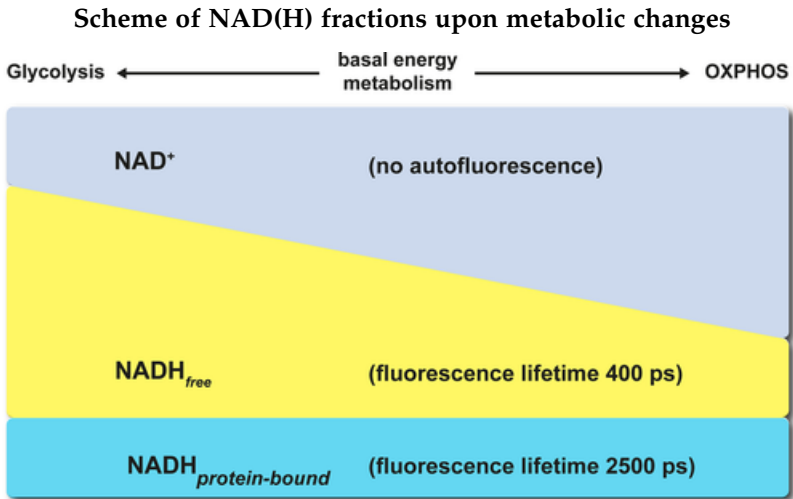


FIGURE 2.2: Under the assumption of a stable NAD⁺/NAD(P)H pool, a change in redox ratio, for example, due to metabolic alterations, changes the NAD(P)H concentration and thereby the total NAD(P)H autofluorescence intensity. FLIM further allows differentiation of free and protein-bound NAD(P)H by their decay times, resulting in the mean NAD(P)H lifetime, which coincides with the redox state and metabolism. *Adapted from Schaefer (2019) [68].*

Phasor plot principles

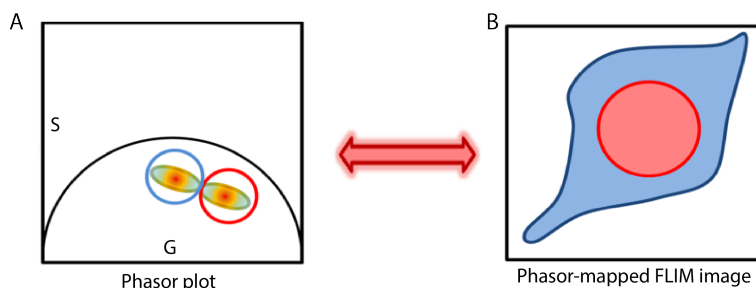


FIGURE 2.3: **A)** Selecting different regions of the phasor plot results in **B)** a selection of different areas of the image and a phasor color-mapped FLIM image and viceversa. *Adapted from Ranjit (2018) [79].*

progression, stage of differentiation, apoptosis and cell fate [54, 76, 77]. To summarize, differently from NAD(P)H intensity analysis, FLIM has the potential to retrieve quantitative information about the ratio of NAD(P)H molecules in the "bound" (e.g. to enzymes) and "free" form, although with a few selected limitations, namely: (i) NAD(P)H and NAD(P)H species cannot be distinguished; (ii) the metabolic response is reported in terms of bound/free ratio but changes can occur in both the numerator and denominator; (iii) the approach, as used here, does not have native single-enzyme or single-pathway resolution.

A further step of analysis can be reached when FLIM-based measurements are coupled with phasor analysis, historically applied in electric circuit studies, and then extended for the first time to the FLIM field by Digman *et al.* [78]. In phasor analysis, the fluorescence lifetime spectra of each pixel in the image is mapped onto a "phasor" that is made up out of two numbers: the real and imaginary parts of the first harmonic of the Fourier transform of the fluorescence intensity decay (see Methods in Appendix A). These two numbers (namely g and s coordinates) are used as coordinates in a scatter plot, the phasor plot. Thus, the phasor plot contains clouds of points that correspond to pixels with similar lifetime spectra (Figure 2.3.A). The phasor plot is represented by a semicircle where the zero lifetime is located at ($g=1, s=0$) and the infinite lifetime located at ($g=0, s=0$). By changing the lifetime from zero to infinity the phasor point moves along a semicircle from (1,0) to (0,0).

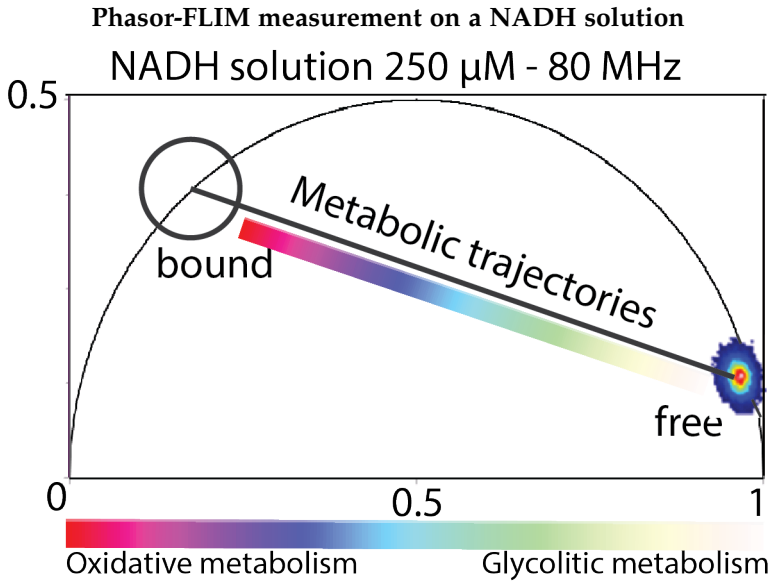


FIGURE 2.4: Phasor-FLIM measurement on a 250 μ M NAD(P)H "free" solution, used as reference for trajectory position.

The goal of this approach is the creation of a color-mapped image in which different colors represent different fluorescence lifetime decays [79]. In fact, a distinguishing feature of phasor analysis is that any region of the phasor plot (which corresponds to a type of decay) can be selected with cursors (red and blue in the figure) in order to directly identify the pixels in the image with that given lifetime (Fig. 2.3.B). This process can be also reversed, and different areas of the intensity image can be selected to obtain the corresponding phasor distribution (segmentation analysis). The phasor approach to FLIM provides a powerful visualization of the data content with a fit-free analysis of the information contained in the thousands of pixels constituting an image. Graphically, in the phasor plot it is possible to define a trajectory, starting from a region of the plot corresponding to enzymes-bound NAD(P)H characteristic lifetimes (spanning from 3 to 3.6 ns) [80, 81] to a region corresponding to free NAD(P)H in solution (lifetime 0.4 ns) measured with at high repetition rate (80 MHz) by two-photon laser (Figure 2.4).

Associated to this trajectory, a color-bar can be used to color each pixel of the image according to the lifetime decay measured in that pixel. According to the linear combination properties of phasors [82], in fact, each pixel lying on the trajectory contains a mixed fraction of the two pure species representing the end-points of the line (bound and free NAD(P)H in this case).

Specifically in the context of insulin secretion, the phasor-FLIM analysis on NAD(P)H species was already used to monitor the metabolic status of intact human and/or mouse Langerhans islets under different stimuli [83–85]. In particular, in a recent pioneering work by Gregg and collaborators [83], phasor-FLIM analysis revealed an increase in the ratio of bound/free NAD(P)H species in both human and mouse islets in response to glucose stimulation, an effect then impaired by aging. The observed shift in NAD(P)H lifetimes measured on entire islets after glucose stimulation is generally attributed to the response of the β -cells to this event, although it is not currently possible to distinguish between different endocrine cell types within such a complex system.

2.3 EXPERIMENTAL MODEL OF β -CELLS.

The majority of studies published so far on β -cells physio-pathology have been accomplished on laboratory cell models recapitulating the principal features of native β -cells, especially the response to glucose stimulation. While, on the one hand, these cell lines cannot provide a complete replica of real β -cells situated within the pancreas (which benefit from input by neural, cellular and vascular regulators) they allow to tackle the major limitation related to the availability of animals or human primary tissues. Rodent derived cell lines possess both immortality and intact β -cell stimulus secretion coupling. They have been generated since 1980 [86] and well characterized during these years both for research purposes and for use in proof-of-principal studies of cell therapy, such as anti-diabetic drug testing. Between all, MIN6 [87] and INS-1E [88] cell lines have proven particularly popular for β -cell research, as indicated by estimated publication numbers: 1145 for MIN-6 and 1538 for INS-1E (data updated to 2018 [89]). INS-1E cells, especially, exhibit a high insulin content and a very accurate β -cell function and for these reasons they were chosen also for the majority of the experiments proposed in this Thesis.

2.4 THE β -CELL METABOLIC STATUS.

The phasor-FLIM analysis is applied here to INS-1E cells to monitor their metabolic status in terms of bound/free NAD(P)H species in standard culturing (11 mM glucose) and then, the metabolic response to glucose stimulation.

2.4.1 *Preliminary fluorescence intensity analysis of NAD(P)H species in INS-1E cells.*

By using a two-photon excitation source tuned at 710 nm flashed on living cultured (and unlabeled) cells, the main contribution to the total detected auto-fluorescence signal arises from NAD(P)H species, which are optically active with most of the fluorescence emission in the 400-500 nm range [54] (Fig. 2.1). Under typical maintenance culturing conditions (i.e. complete RPMI medium supplemented with 11.1 mM glucose), an intrinsic fluorescence signal from INS-1E cells is clearly detectable (Fig. 2.5.A). It derives mainly from cytoplasmic regions, which appear with a peculiar patterned staining (presumably belonging to mitochondria). Cell nuclei, instead, can be distinguished as ellipsoidal regions with a sensibly lower auto-fluorescence signal (Fig. 2.5.A).

Overall, the intracellular distribution of detected signals reflects the expected localization of NAD(P)H species and well agrees with previous measurements on different cellular systems [53, 90]. The same cells cultured for 48 hours in condition of hyperglycemia, which is known to impair β -cells metabolism and physiology [90, 91], show a similar autofluorescence pattern, but with absolute intensity values that appear significantly increased compared to maintenance condition (130.2 ± 19.9 , 84.7 ± 12.2 respectively, $p < 0.0001$) (Fig. 2.5.B). This finding is in line with previous observations correlating glucose concentration in the medium and intracellular autofluorescence signal [53, 90]. As described in detail in the Appendix A and according to previous reports [92], a protocol for acute glucose stimulation of INS-1E was used. The total autofluorescence intensity of INS-1E cells (Fig. 2.5.C) increases significantly upon exposure to 16.7 mM glucose concentration with respect to 2.5 mM glucose after both the above-mentioned culturing conditions (48h at 11.1 mM or 30 mM glucose). However, this increment is significantly higher in cells previously kept at 11.1 mM glucose, compared to those culture at 30 mM glucose (respectively 41.6 ± 10.6 %

Autofluorescence intensity analysis

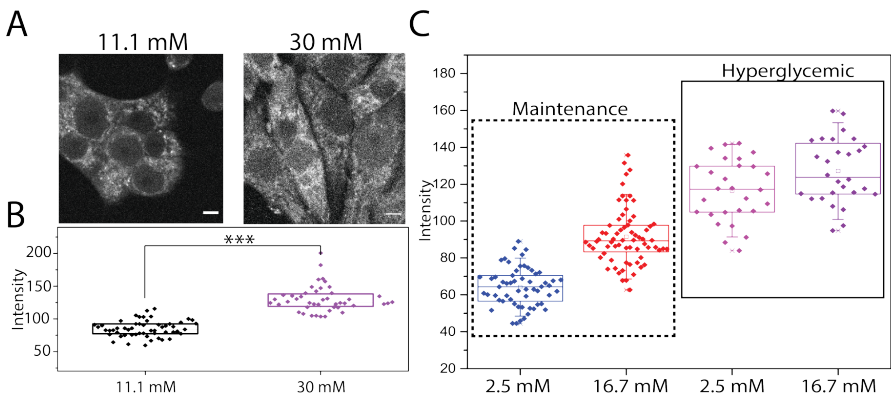


FIGURE 2.5: **A**) Representative images of NAD(P)H auto-fluorescence intensity in INS-1E in maintenance condition (11.1 mM glucose) and in INS-1E cultured for 48 hours in hyperglycemic condition (30 mM glucose). Scale bar: $5 \mu\text{m}$. **B**) Box plots for different culturing conditions. Each point represents the total NAD(P)H intensity of a single cell. Boxes represent 25 and 75 percentiles, lines represent median, whiskers represent SD. (***) p value < 0.001 , Mann-Whitney test). **C**) Box plots for different culturing conditions. Each point represents the total NAD(P)H intensity of a single cell. Boxes represent 25 and 75 percentiles, lines represent median, whiskers represent SD.

NAD(P)H intensity and insulin secretion

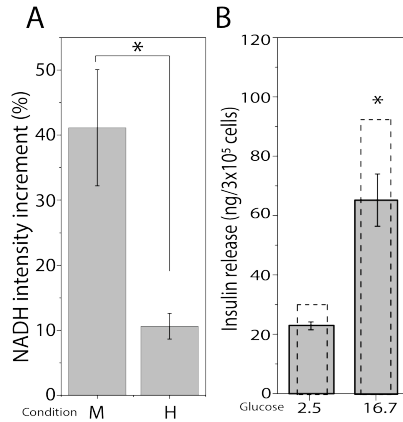


FIGURE 2.6: **A)** NAD(P)H intensity fractional increment in maintenance (M) and hyperglycemic (H) conditions, calculated as fold increment in NAD(P)H intensity measured between 2.5 and 16.7 mM; * p value < 0.05. **B)** Insulin release measured by ELISA-kit assay in low (2.5 mM) and high (16.7 mM) glucose concentration in cells pretreated for 48h with 30 mM glucose. Stimulation was carried out following protocol described in Methods section. Data are the means \pm SE of three separate measurements. Dashed columns represent measured insulin release in maintenance condition. * p value < 0.05 compared with high glucose (16.7 mM) of maintenance condition.

and 8.9 ± 2.0 %, $p=0.007$, Fig. 2.6.A). Accordingly, acute glucose-stimulated insulin release in response to 16.7 mM glucose was significantly higher with the INS-1E cells cultured for 48h at 11.1 mM glucose than with those kept at 30 mM glucose (Fig. 2.6.B), indicating that in this latter case cells had functional features of "glucose toxicity" [93].

2.4.2 FLIM analysis of NAD(P)H species in INS-1E cells in response to glucose stimulation.

As already stated above [68], intensity-based measurements of NAD(P)H species inevitably contain artifacts due to the heterogeneity of fluorophore concentration and to differing quantum yields of NAD(P)H in the free and bound (to proteins) form. FLIM, instead, reports on the fluorophore's micro-environment and, in this case, can discriminate between "free" and "protein-

bound" NAD(P)H species within the cell. Phasor FLIM analysis applied to INS-1E cells under maintenance culturing conditions yields a reference position of the NAD(P)H bound/free lifetime ratio (Fig. 2.7.A). Visual inspection of FLIM maps suggests the expected prevalence of NAD(P)H molecules in the "bound" form within the cytoplasm while nuclei are enriched NAD(P)H molecules in the "free" form (Fig. 2.7.B, left panels).

This readout is used to test cell response to glucose stimulation following the protocol described above. More in detail, once exposed at 16.7 mM glucose, cells were imaged for approximately 45 minutes. As showed in Fig. 2.7.B-C, glucose stimulation produces a clear shift of the NAD(P)H bound/free lifetime ratio towards higher values. In particular, a comparative analysis of the phasor coordinates of unstimulated (black squares, $n=28$) and stimulated cells (red circles, $n=35$), represented by single data points, is reported in Fig. 2.7.D, in which variations along both g and s axes of the phasor plot can be appreciated. At this point, by exploiting the imaging potential of 2-photon FLIM, it is performed a spatial segmentation analysis of data (see section 2.2) to extract the specific contribution of the cytoplasm (and nucleus) of cells to the observed metabolic shift (Fig. 2.8.A). The obtained scatter plots of the average values of phasor distributions from the nucleus (yellow, top graph) and cytoplasm (red, bottom graph) are reported in Fig. 2.8.B: it is clear that the cytoplasm of cells is the location where the metabolic shift towards an higher bound/free NAD(P)H lifetime ratio does take place (compare empty and full data points in Fig. 2.8.B, bottom panel).

2.4.3 *The characteristic metabolic signature of the β -cells.*

The metabolic response upon glucose stimulation observed in insulin-secreting INS-1E cells was compared to similar measurements performed in non-secreting cells, namely A549 (lung tumor-related cells) and HEK 293 cells (human embryonic kidney cells) (Fig. 2.9.A). Both A549 and HEK293 cells exposed to the same treatments (i.e. pulsed stimulation with 16.7 mM glucose to mimic secretion) did not show any significant increase in the bound/free NAD(P)H lifetime ratio of NAD(P)H calculated as the Euclidean distance between the ellipsoid central points of unstimulated and stimulated cells (Fig. 2.9.B). The observed different response between insulin-secreting cells and non-secreting cells reflects a different biochemical regulation of glucose intracellular metabolism. This result can be readily interpreted as a tight coupling between glucose influx and activation of

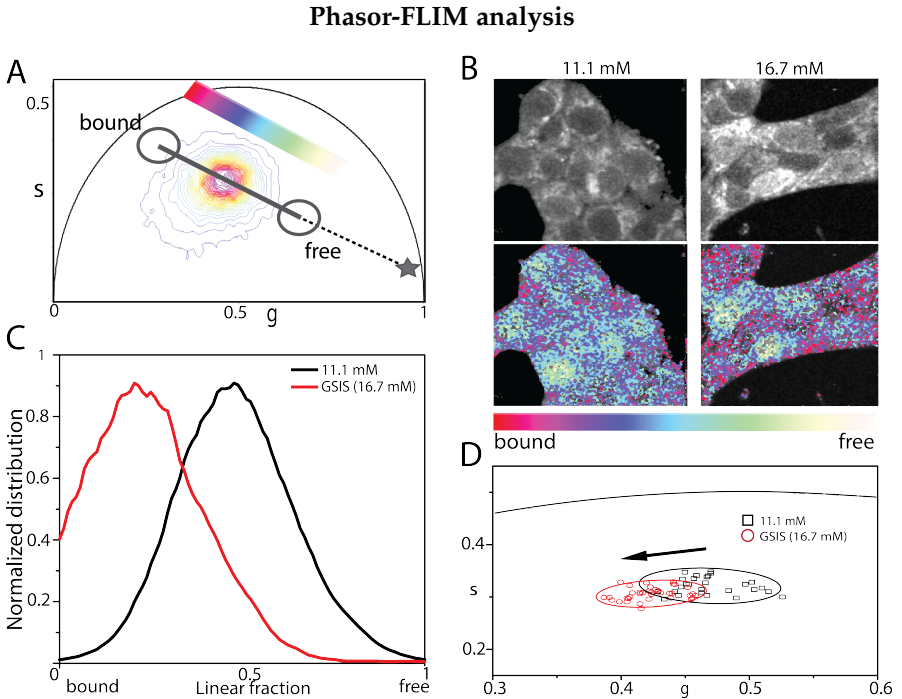


FIGURE 2.7: **A)** Phasor plot of control and stimulated cells. Color-bar defines the variations from NADH bound state (red/magenta) to NADH free state (green/white). Grey symbol represents the position in the phasor plot of pure NADH solution. **B)** Exemplary images of total NADH intensity of INS-1E cell clusters (top line) in 11.1 mM glucose and . On bottom line, same images colored in accordance to the color bar defined below. **C)** Distributions of the free and bound NADH species for all pixels of acquired image in (B) for 11.1 mM and GSIS condition. **D)** Scatter plot of the average values of distinct phasor distributions, each relative to distinct acquired cells. Black squares represent cells in maintenance condition, in red circles stimulated cells. Standard deviation is depicted as 90% confidential ellipsoid in accordance to aforementioned colors.

Segmentation analysis on INS-1E cells upon glucose stimulation

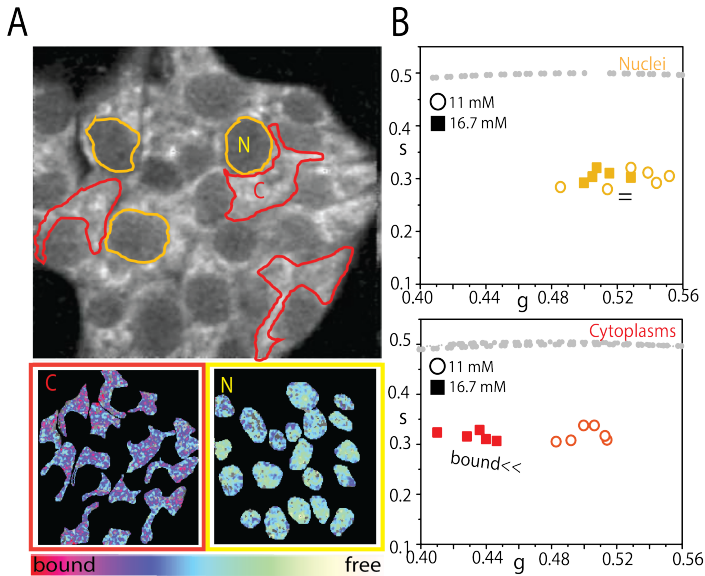


FIGURE 2.8: **A)** Top: Exemplary NAD(P)H intensity image of a cluster of INS-1E cells. Examples of ROI for segmentation analysis are reported: nuclei are identified as yellow ROI (N) while cytoplasmic regions are identified as red ROI (C). Nuclei are selected based on their ellipsoidal shape and typical lower NAD(P)H intensity signal. Bottom: Example of segmentation analysis performed on the cell cluster above, with color-mapped NAD(P)H phasor-FLIM reported. Color-bar defines the variations from NAD(P)H bound state (red/magenta) to NAD(P)H free state (green/white). **B)** Scatter plot of the average values of distinct phasor distributions obtained by segmentation analysis for nuclei (yellow) and cytoplasmic regions (red) for cell cultured in maintenance condition (circle, $n=6$ acquisitions) and stimulated with 16.7mM glucose (solid square, $n=5$ acquisitions), each relative to distinct analyzed cell clusters.

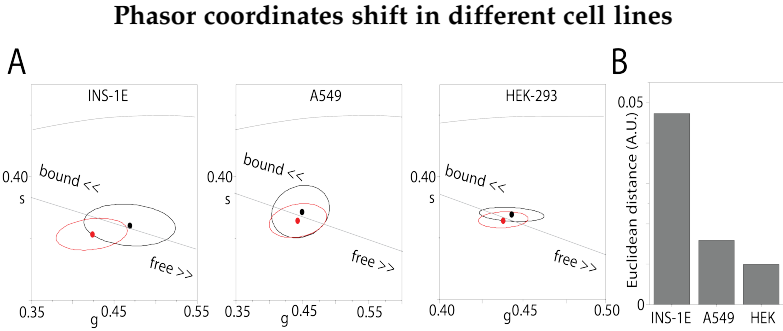


FIGURE 2.9: **A**) Phasor FLIM plot for different cell lines (INS-1E, A549, HEK-293). In each phasor plot confidential ellipsoids are depicted in representation of distinct measures of unstimulated (black) and stimulated (red) cells. Ellipsoid central points (average value) are reported. **B**) Euclidean distance calculated as geometrical distance between ellipsoid central points.

the oxidative phosphorylation process. Similar results has been previously obtained with biochemical assay in Refs. [94, 95].

2.5 EFFECT OF β -CELL EXPOSURE TO CHRONIC HYPERGLYCEMIC CONDITIONS.

INS-1E cells response to glucose pulsed stimulation after exposing cells to hyperglycemic conditions was also measured (30 mM glucose for 48 hours, see Appendix A for more details). In this experiment, cells showed a sensibly reduced metabolic response in terms of phasor shift towards higher bound/free NAD(P)H lifetime ratios (Fig. 2.10.A). This can be visualized qualitatively by means of the color-coded maps of intracellular NAD(P)H bound/free ratio (exemplary case in Fig. 2.10.B) and, quantitatively, by the corresponding bound/free ratio value for each measured cell (Fig. 2.10.C) and cumulative results from the whole population of observed cells (Fig. 2.10.D). Again, spatial segmentation analysis of data is useful to extract the specific contribution of the cytoplasmic and nuclear regions of cells (Fig. 2.11.A). The obtained scatter plots of the average values of phasor distributions from the nucleus (yellow, top graph) and cytoplasm (red, bottom graph) are reported in Fig. 2.11.B. As somewhat expected, the contribution to the metabolic response of the cytoplasmic regions (that was dominant upon glucose stimulation from maintenance conditions) is now

almost completely impaired (compare empty and full data points in Fig. 2.11.B, bottom panel).

2.5.1 *Reduced response to glucose stimulation under hyperglycemic conditions correlates with production of intracellular oxidative stress.*

The phasor-FLIM analysis gives access to additional metabolic information in the case that reactive oxygen species (ROS)-induced damages are produced intracellularly, especially on lipids. Datta et al. [96], in fact, identified the products of lipid oxidation by ROS as auto-fluorescent, endogenous markers of stress, with a characteristic long fluorescent lifetime (i.e. approximately 8 ns). The presence of long lifetime species (LLS) generates a third auto-fluorescent component along with those belonging to "free" and "bound" NAD(P)H but still with similar excitation and emission properties. Such additional contribution to the average measured lifetime induces a detectable alteration of the lifetime distribution in the phasor plot. More in detail, phasor plots in Fig. 2.12.A show the emergence of an elongation of the lifetime distribution towards the LLS-specific position in the phasor plot in cells exposed for 48h to 30 mM glucose with respect to those maintained at 11.1 mM glucose. Phasor points which show the shift toward LLS were highlighted using a yellow cursor while the metabolic path connecting the characteristic "bound" and "free" states was shown using same color scheme represented in previous figures (Fig. 2.12.B). To confirm that the identified LLSs are a product of oxidative stress, cells cultivated under standard conditions were treated with 100 μM of hydrogen peroxide. Massive ROS treatment with H_2O_2 induces a more pronounced shift towards LLS vertex respect to control and even respect to cell growth in 30 mM, as confirmed by three component analysis reported in Fig. 2.12.C. The data shows the fractional intensity contribution of the LLS for each pixels of the acquired images, that is larger in the 30 mM condition and for 100 μM H_2O_2 treatment respect to standard cultivation condition.

2.6 CONCLUDING REMARKS

Phasor-FLIM analysis on NAD(P)H bound/free state demonstrated how β -cell responds peculiarly to the glucose stimulation, by increasing the bound/free ratio of their intracellular pool of NAD(P)H molecules. This result recapitulates what observed by others in the entire human and

Phasor FLIM analysis on hyperglycemic culturing condition

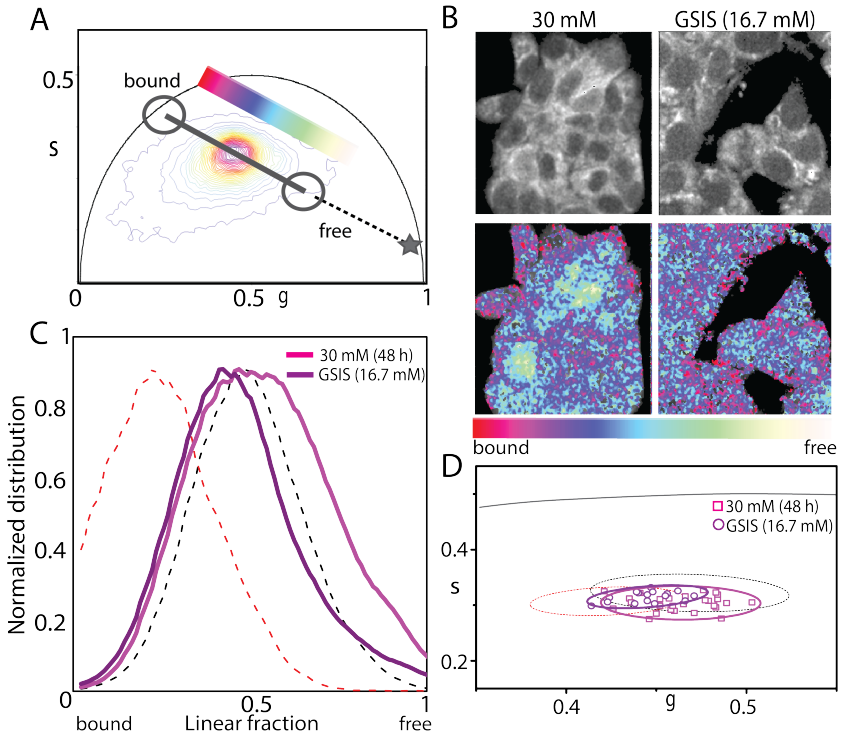


FIGURE 2.10: **A)** Exemplary phasor plot of cells cultured in hyperglycemic condition and stimulated. Colobar defines the variation trajectories from NADH bound state (red/magenta) to NADH free state (green/white). **B)** Exemplary images of total NADH intensity of cells cluster (top line) after 48h in 30 mM glucose and after GSIS. On bottom line, same images colored in accordance to the color bar defined below. **C)** Distributions of the free and bound NADH species for all pixels of acquired image in (B) for 30 mM and GSIS condition. **D)** Scatter plot of the average values of distinct phasor distributions, each relative to distinct acquired cells cluster. In magenta squares $n=30$ cells in 48h hyperglycemic culturing condition, in violet circles $n=20$ stimulated cells. Standard deviation is depicted as 90% confidential ellipsoid in accordance to aforementioned colors. Confidential ellipsoid relative to standard culturing condition (dotted black line) and induced stimulation starting from standard condition (dotted red line) are also depicted.

Segmentation analysis on INS-1E cells pre-incubated in hyperglycemic conditions

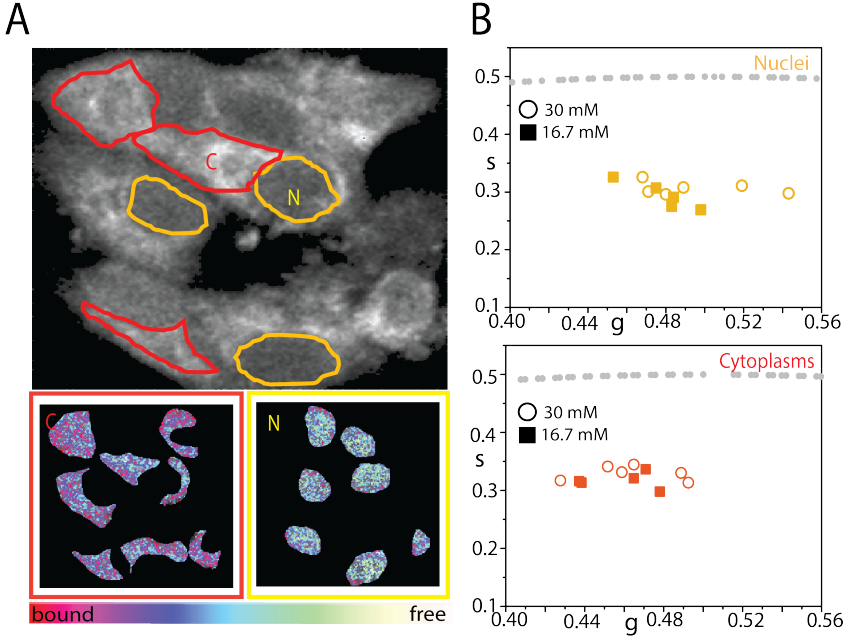


FIGURE 2.11: **A)**Top: Exemplary NAD(P)H intensity image of a cluster of INS-1E cells cultured in 30mM glucose for 48h. Examples of ROI for segmentation analysis are reported: nuclei are identified as yellow ROI (N) while cytoplasmic regions are identified as red ROI (C). Nuclei are selected based on their ellipsoidal shape and typical lower NAD(P)H intensity signal. Bottom: Example of segmentation analysis performed on the cell cluster above, with color-mapped NAD(P)H phasor-FLIM reported. Color-bar defines the trajectory from NAD(P)H bound state (red/magenta) to NAD(P)H free state (green/white). **B)** Scatter plot of the average values of distinct phasor distributions obtained by segmentation analysis for nuclei (yellow) and cytoplasmic regions (red) in cells cultured in hyperglycemic condition (circle, $n=6$ acquisitions) and stimulated with 16.7mM glucose (solid square, $n=5$ acquisitions), each relative to distinct analyzed cell clusters.

LSS species as oxidative stress signature induced by hyperglycemia

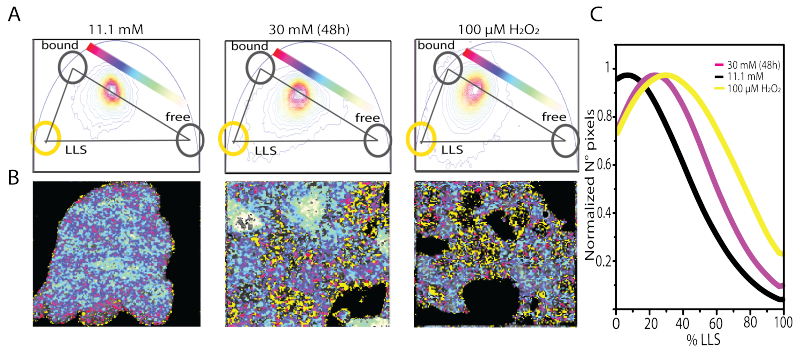


FIGURE 2.12: **A)** Three components analysis on phasor plot of cells cultured in 11.1 mM glucose, exposed to high glucose medium for 48h and treated with 100 μm H₂O₂ to stimulate ROS production. **B)** Exemplary images and relative lifetime-based color map for NAD(P)H trajectory. Pixels with LLS species are colored in yellow, according to the position of yellow cursor in phasor plot. **C)** Resultant graph from three components analysis, in which percentage of LLS species is plotted versus the number of pixels in which long lifetimes species are present for the three conditions.

mouse Langerhans islet [83] and corroborates the idea that what observed in the islet well describes the contribution of β -cells. Along this reasoning, INS-1E response is consistent with a large amount of biochemical and genomic/proteomic data collected on β -like and actual β -cells. It is known, for instance, that finely tuned metabolic pathways are active in pancreatic β -cells to funnel glucose carbons from glycolysis to the mitochondria for oxidative phosphorylation [97]. Unlike most of the cells, β -cells, in fact, lack the lactate transporter MCT1 and show reduced expression levels of lactate dehydrogenase, thus sensibly reducing the amount of glucose that is metabolized to lactate [98, 99] (Fig. 2.13). In addition, the mGPDH and mDH hydrogen shuttles that transport NADH from the cytoplasm to the mitochondria are particularly active in the β -cell [100, 101], favoring NADH consumption by the Electron Transport Chain (ETC). In ETC, Complex I (NADH-ubiquinone oxidoreductase) is the primary electron entry point and is absolutely required for glucose-stimulated insulin secretion [102]. It is the major enzyme that oxidizes NADH to NAD⁺. Therefore, it can be assumed as principal enzyme responsible for NAD(P)H-bound state signature revealed with phasor-FLIM.

Such a potentiated orientation towards ox/phos metabolism is, indeed, a key biochemical signature of the β -cell. It is thus not surprising that, in our experimental setup, non-secreting cells show substantially no metabolic shift upon glucose stimulation. Phasor-FLIM is used here also to show that INS-1E chronically exposed to hyperglycemia have a very reduced shift towards oxidative phosphorylation metabolism after glucose stimulation (data supported by a measured reduced GSIS with ELISA assay). In this regard, Haythorne and collaborators, by means of a multi-omics functional approach, recently showed that mitochondrial metabolism is impaired in rodent islets and INS-1 cells cultivated in hyperglycemic conditions [90]. Exposure of β -cell to a high glucose concentration not only stimulates NAD(P)H production by the conventional glucose metabolic pathways including glycolysis and the TCA cycle (see Fig. 2.5 and Fig. 2.6 for total NAD(P)H autofluorescence) but also stimulates production of reactive oxygen species (ROS), mainly deriving from mitochondrial ETC and Complex I activity [103–106]. Nonetheless, how Complex I function is indeed impaired (either an increase or a decrease in activity) by diabetic hyperglycemia in β cells has yet to be investigated [107]. Phasor-FLIM analysis here successfully identifies the emergence of ROS-induced damage in the context of INS-1E dysfunction, paving the way to rapid, label-free, approach to follow the

Model for coupling of glucose metabolism to insulin secretion

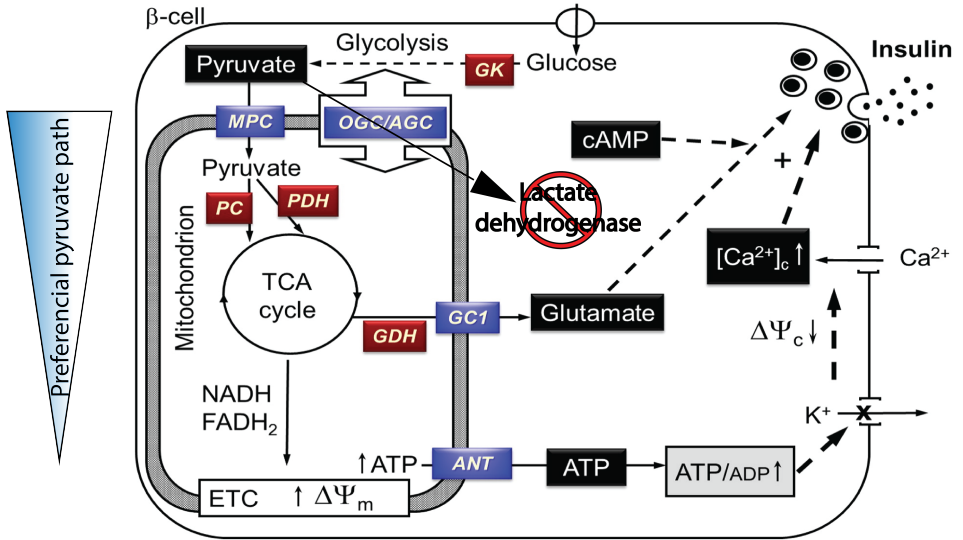


FIGURE 2.13: Glucose equilibrates across the plasma membrane and is phosphorylated by glucokinase (GK). Further, glycolysis produces pyruvate, which preferentially enters into mitochondria through MPC and fuels the TCA cycle by the action of both pyruvate dehydrogenase (PDH) and pyruvate carboxylase (PC). *Adapted from Brun (2016) [99].*

progression from a physiologic to pathologic condition typical of diabetes onset.

IMAGING-DERIVED MEAN SQUARE DISPLACEMENT (IMSD) ANALYSIS TO STUDY THE STRUCTURAL AND DYNAMIC PROPERTIES OF FLUORESCENTLY-LABELLED INSULIN GRANULES IN LIVE CELLS

Most of the content of this Chapter was peer-reviewed and published with co-authors in:

- Time-lapse confocal imaging datasets to assess structural and dynamic properties of subcellular nanostructures. *Scientific Data* (2018).

Ferri G., Digiaco L., D’Autilia F., Durso W., Caracciolo G., Cardarelli F.

- Insulin secretory granules labelled with phogrin-fluorescent proteins show alterations in size, mobility and responsiveness to glucose stimulation in living β -cells. *Scientific Reports* (2019).

Ferri G., Digiaco L., Lavagnino Z., Bugliani M., Cappello V., Caracciolo G., Marchetti P., Piston D.W., Cardarelli F.

In the previous Chapter, the process of insulin secretion stimulated by glucose concentration was investigated and characterized in terms of the metabolic changes occurring in the β -cell. The possibility to exploit NAD(P)H autofluorescence to address this key feature of the β -cell guarantees a non-invasive and label-free approach capable to exclude possible artifacts introduced by exogenous metabolic probes. As discussed above, this finely-tuned metabolic response triggers the mobilization of ISGs in the cell cytoplasm, a process finally leading to secretion. Granule intracellular mobility was identified as the second pillar of my Thesis work. The characterization of macromolecular motion in living cells is an important task of biophysics. Among many approaches, fluorescence fluctuation microscopy encompasses a diversified arsenal of analytical tools useful for this purpose. In this Chapter, the implementation of one of these fluctuation spectroscopy techniques (namely, *imaging-derived* Mean Square Displacement, or *iMSD*) and its adaptation to the specific aim of ISG mobility characterization is described.

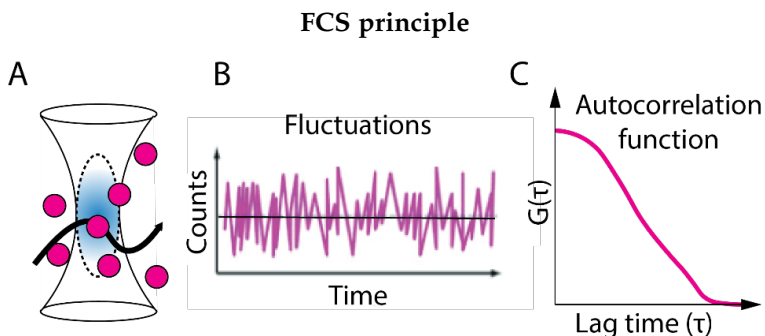


FIGURE 3.1: **A)** Confocal detection volume. Molecules (magenta) are free to diffuse. **B)** Free fluorescent molecules are detected as a series of short, randomized fluorescence bursts. **C)** FCS autocorrelation functions calculated with Eq. 3.1.

3.1 FLUORESCENCE CORRELATION SPECTROSCOPY TECHNIQUES TO STUDY DYNAMIC EVENTS: FROM LOCAL TO SPATIAL ANALYSIS.

Fluorescence Correlation Spectroscopy (FCS), developed in 1972 [108], allows to study the dynamics of fluorescently-labeled objects at high temporal resolution with no need for single-object localization. In detail, FCS measures spontaneous intensity fluctuations caused by small deviations from thermal equilibrium [108, 109]. The analysis is commonly achieved by applying temporal correlation functions:

$$G(\tau) = \frac{\langle I(t)I(t+\tau) \rangle}{\langle I(t) \rangle^2} - 1 \quad (3.1)$$

Fluorescence intensity fluctuations are usually measured by means of a confocal microscope system that ensure a microscopic detection volume of about 10^{-15} L (1 femtoliter) defined by a tightly focused laser beam (Fig 3.1.A). Fluorescence intensity fluctuations measured by FCS represent changes in either the number or the fluorescence quantum yield of molecules resident in the detection volume. The time-dependent fluorescence intensity $I(t)$ (Fig. 3.1.B) is then analyzed in terms of its temporal autocorrelation function ($G(\tau)$) Eq. 3.1, which compares the fluorescence intensity at time t with the intensity at $(t + \tau)$, where τ is a variable interval, averaged over all data points in the time series. The calculated autocorrelation function (Fig. 3.1.C) contains information about equilibrium concentrations, reaction kinetics and diffusion rate of molecules in the sam-

ple [110]. Despite its fifty years, FCS is still applied in several biological and physical field for its robustness and fastness. However, the retrieved information that FCS provides it is confined to the confocal observation volume and describes only the temporal evolution of the correlation function. More recently, thanks to the coupling of spectroscopy techniques with scanning confocal microscopes, the spatial dimension has been explored and several techniques have flourished starting from the FCS founding principle. Image Correlation Spectroscopy (ICS), for instance, operates on image stacks and globally refers to the ensemble of simultaneously detected molecules and a great amount of data can be rapidly extracted due to the high statistics. From ICS, related methods have been developed, such as Raster Image Correlation Spectroscopy (RICS) [111], Temporal and Spatio-Temporal Image Correlation Spectroscopy (TICS and STICS respectively) [112, 113], ν -space ICS [114] and, more recently in my laboratory, *image-derived* Mean Square Displacement (*i*MSD) [63, 64]. *i*MSD, in particular, combines the temporal and spatial information by providing the molecule/organelle mode of motion and diffusion coefficient (or velocity, in case of directed motion) and structural information (i.e. the average size of the fluorescent species) related to the objects under study.

3.2 THE *i*MSD APPROACH.

3.2.1 *i*MSD extracted parameters.

*i*MSD is based on the rapid calculation of the mean square displacement (MSD) (commonly used in Single Particle Tracking, SPT) directly for imaging of many molecules at the same time, with no need to dwell on any of them. With respect to SPT, in which particles must be isolated and distinguishable, the *i*MSD algorithm works well also under the typical experimental conditions met with FP-tagged molecules and live cells (i.e., high particle density, low signal-to-background ratios). Therefore, the *i*MSD final outcome (i.e. a plot in time of the average particle displacement) resembles that obtained from SPT technique and can be used to reconstruct the (average) particle diffusion law and extract quantitative information on it. First, fast imaging of the region of interest is performed (Fig. 3.2.A). Then, recorded acquisitions corresponding to increasing time delays are correlated (i.e., each 2, 3, n-repetitions). For each time delay, the average of the spatial correlation function is calculated by using the same mathematical basis of

the STICS method (for mathematical details see Appendix A, Methods). However, since its introduction, the STICS approach was mainly used in conjunction with frame rates in the "seconds" time range. This in turn allowed accurate measurement of only slow protein fluxes (i.e., magnitudes of $\mu\text{m}/\text{min}$) such as those from retracting lamellar regions and protrusions for adherent cells, but neglected (fast) diffusive components [115, 116].

As thoroughly described in *iMSD* section of Appendix A, if particles diffuse, the width of the correlation central peak increases with increasing time delay between frames (Fig. 3.2.B). This peak can be fitted with a Gaussian function (Fig. 3.2.C), whose variance ($\sigma_r^2(\tau)$) represents the particle Mean Square Displacement directly extracted from imaging, with no need to extract and analyze individual single-particle traces. Thanks to the *iMSD* vs. time plot (Fig. 3.2.D), a diffusion laws can be directly identified with no need for an interpretative model or assumptions about the spatial organization of the system. By fitting the *iMSD* curve different diffusion modes can be evaluated and can be described by diffusion coefficient (D) and anomalous coefficient (α). If particles are diffusing isotropically with diffusivity "D" the retrieved *iMSD* is linear in time with a slope that depends on the diffusion coefficient and the value of α is equal to 1. If particles are diffusing in a meshwork where multiple adjacent domains of variable size (L) are separated by impenetrable barriers, i.e., particles can freely diffuse inside each domain with diffusivity D_{micro} (D_m) but cannot jump to adjacent domains (probability to jump, $P = 0$). In this case, the *iMSD* plot saturates to an asymptotic value that depends on the confinement area and α coefficients will have values below 1. In a living cell, however, more complex diffusion models respect to the latter can be present: for example, a partially confined diffusion behavior. In this case particles diffusing within the mesh with diffusivity D_m are also able to cross the boundaries with probability $P > 0$, thus generating a new "long-range" diffusivity, D_{macro} (D_M). Again, in this case the α coefficient will have values below 1 (Fig. 3.2.D). The last case occurs when particles are moving along cell-tracks (i.e. microtubules). This case, called superdiffusive behavior, *iMSD* plot presents a hyperbolic trend and is characterized by an anomalous coefficient α with value above 1. Moreover, a distinguishing feature of *iMSD* is that it yields aforementioned dynamic information combined with the average size of the moving objects [64, 65]. For molecules, the resulting size extracted from *iMSD* analysis correspond to the confocal Point Spread Function (PSF) but, when the particle under study has more than one fluorophore and its size is not negligible (e.g., large protein clusters, vesicles, etc.), the correlation

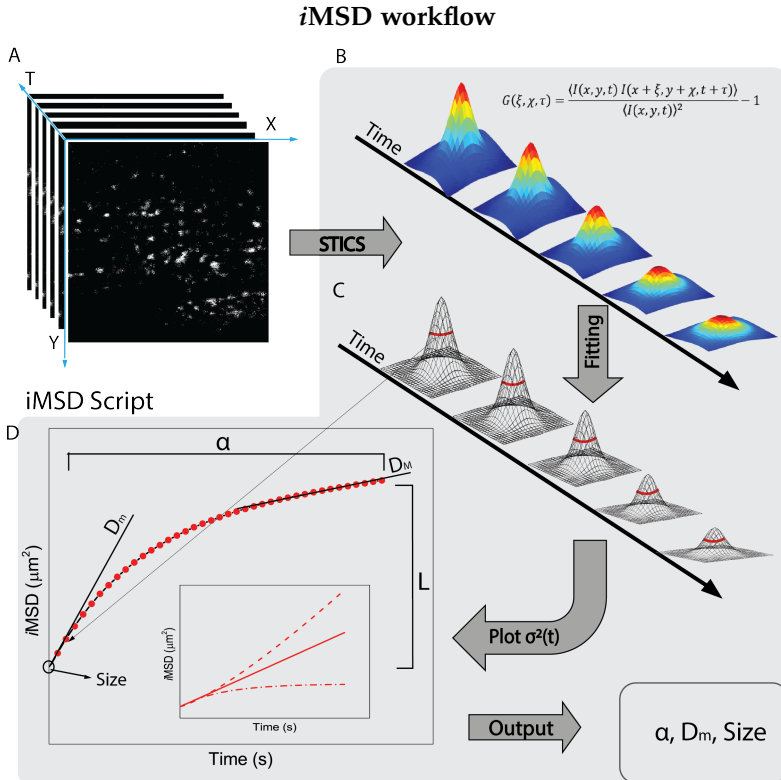


FIGURE 3.2: **A)** Stack of intensity images of a fluorescently labelled intracellular organelles by time-lapse confocal microscope in living cell. **B)** Temporal evolution of the spatiotemporal correlation function calculated according to STICS analysis. **C)** 2D Gaussian fitting of each spatiotemporal correlation function. The depicted red segment represents the variance of the fitted Gaussian function. **D)** example of *i*MSD plot. Fitting procedure can be used to retrieve structural and dynamic parameters of labelled organelles, such as Size, D_m , D_M , anomalous diffusion coefficient α and confinement length L . On the inset, representation of three exemplary mode of motion: super diffusion, dashed red line; isotropic diffusion, solid red line; sub diffusion, dashed-dot red line. **E)** Three relevant parameters: α , D_m and Size are used to define the position of the cell-based acquisition in a 3D parametric space.

function at $t = 0$ include also the spatial extension of the object itself, i.e. the σ_0^2 value can be used to extract the apparent average size of the imaged particles (further details in Appendix A Methods and Appendix B).

3.2.2 *Application of iMSD: from molecules to proteins, from nanoparticles to organelles.*

In Di Rienzo *et al.* [64] *iMSD* was first presented with its theoretical framework and with an application on transmembrane diffusing Transferrin Receptor imaged with a total internal reflection fluorescence (TIRF) microscope. *iMSD* application has permitted to understand better the plasma membrane organization, mostly in terms of its interaction with the underneath cytoskeleton meshwork. Studies on other membrane components, such as that glycosylphosphatidylinositol (GPI) [64] or transmembrane receptor TRPV-1 [117] are followed, providing a deeper knowledge on how these molecules interact with membrane and cytoskeleton components in very fast timescale (μs). In latest *iMSD* applications, the structural and dynamic properties of entire organelles or nanoparticles were explored. First, lipid-based nanoparticles [65], then organelles involved in principal endocytic ways [65, 118] [121] were studied in terms of the evolution of their dynamics properties during endocytosis but also from a structural point of view: since organelles are not sub-resolved structure (i.e. average dimensions are bigger than a conventional PSF of a confocal microscope) average size can be obtained by y-axis intercept of *iMSD* plot and can be used, in a comparative strategies, coupled with diffusion coefficient and anomalous coefficient to build a "fingerprint" describing the structural and dynamics properties of an organelle.

3.3 APPLICATION OF *iMSD* TO INSULIN SECRETORY GRANULES.

The proper intracellular function of ISGs depends on both structural (e.g. size) and dynamic (e.g. diffusion mode) properties [15]. Defects in granule structural/dynamic properties are recognized hallmarks of pancreatic β -cells dysfunction such as those found under hypercholesterolemia conditions [55]. Despite the importance of these ISG properties, no currently utilized method provides simultaneous, rapid, and robust access to both structural and dynamic information of ISGs in living cells. Electron microscopy achieves high spatial resolution at the expenses of dynamic

information (and can be prone to fixation artifacts) [56]. On the other hand, approaches such as SPT provide valuable dynamic information but typically underexploit the structural one. These methods are also limited by the time-consuming extraction of trajectories and challenges inherent with a crowded 3D environment where many objects are packed within the microscopy resolution limit [58, 60, 62]. In the rest of the Chapter, optimization and validation steps for the application of *i*MSD analysis on ISGs dynamics are presented. Exploiting its principal features, *i*MSD provides the simultaneous estimation of the structural (size) and dynamic (diffusivity and mode of motion) properties of granules with high temporal resolution at the expense of distinguishing local heterogeneities, yielding quantitative information at the whole-cell level.

3.3.1 Workflow of the experiment.

The workflow from time-lapse imaging of ISGs to the derivation of their structural/dynamic properties is described for a typical experiment on labelled ISGs in Figure 3.3. ISGs are labelled with a transient transfection of pro-insulin-EGFP (in which EGFP is attached to the C-peptide) into INS-1E cells as a standard procedure to obtain fluorescent, functional granules (punctate staining in Fig 3.3.A): after the intra-granular enzymatic processing, the granules contain a dense core of insulin and EGFP-tagged C-peptide [20]. Then, a stack of images is obtained from a $12 \times 12 \mu\text{m}$ region of interest (Fig. 3.3.B) at ~ 200 ms/frame for at least 100 seconds, while keeping photo-bleaching under control (Fig. 3.4).

The spatiotemporal correlation function is calculated by comparing acquired images at increasing time delays (Fig. 3.3.C) following standard spatio-temporal image correlation spectroscopy (STICS) procedures [113] as described in Appendix A (Methods). The width of the peak of the spatial autocorrelation function increases at increasing time delays as a function of the movement of the fluorescent ISGs. As can be seen in Fig. 3.3.D inset, ISGs average displacement is linear in time only at very short spatiotemporal scales while it substantially deviates from linearity for larger scales.

The initial linearity behavior means that is possible to define a short-range diffusion coefficient, namely D_m , evaluated for $\tau \rightarrow 0$ in the *i*MSD curve [64]. This parameter, together with other two, describes the ISG local diffusive properties. In addition, from *i*MSD we routinely extract: (i) D_M , that depends on the time window analyzed (Fig. 3.5)); (ii) the anomalous

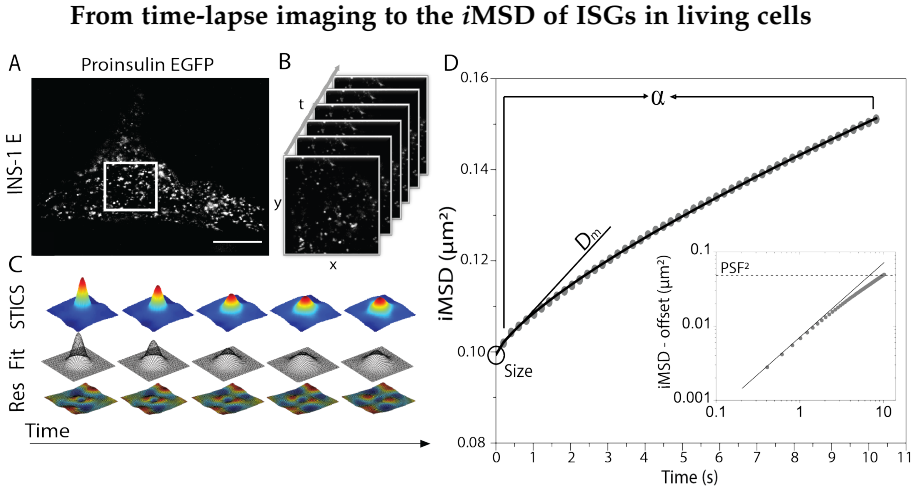


FIGURE 3.3: **A)** Confocal image of an INS-1E cell transfected with pro-insulin-EGFP: the visible punctuated pattern represents the ISGs containing the GFP-tagged C-peptide fragment. **B)** Acquisition of a cytoplasmic region (white square in (A)), consisting of 500 frames at 200 ms/frame, 256x256 pixels. **C)** Temporal evolution of the spatiotemporal correlation function obtained by STICS analysis performed on the stack of images in (B) (top row), with Gaussian fits and residuals (middle and bottom rows). **D)** *i*MSD curve obtained by Gaussian fitting of the spatiotemporal correlation functions representing the average diffusion law of the whole population of captured ISGs. The inset contains a log-log plot of the same data. For each experimental curve, values of α , D_m and size are extracted by fitting procedures.

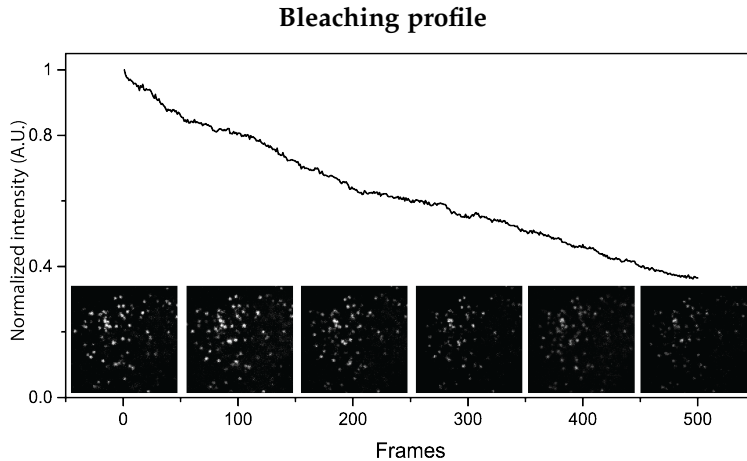


FIGURE 3.4: Normalized intensity fluorescence counts of a typical acquisition of transfected ISGs versus frames progression/time, with exemplary images extracted from the acquired movie, at frame $n=0, 100, 200, 300, 400, 500$.

coefficient also known as α , which describes the mode of motion of the dynamic object; and (iii) the y-axis *i*MSD curve intercept σ_0^2 (subtracted in the inset of Fig. 3.3.D), which yields the average apparent size of dynamic objects (i.e. the actual size convolved with the instrumental PSF).

3.3.2 *The importance of temporal resolution and pixel size.*

A few considerations to assess if the chosen temporal resolution is adequate to retrieve properly spatial and dynamic properties of ISGs in their native condition. If the time resolution of imaging is appropriate, ISGs will appear as "immobile" within each captured frame, i.e. it will display a characteristic size that, on average, is not deformed due to the imaging speed. In this sense, a limit condition can be reached by fixing the sample, i.e. by artificially immobilizing labelled ISGs. This condition can be used as a reference to obtain the expected organelle size under the imaging conditions chosen (e.g. laser wavelength, pixel size, objective, etc.). This is shown in Fig. 3.6 along with an acquisition performed in live cells at the desired temporal resolution (i.e. 200 ms/frame, Fig. 3.6.B), and with an acquisition performed intentionally at slow speed (i.e. 10 sec/frame, Fig. 3.6.C). Thus, it is reported a quantification of granules' sizes directly from

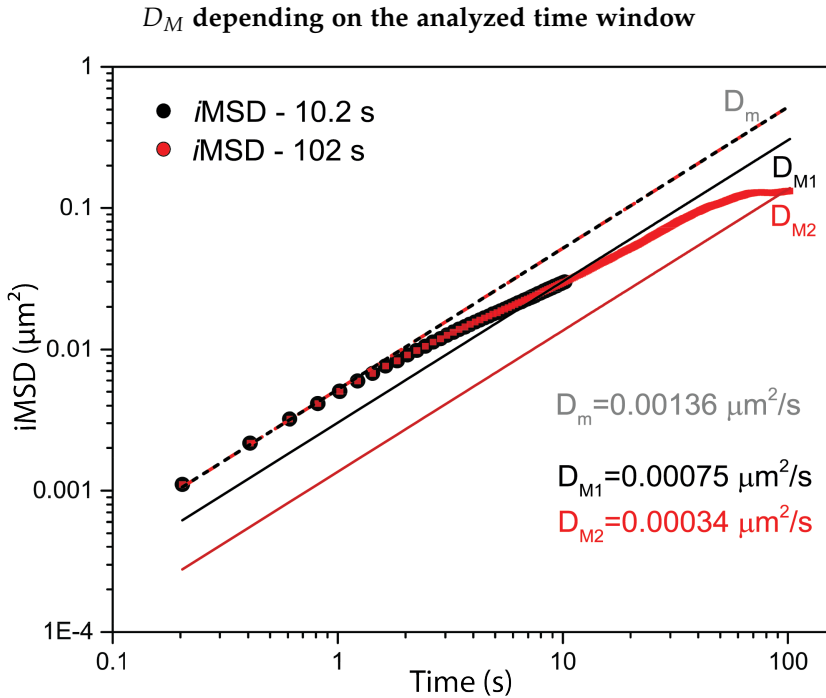


FIGURE 3.5: Two $iMSD$ curves of different duration (10.2 s, black dot and 102 s, red dot) are represented in log-log scale. Both curves are characterized by the same value of D_m (short range diffusivity) coefficient, represented by tangent red and black dashed line, while they differ for D_M (long range diffusivity) coefficients, represented by tangent black solid line for shorter curve and tangent red line for the longer one.

the optical microscopy images (Fig. 3.6.D). In particular, the size of each organelle/structure in the image is extracted by means of ImageJ software. For each spot of imaged ISGs, intensity profile is plotted and fitted with a Gaussian function to obtain Full Width at Half Maximum (FWHM) value that can be assumed as estimation of spot diameter. As expected (Fig. 3.6.E), the acquisition performed at an appropriate temporal resolution (200 ms) yields a characteristic size of the structure of interest that closely resembles that obtained from the fixed sample, either by using the standard tool described above or the *i*MSD *y*-axis intercept.

By contrast, the artificially slow acquisition yields a substantially enlarged apparent size of the same structure, due to its substantial movement during imaging. Under these latter experimental conditions, both the structural and dynamic information embedded into the time-lapse acquisition do not faithfully describe the intrinsic properties of the structure of interest. Concerning the spatial dimension, it was chosen to oversample the available PSF of the laser beam with an appropriate pixel size, i.e. at least 3–5 times smaller than the PSF.

3.4 THE *i*MSD-BASED ISG STRUCTURAL-DYNAMIC FINGERPRINT.

Finally, defined the proper experimental parameters for live cell imaging, C-peptide-EGFP-tagged ISGs are imaged and analyzed by the *i*MSD algorithm. Each obtained *i*MSD trace is calculated up to time-lags with a maximum length corresponding to 10% of the total acquisition time (~ 10 seconds in my measurements), as this satisfies statistical criteria for *i*MSD calculation [112]. The aforementioned three parameters extracted from traces of 107 cells (Fig. 3.7.A) are analyzed to provide the histogram distributions of whole-cell-populations acquisitions (Fig. 3.7.B).

Interestingly, the average structural/dynamic parameters are invariant as a function of the amount of C-peptide-EGFP expressed by INS-1E cells, as can be seen in scatter plots of Fig. 3.7.C in which fluorescent intensity analysis was performed for each acquired movie and plotted versus structural or dynamic parameters retrieved from *i*MSD fitting. Please take in mind that this property (i.e. structural and dynamic properties invariant with respect to tag concentration) will be crucial in our analysis of the influence of fluorescent labelling on granule properties (addressed in the next Chapter). The data extracted from *i*MSD analysis can be visualized graphically as a multivariate 3D distribution for σ_0^2 , D_m , and α parameters

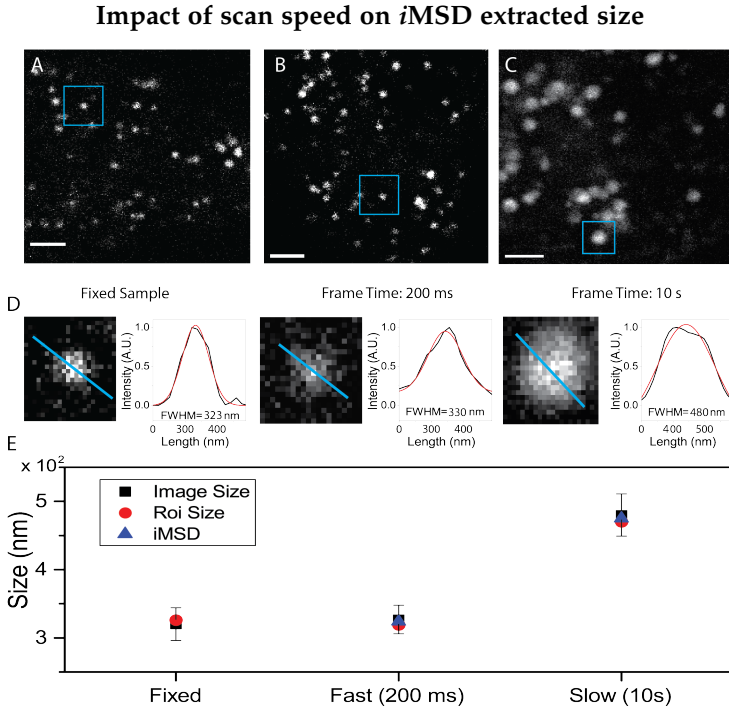


FIGURE 3.6: **A)** Exemplary image of fluorescently labelled ISGs in a fixed sample. Scale bar: $2 \mu\text{m}$. **B)** First frame of a stack of images of ISGs in a living cell, acquired with the appropriate parameters. Temporal resolution: 200 ms/frame. Scale bar: $2 \mu\text{CAZZOm}$. **C)** First frame of a stack of images of ISGs in a living cell, acquired at low speed: artifactual deformation of the apparent ISGs size due to organelles motion during imaging is clearly visible. Temporal resolution: 10 s/frame. Scale bar: $2 \mu\text{m}$. **D)** Example of size calculation for imaged ISGs in blue ROI of (A), (B) and (C). The intensity profile along the blue line was fitted with a Gaussian function to retrieve the FWHM, i.e. an estimate of spot size. FWHM values are reported for each fitting. **E)** Graphical representation of size values obtained by image analysis described in panel (D) for all imaged ISGs (black square, mean value and standard deviation), for ISGs enclosed within the blue ROI (blue triangle) and retrieved by *i*MSD analysis (red circle).

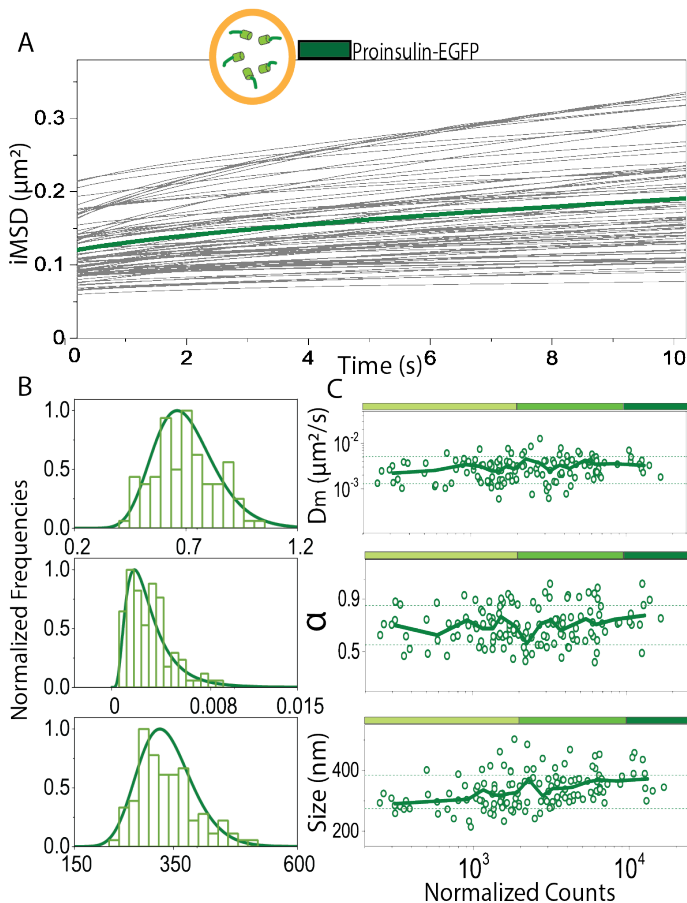
From single *i*MSD traces to whole-cell-population analysis

FIGURE 3.7: **A)** *i*MSD curves from 107 cell acquisitions of proinsulin-EGFP expressing INS-1E cells with the average highlighted in bold green. **B)** Normalized relative distributions of D_m , α , and size parameters. **C)** Protein expression level analysis. Each point in the plots associates, for each acquisition, the obtained value of D_m (top), α (middle), and size (low panel) with the protein expression level (expressed in fluorescence counts). Solid green lines represent the average values calculated for each parameter, plus/minus standard deviation (dashed green lines). Solid green lines are calculated by averaging data points with a floating window corresponding to 8 experimental points.

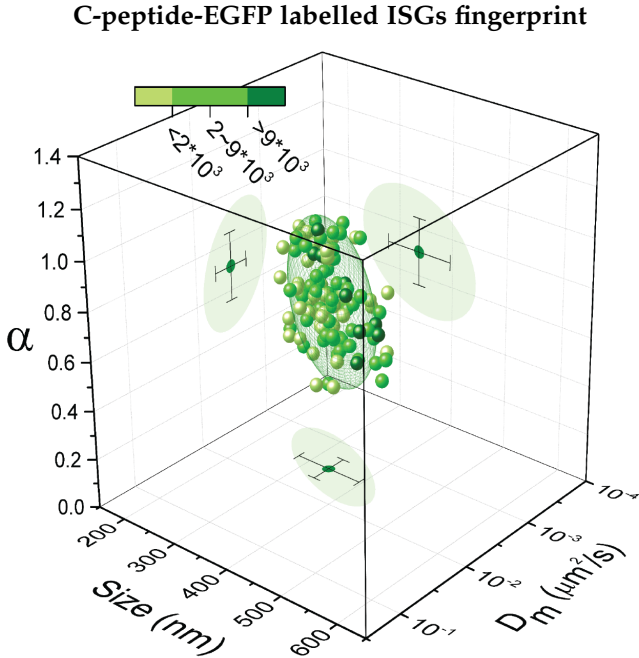


FIGURE 3.8: Structural and dynamic properties of ISGs labelled with proinsulin-EGFP represented as a scatter plot in which the three values of α , D_m and size of each acquisition are organized in a 3-D parametric space. Darkness of the color represents the fluorescence expression level. The 3D-plot projections of data points show the confidence ellipsoids of average values and SD.

for the population of analyzed cells (Fig. 3.8). By diagonalizing the covariance matrix of the distribution, a confidential ellipsoid was defined that can be regarded as the 3D analog of the confidence interval (mean \pm SD) for 1-D distributions. This allows a global statistical analysis on whole-cell-population data based on the Mahalanobis [119] approach (see Appendix A, Methods for further details). In brief, two distributions with the same mean values have a "statistical cluster distance" (SCD) equal to 0, independently of their covariance matrices. If the average values are different and the corresponding ellipsoids intersect each other, then $0 < SCD < 1$. If the ellipsoids are externally tangent, then $SCD = 1$. If the distributions are far enough that there is no intersection between the ellipsoids, then $SCD > 1$.

Labelling	Size (nm)	D_m ($\mu m^2 / s$) $\times 10^{-3}$	α	N	SCD
C-peptide	335 \pm 56	3 \pm 1.7	0.7 \pm 0.1	107	/
C-peptide + Chol	472 \pm 97	11 \pm 7	0.3 \pm 0.3	71	0.54
C-peptide + Low	335 \pm 64	2 \pm 1	0.6 \pm 0.1	58	/*
C-peptide + High	357 \pm 61	4.6 \pm 3.2	0.7 \pm 0.1	54	0.42*

Summary of *i*MSD-derived parameters

TABLE 3.1: *SCD, statistical cluster distance is calculated between ISGs labelled by C-peptide-EGFP between INS-1E cells in low- and high-glucose medium.

3.5 FINGERPRINT VALIDATION.

Average values and standard deviation of size, D_m and α for C-peptide-EGFP ISGs are reported in Table 3.1. In particular, the average apparent ISG size calculated from my experiments is 335 ± 56 nm. The average granule isotropic diffusion at a short spatio-temporal scale is $D_m = (3.2 \pm 1.7) \times 10^{(-3)} \mu m^2 / s$ and the average anomalous coefficient α is equal to 0.70 ± 0.14 , indicating a sub-diffusive behavior. These values are validate "internally", testing whether *i*MSD analysis was capable to highlights changing in spatial and dynamics behavior after cell treatments known to affect granule dimension and/or diffusivity (i.e. cholesterol overloading or glucose stimulation); and with other techniques able to retrieve same spatial and dynamic parameters that *i*MSD: i.e. for size validation TEM measurement and tracking analysis for diffusivity.

3.5.1 Validation of *i*MSD by standard SPT analysis.

Particle tracking affords, as mentioned in Chapter 1, an impressive amount of detailed information in the form of single-object positions in time and space (i.e. trajectories) captured during the experiment (Fig. 3.9.B-C). *i*MSD, instead, as any other fluctuation-based analysis method, provides average information on single diffusing objects, without dwelling on any of them in particular. As such, the *i*MSD plot presented here (Fig. 3.9.D-E) should be considered as the average diffusion law of all the sub-cellular fluorescent organelles/structures captured by imaging, during the whole acquisition and obtained with no need to extract trajectories. As such, we expect it to be coincident (in terms of the overall shape of the diffusion law)

to the standard MSD calculated starting from all single-object trajectories (this is clear from the comparison of traces in Fig. 3.9.C-E). Moreover, as any FCS technique, *i*MSD could in principle have a bias towards large and bright objects. In fact, as purely statistical method, in presence of different sub-population behaviors, brightest and biggest granules could, as average, induced an overestimation of the native granule properties. This issue concerning the granule measurements was carefully addressed extracting single granule sizes and intensities from the confocal images to build a plot of size vs intensity (Fig. 3.10). This is already showing that the granules are not unevenly distributed, i.e. brighter granule are, for instance, both small and large. Still, the brighter/larger granules could be weighted more in the calculation of the diffusivity as compared to the other ones. Thus, for each localized spot (granule) the trajectory was computed by the standard SPT algorithm and, from the trajectory, the local diffusivity was calculated. Then, points in the plot of Fig. 3.10 were color-coded according to the measured D (diffusion) value. As can be seen, once the dynamics is calculated, no clear correlation is found between size/intensity and diffusivity. In other words, no substantial bias in the estimate of granule diffusivity can be introduced if large/bright objects are yielding diffusivities distributed spanning a wide range of values, from low to high.

Previous results on granule trafficking in live cells are also available in literature, although these data typically rely on either confocal-microscopy- or TIRF-based granule imaging and tracking with variable temporal resolutions, i.e. in the 1-200 Hz range [58], [59–62, 120]. Considering only previous works based on proinsulin/C-peptide-FP labelling it can be found, for example, that Tabei and co-workers [58] investigated intracellular granule dynamics by spinning-disk microscope (and reported diffusion values similar to mine). They described ISGs intracellular motions as a subordinated random walk (i.e. sub-diffusion) over the time scale of 1-100 seconds. This is consistent with my results using the *i*MSD both in terms of average anomalous coefficient ($\alpha < 1$, indication of sub-diffusive behavior) and of the overall shape of the granule diffusion law. Also, Heaslip [59] and co-workers addressed granule dynamics by SPT and reported D values almost coincident with the one I found (about $2 \times 10^{-3} \mu\text{m}^2/\text{s}$).

It is interesting to note that, in another work of [60] higher D values were observed. But, in their relevant paper on aged insulin granules the authors report on the co-existence in the cell cytoplasm of three granule components, defined as "highly dynamic" ($D \sim 10^{-2} \mu\text{m}^2/\text{s}$), "restricted" ($D \sim 10^{-3} \mu\text{m}^2/\text{s}$), and "nearly immobile" ($D \sim 10^{-4} \mu\text{m}^2/\text{s}$), with the latter

Example of typical acquisition of transfected ISGs

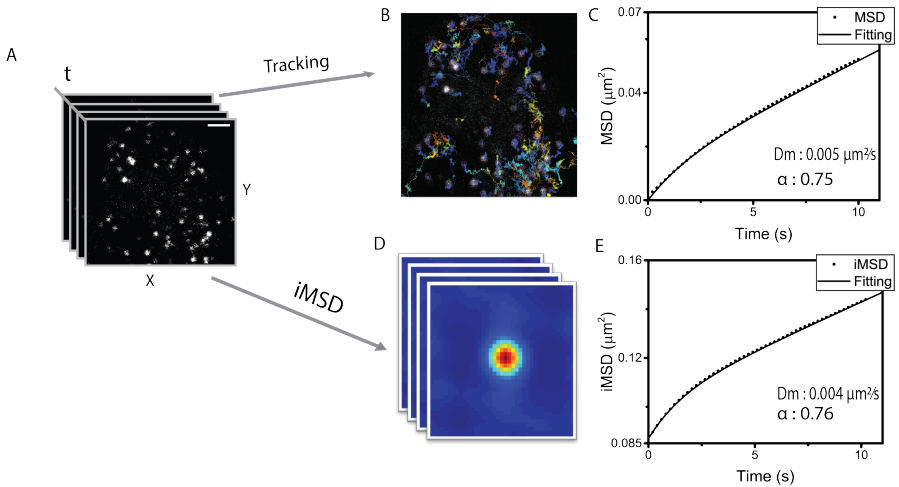


FIGURE 3.9: **A)** Example of typical acquisition of transfected ISGs (scale bar: $5 \mu\text{m}$). **B)** Representation of trajectories of each granule superimposed to the first frame of the movie, extracted by TrackMate analysis on ImageJ. **C)** MSD curve obtained by analyzed tracks. Fitting with same equations describe in Methods lead to reported values for D_m and α coefficients. **D)** Stack of images representing the evolution of the spatio-temporal correlation function (STICS), obtained by *iMSD* custom made Matlab algorithm (as described in Methods). **E)** *iMSD* curves obtained for movie in (A). Fitting procedures lead to reported values, in agreement to tracking-based retrieved ones.

Impact of high mobility and brighter granules on *i*MSD analysis

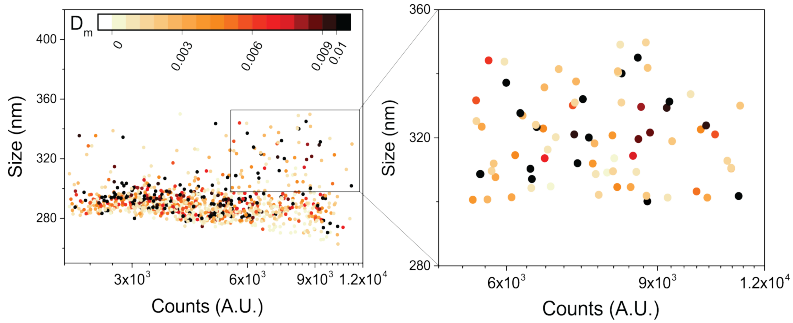


FIGURE 3.10: Each point in the scatter plot represent a specific localized ISGs for which fluorescence intensity, size, and D_m were estimated by trajectories analysis ($n=4$ acquisitions). Darkness of the color represents the increasing value of D_m coefficients calculated by tracking analysis. On the right, zoomed region of the scatter plot populated by bigger and more intense ISGs.

two populations being the more abundant. It is thus somewhat expected that doing the average of the whole population by *i*MSD I obtained an overall D value that is in the order of 10^{-3} , i.e. in the same order of magnitude as that reported in this thesis for C-peptide-EGFP labelled ISGs.

3.5.2 Validation of *i*MSD-derived granule size by TEM.

First of all, it is important to note that a consistency between the granule size derived from optical (super-resolution) microscopy and that derived by TEM was already proved by others [55, 56]. Yet, new TEM experiments were performed on our experimental system. Nicely, TEM-based direct measurement of granule size in INS1-E cells matches *i*MSD-based estimates of the same parameter. *i*MSD-based size of C-peptide-EGFP-labelled ISGs must be considered as an apparent size, since, as any imaging measurement in a confocal microscope, is affected by convolution of the object size with the size of the instrumental PSF. For this reason, a direct comparison between granules size extracted by *i*MSD and TEM image analysis is impossible. But, as described in Appendix B, the analytical procedure for PSF deconvolution yields an average actual size of ISGs in INS-1E cells of about 220 nm, in good accordance with direct TEM-based quantification of ISG size performed here (215 ± 39 nm, from the analysis of $N = 104$ single granules

TEM micograph of ISGs

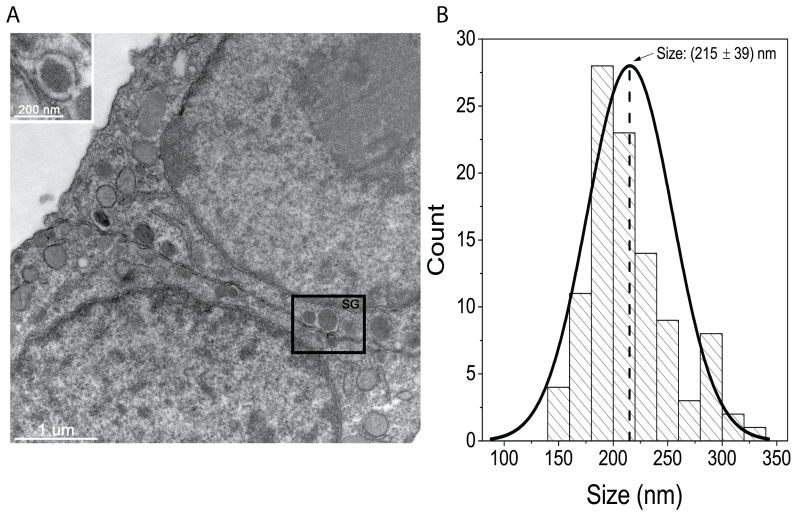


FIGURE 3.11: **A)** Micrograph of INS-1E cells. Granules (SG) are dense core structure with a well-defined outer membrane (inset). **B)** Diameter (size) distribution of $n=104$ analyzed granules. Mean value and standard deviation of the distribution are reported.

in EM micrographs; Fig. 3.11) and by others [56] on the same cell line. For simplicity, hereafter the apparent sizes directly extracted as y-axis *iMSD* intercepts (σ_0^2) will be used to compare ISG structural properties across different conditions.

3.5.3 Functional validation of *iMSD*-derived parameters: glucose stimulation.

Two experimental conditions were considered to validate the sensitivity of the *iMSD*-based measurements of granule structural/dynamic properties. First, the cell culture was switched from low (2.8 mM) to high (16.7 mM) glucose concentration. Previous SPT measurements [59] has shown that granule deployment upon glucose stimulation is the result of two main effects: a 1.5-fold increase in local granule diffusivity combined with an increase in their anomalous coefficient. Data from *iMSD* analysis are consistent with these findings, in fact as can be observed in Fig. 3.12 and reported in Table 3.1 that α coefficient switch from 0.67 in low glucose

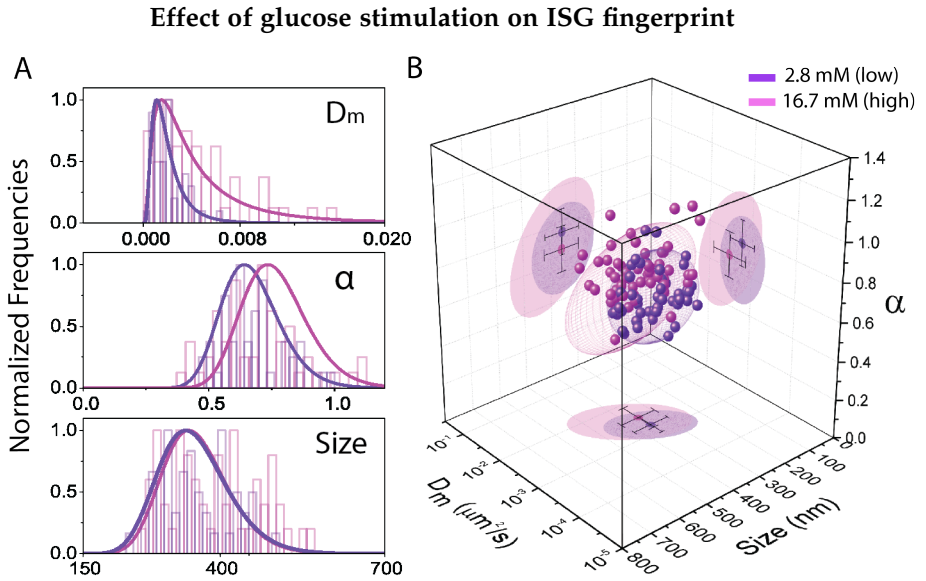


FIGURE 3.12: **A)** Normalized relative distributions of D_m , α and size for low glucose (violet bars and fit) condition compared to high glucose condition (magenta bars and fit). **B)** Dynamic fingerprint of proinsulin-EGFP ISGs in low glucose medium compared to pro-insulin-EGFP ISGs in high glucose medium.

medium to 0.76 after glucose stimulation; also D_m coefficient increases after the stimulus, in keeping with recent findings in literature.

3.5.4 Functional validation of iMSD-derived parameters: cholesterol overloading.

An additional functional validation was made by exposing the cells to high concentrations of cholesterol. Cholesterol is an essential component of cell membranes and contributes to the control of their physical properties (such as fluidity and curvature), which in turn affect plasma membrane proteins function (i.e. transporters, ion channels and receptors) as well as vesicles formation and fusion. These aspects are also critical for the correct function of pancreatic β -cells and factors influencing cellular cholesterol metabolism are believed to impact β -cell function and the pathogenesis of diabetes. TEM data showed that excess cholesterol is delivered specifically to insulin granules [55] causing, on average, a 1.5-fold granule enlargement.

Effect of cholesterol overload on ISG fingerprint

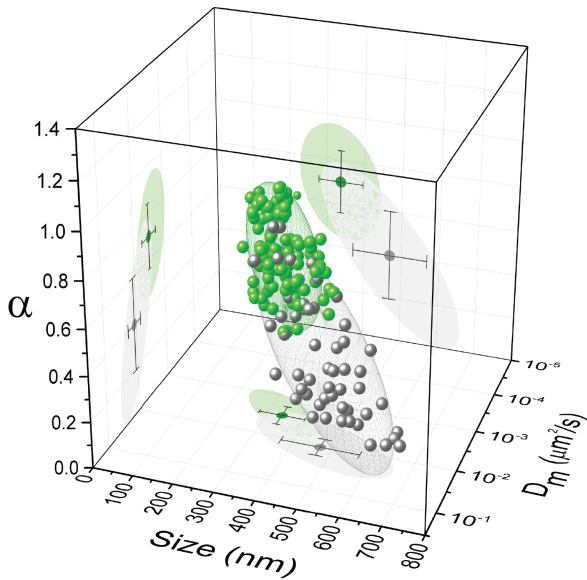


FIGURE 3.13: Dynamic fingerprint of Cholesterol-treated cells (grey dots) compared to untreated cells (represented as a 68% confidential ellipsoid in green).

Again, this is mirrored by the results from *i*MSD analysis: after 1h treatment with 5 mM cholesterol, ISGs increased 1.5-folds in size, in average (Fig. 3.13, Table 3.1). In my experiments, hypercholesterolemia also induces alteration of the granule dynamic behavior (4-fold increased D_m , 2-fold decreased α , Table 3.1). While this change has not been reported explicitly before, cholesterol-impaired granule trafficking is expected based on the observed retention of syntaxin 6, VAMP4, and clathrin in granule membranes [55].

3.6 CONCLUDING REMARKS.

Here, *i*MSD analysis has been first tuned for the precise purpose to study ISGs then applied to characterize ISGs structural and dynamic properties in living β -cells. The intraluminal fluorescent probe used, C-peptide-EGFP, reveals itself capable to label ISG without affecting its native features as demonstrated by several validation experiments. For this reason, C-peptide-EGP labelled ISGs has been used in the next chapter as reference and the generated structural-dynamic fingerprints (i.e. the triplets of parameters size, D_m and α coefficients) compared with the ones obtained by others fluorescent chimeric proteins used to label ISGs.

PROBING THE EFFECT OF FLUORESCENCE LABELLING ON GRANULE STRUCTURAL AND DYNAMIC PROPERTIES

Most of the content of this Chapter was peer-reviewed and published with co-authors in:

- Insulin secretory granules labelled with phogrin-fluorescent proteins show alterations in size, mobility and responsiveness to glucose stimulation in living β -cells. *Scientific Reports* (2019).

Ferri G., Digiacomio L., Lavagnino Z., Bugliani M., Cappello V., Caracciolo G., Marchetti P., Piston D.W., Cardarelli F.

- Probing the light scattering properties of insulin secretory granules in single live cells. *Biochem. Biophys. Res. Commun.* (2018).

Ferri G., Bugliani M., Marchetti P., Cardarelli F.

The commonly used strategy for granule labeling in living cells is based on genetically-encoded FPs tagged to intrinsic protein markers of the granule. A few granule-intrinsic proteins are available for this purpose: the C-peptide contained in pro-insulin (described in Chapter 1 and with *iMSD* analysis in Chapter 3), the islet amyloid polypeptide (IAPP) [121], the intraluminal zymogen granule protein, syncollin [122], and the phosphatidylinositol phosphatase transmembrane protein phogrin [123]. The first three proteins are localized within the granule lumen, while phogrin is a transmembrane protein. Despite their extensive use, little is known about potential overexpression artifacts of these labeling approaches on granule structural and dynamic properties. Before the presentation of *iMSD* analysis performed on differently labelled ISGs, in the next section of the Chapter the proteins used as fluorescent tag will be reviewed, in terms of their biology and principal information available in literature.

4.1 PROTEINS USED AS MOLECULAR MARKERS OF ISGS.

4.1.1 *IAPP*.

Islet amyloid polypeptide (IAPP or amylin) is a peptide hormone composed by 37 aminoacidic residues [121]. It is co-secreted with insulin in the ratio of approximately 100:1 (insulin:amylin) and, as insulin, it plays a role in glycemic homeostasis, regulating gastric emptying and satiety, thereby preventing post-prandial spikes in blood glucose levels. IAPP is processed from a 67 aminoacidic proislet amyloid polypeptide (pro-IAPP) that undergoes post-translational modifications including protease cleavage to produce IAPP mature form [124]. Inside granules IAPP, together with a large number of additional components, including the C-peptide, is found in the peripheral region of the granule [125] (Fig. 1.3). IAPP was first discovered through its ability to aggregate into pancreatic islet amyloid deposits, that are commonly found in pancreatic islets of patients suffering T2D or containing an insulinoma cancer [126, 127].

4.1.2 *Syncollin*.

The small 13 kDa secretory granule protein syncollin was first identified as a component of zymogen granules from the exocrine pancreas where forms oligomeric structures, most likely hexamer, associated with the luminal surface of the zymogen granule membrane [128, 129]. Syncollin is currently thought to play a role in the mechanism of zymogen granule exocytosis in the formation of an exocytotic fusion pore acting from the inside lumen of the granule [129]. Syncollin is not normally expressed in β -cells but, as demonstrated in Hays *et al.* [122], the induced expression of exogenous syncollin proteins indicated that these were specifically targeted to the lumen of insulin granules. Despite the correct localization, syncollin expression had significantly inhibited regulated insulin secretion stimulated by glucose. Intriguingly, a chimeric syncollin-FP (syncollin-EGFP) chimera was also efficiently targeted to insulin granules when expressed in β -cells but, unlike native syncollin, did not affect insulin secretion [122]. As such, syncollin-EGFP can be used as an experimental tool for tracking ISGs movement and exocytosis in real time [57, 130].

4.1.3 *Phogrin*.

Receptor-type tyrosine-protein phosphatase N2 (PTPRN2) also known as islet cell autoantigen-related protein (ICAAR) and phogrin (in rat and mouse) is an enzyme encoded by the PTPRN2 gene [131, 132]. PTPRN2 and the homologue PTPRN are both found to be major autoantigens associated with insulin-dependent diabetes mellitus. Phogrin is a transmembrane protein localized on the insulin granule's membrane (Fig. 1.3), it possesses an extracellular region, a single transmembrane region, and a single intracellular catalytic domain, and it is expressed in cells with stimulus-coupled peptide hormone secretion, including pancreatic β -cells and neurons but not in cells of the exocrine pancreas or in cells that lack a regulated secretion pathway [123]. Due to a close similarity in the gene sequences, the protein encoded by this gene has traditionally been considered a member of the protein tyrosine phosphatase (PTP) family. But it has shown that phogrin, dephosphorylates the lipid phosphatidylinositol rather than tyrosine [123]. Specifically, phogrin was shown to act upon phosphatidylinositol 3-phosphate (PIP3) and phosphatidylinositol 4,5-diphosphate (PIP2) and, therefore, must be considered a PIPase rather than a PTPase. PIPs play important roles in lipid signaling, cell signaling and membrane trafficking.

4.2 *i*MSD BASED APPROACH TO COMPARE ISGS' LABELLING STRATEGIES.

Here it is reported the *i*MSD-based analysis of ISGs labeled with aforementioned chimeric FP in INS-1E cells. The two intraluminal proteins (syncollin-FP and IAPP-FP) yield similar ISG properties in terms of average size and dynamics of labelled granules compared to the reference C-peptide-labelled ISGs, reported in green in all figures. (Table 4.1 and Fig. 4.1).

Data from these three labels show no clear dependence of granule structural and dynamic parameters from protein concentration. However, it is worth noting that high concentrations of IAPP-FP do elicit a slight increase of average granule size (Fig. 4.2.A). This is most likely related to toxic effects on cells, in accordance with what has been reported for COS-1 cells [133].

In contrast to the three intra-luminal proteins, transient over-expression of phogrin-EGFP produces a dramatic change in both the structural and dynamic properties of granules, which is readily evident with the *i*MSD

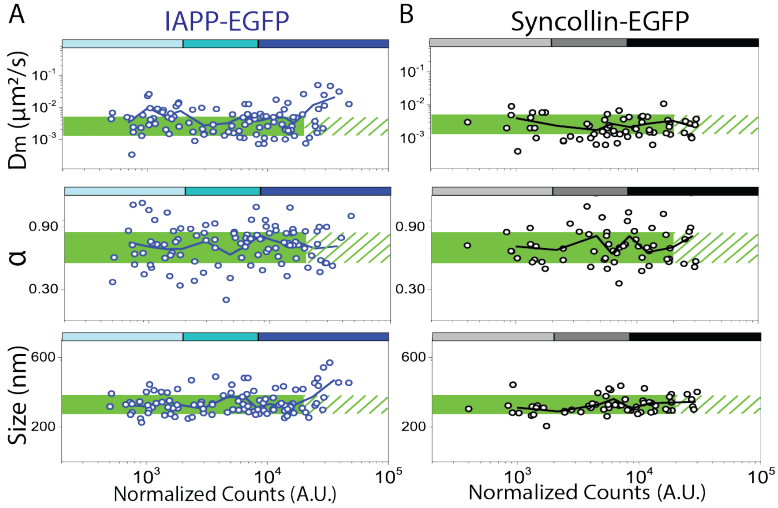
***i*MSD derived parameters of IAPP-FP and Syncollin-FP labelled ISGs**

FIGURE 4.1: **A)** Fluorescence expression level analysis, of IAPP-EGFP ISGs (blue), as described in Fig. 2.5. Green area in each plot is defined by average values plus and minus relative SDs of C-peptide-EGFP ISGs data. **B)** Fluorescence expression level analysis of syncollin-EGFP ISGs (black). Green area in each plot is defined by average values plus and minus relative SDs of C-peptide-EGFP ISGs data.

Labelling	Size (nm)	D_m ($\mu\text{m}^2 \setminus s$) $\times 10^{-3}$	α	N	SCD
C-peptide	335 ± 56	3 ± 1.7	0.7 ± 0.1	107	/
Syncollin	340 ± 60	2.4 ± 1.8	0.7 ± 0.2	48	0.157
IAPP	345 ± 73	5 ± 1.5	0.7 ± 0.2	103	0.33
Phogrin	420 ± 88	13 ± 6	0.5 ± 0.2	94	0.858

Summary of *i*MSD-derived parameters

TABLE 4.1: SCD, statistical cluster distance is calculated using as reference ISGs labelled by C-peptide-EGFP

Fingerprints of IAPP-FP and Syncollin-FP labelled ISGs

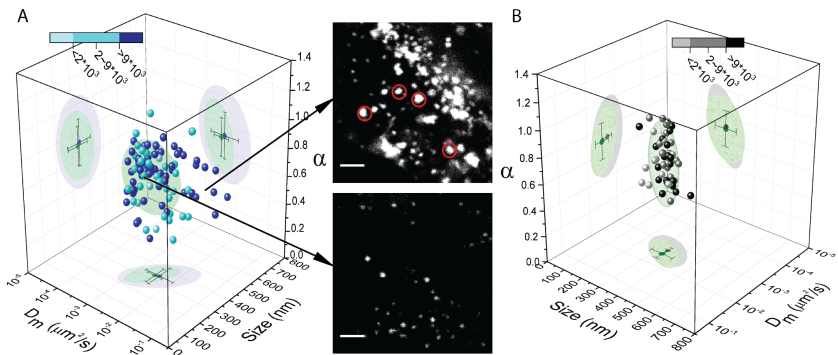


FIGURE 4.2: **A)** Structural/dynamic fingerprint of IAPP-labelled ISGs as compared to Proinsulin-EGFP reference. Points are color-coded as a function of the protein expression level. Examples of ISGs morphology alteration induced by high expression level of IAPP-Emerald, with exemplary ISGs highlighted in red or green of two distinct observable populations. Scale bar: $2 \mu m$. **B)** Dynamic fingerprint of syncollin-EGFP ISGs compared to proinsulin-EGFP ISGs dynamic fingerprint (represented as a 68% confidential ellipsoid in green). Color mapping is used to define three fluorescence expression regimes in which syncollin ISGs points are categorized.

analysis (Fig. 4.3.A). Cells expressing phogrin-EGFP show ISGs that are, on average, enlarged 1.2 folds as compared to C-peptide-EGFP-labelled ISGs (Table 4.1). These ISGs also exhibit a ~ 3 -fold higher D_m than C-peptide-EGFP-labelled ones (Table 4.1) and show a strong tendency to be confined by the intracellular environment, with $\alpha = 0.55 \pm 0.17$, as compared to $\alpha = 0.70 \pm 0.14$ of those labelled by C-peptide-EGFP (Table 4.1 and Fig. 4.3.B). Of note, these differences also depend on the phogrin-EGFP expression level (Fig. 4.3.C). At low phogrin-EGFP expression levels, in fact, the structural and dynamic properties of ISGs are similar to those of the C-peptide-EGFP reference, while alteration becomes clear above a certain concentration threshold for all the three parameters. This is evident in the 3D (Fig. 4.4) plot showing color-coded phogrin-EGFP expression levels, and average statistical distance between phogrin-FP and C-peptide-FP clusters (SCD, Table 4.1).

Worthy of note, a substantial increase in granule mobility in the presence of phogrin-FP can be also found in the literature, although it was not recognized as a direct effect of protein overexpression [61].

At this point, to better characterize these observations, I set out to perform a control experiment in which a mCherry-tagged variant of phogrin was co-transfected in INS-1E cells with C-peptide-EGFP and imaged in a two-channel time-lapse experiment (Figure 4.5).

Of note, the *i*MSD analysis of C-peptide-EGFP in these co-transfected cells exhibits enlarged and highly dynamic granules, revealing a dominant effect of the phogrin protein (yellow dots in the 3D plot of Fig. 4.5). The effect of phogrin-FP overexpression on granule size is likely due to the accumulation of transmembrane proteins. This may result in a physical perturbation of the membrane integrity above a critical concentration, similar to the conditions of cholesterol overload on the granule membrane observed here (see Fig. 3.13) or by others [55]. Please note that a similar concentration-dependent alteration of ISGs becomes visible also under stable-transfection conditions (Fig. 4.6). Worthy of mention, present results on granule enlargement are corroborated by analogous observations made by Durso *et al.* [118] on a different sub-cellular organelle, the lysosome, under over-expression of GFP-tagged transmembrane protein markers. The effect on granule dynamic properties, on the other hand, prompted us to speculate on a possible effect of phogrin-FP overload on the correct granule docking to the trafficking machinery (e.g. the cytoskeleton).

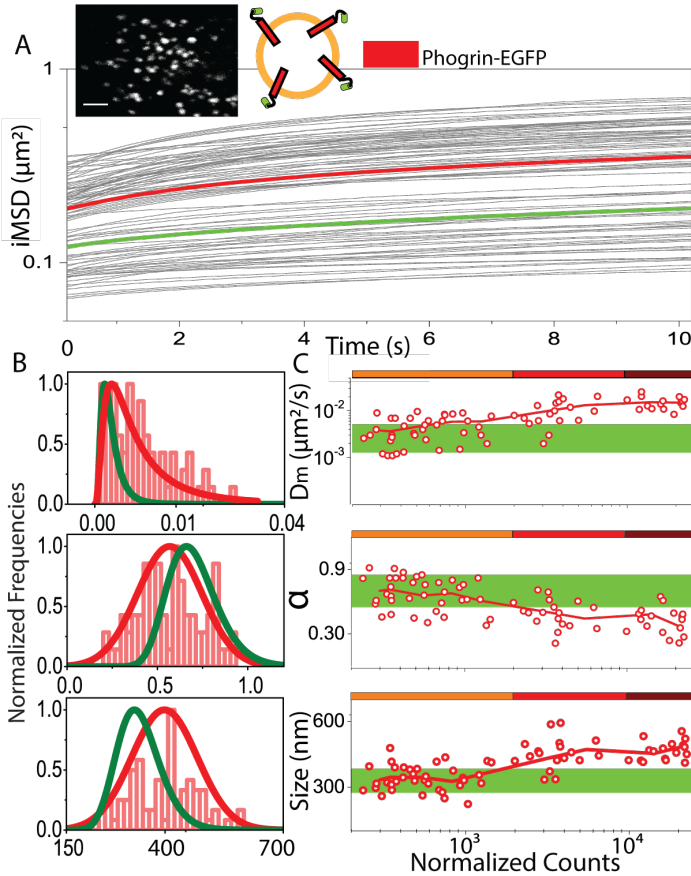
***i*MSD derived parameters of phogrin-FP labelled ISGs**

FIGURE 4.3: **A)** On top, example image of a phogrin-EGFP expressing cell (scale bar: $2 \mu\text{m}$) and schematic representation of fluorescent protein localization in phogrin-EGFP transfected ISGs. *i*MSD curves of $n=94$ acquisitions, with the average highlighted in bold red, as compared to the reference (from Fig. 3.7) in bold green. **B)** Normalized relative distributions of α , D_m and size for phogrin-EGFP expressing cells. **C)** Fluorescence expression level analysis. The green area in each plot defines the average position ($\pm\text{SD}$) of the proinsulin-EGFP reference. Each point associates the obtained value of D_m (top), α (middle) and size (low panel) with the protein expression level (expressed in fluorescence counts). Solid red lines are calculated by averaging data points with a floating window corresponding to 8 experimental points. The color-coded bars at the top of each graph indicate the three expression regimes used to classify data.

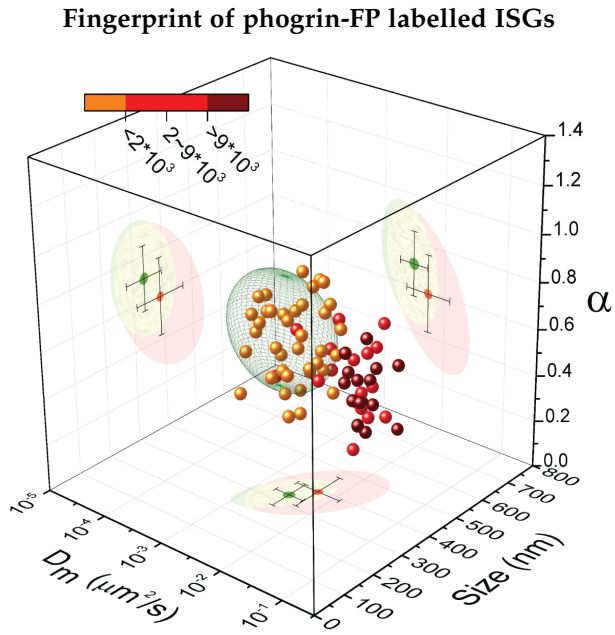


FIGURE 4.4: Structural/dynamic properties of phogrin-EGFP expressing cells as compared to the proinsulin-EGFP reference (represented as a 68% confidence ellipsoid in green). Points are color-coded as a function of the protein expression level.

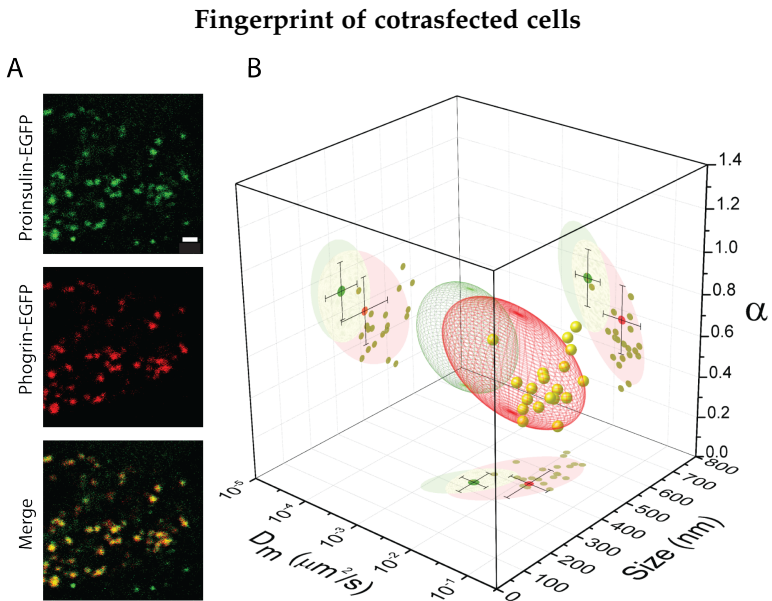


FIGURE 4.5: **A)** Co-transfection of phogrin-mCherry and proinsulin-EGFP (Scale bar: $2 \mu\text{m}$). **B)** Dynamic fingerprint of proinsulin-EGFP and phogrin-mCherryco-transfected ISGs (in yellow), compared to proinsulin-EGFP ISGs (68% confidential ellipsoid in green), and phogrin-EGFP ISGs (68% confidential ellipsoid in red).

Fluorescence expression level analysis of stably transfected cells

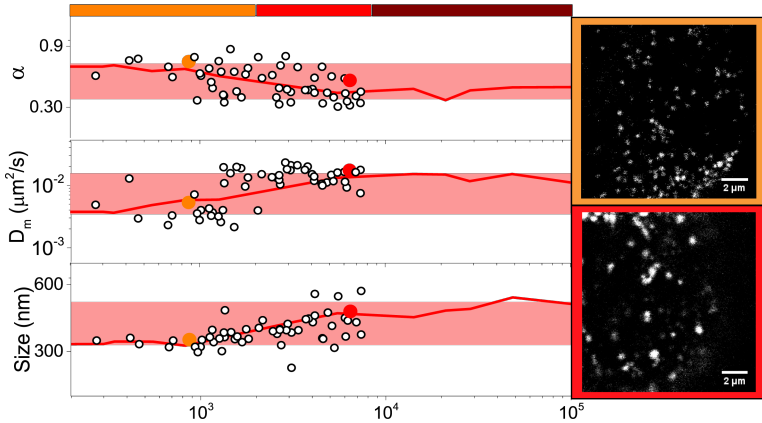


FIGURE 4.6: Fluorescence expression level analysis of stably phogrin-EGFP transfected cells (black points). The red area in each plot indicates the range of values (mean \pm SD) observed in cells transiently transfected with phogrin-EGFP (and reported in Fig. 4.3.C). For two exemplary expression levels two representative cells are highlighted in the plot (orange and red circles) and showed by confocal images on the right.

4.3 PHOGRIN OVEREXPRESSION EFFECT: POSSIBLE EXPLANATIONS.

Based on the strong mobilization observed in phogrin-FP labelled granules in comparison to the other labelling strategies, we were prompted to speculate if actin cytoskeleton could be involved in the phogrin-induced effect. Actin integrity was measured by using Phalloidin-647 in fixed cells in presence of different granule-specific proteins and experimental conditions (Fig. 4.7). In almost all the analyzed cells ($N = 30$), phogrin-FP expression induces extensive actin depolymerization (exemplary case in Fig. 4.7.B). Notably, this effect is not seen in cells expressing only the C-peptide-EGFP (Fig. 4.7.A). This phogrin-induced actin phenotype can be artificially reproduced by treating C-peptide-EGFP-expressing cells with an actin-depolymerizing agent, Latrunculin-B (example in Fig. 4.7.C). These results are consistent with the *i*MSD analysis on C-peptide-EGFP expressing cells treated with Lat-B, which shows a ~ 3 -fold increase in granule local diffusivity, a concomitant ~ 1.5 -fold decrease of the α coefficient, and as

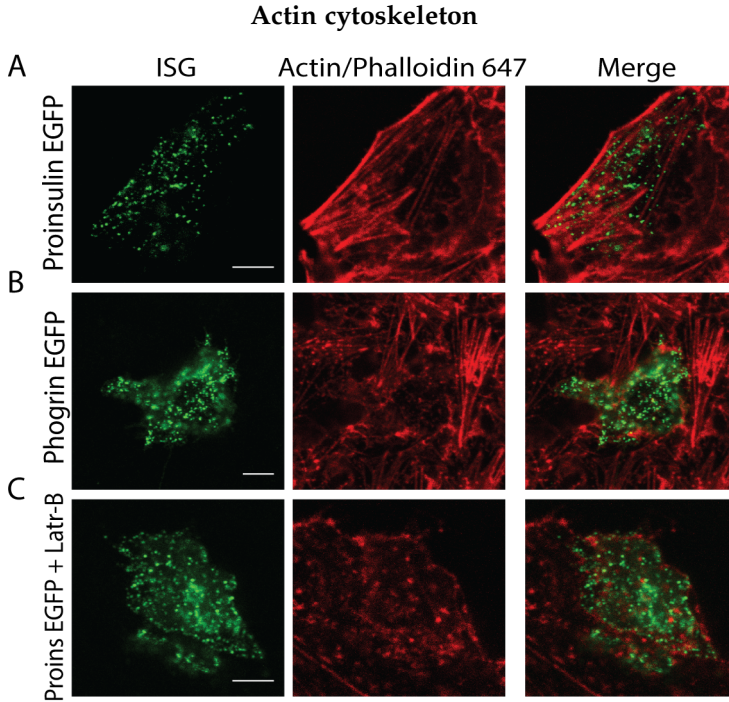


FIGURE 4.7: **A)** Representative case: C-peptide-EGFP transfected ISGs (green), actin labeled with Phalloidin-647 (red) and overlay of the two channels. **B)** phogrin-EGFP transfected ISGs (green), actin labeled with Phalloidin-647 (red) and overlay of the two channels. **C)** C-peptide-EGFP transfected ISGs (green) and treated with $10 \mu\text{M}$ Latrunculin-B before fixation, actin labeled with Phalloidin-647 (red) and overlay of the two channels. Scale bar = $5 \mu\text{m}$.

expected for C-peptide-EGFP, no effect on granule size (Fig. 4.8 and Table 4.2).

As a final test, insulin secretion from stably-phogrin-expressing cells was evaluated and compared to that of unlabeled cells. In case of low-glucose concentrations (2.8 mM), insulin release appears to be not affected by phogrin-FP expression (Fig. 4.9). In contrast, high-glucose concentrations (16.7 mM) showed a 30% reduction in normalized insulin secretion from phogrin-FP expressing cells as compared to unlabeled cells.

At this point, a few considerations on the data collected so far in needed. Similar *i*MSD-derived fingerprints were found for all luminal granule mark-

Fingerprint of Latrunculin-B treated ISGs

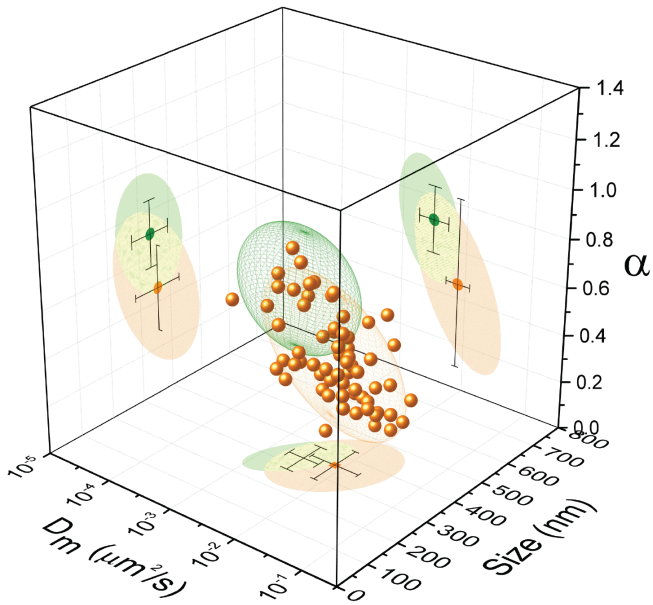


FIGURE 4.8: Dynamic fingerprint of Latrunculin-B treated C-peptide-EGFP ISGs compared to C-peptide-EGFP ISGs dynamic fingerprint (represented as a 68% confidential ellipsoid in green).

Labelling	Size (nm)	$\frac{D_m}{(\mu m^2 \setminus s)} \times 10^{-3}$	α	N	SCD
Phogrin	420 ± 88	13 ± 6	0.5 ± 0.2	94	0.858
C-pep+Latr-B	356 ± 72	10 ± 9	0.5 ± 0.2	65	0.489

Summary of *i*MSD-derived parameters treated cells

TABLE 4.2: Summary of *i*MSD-derived parameters for phogrin-EGFP labelled ISGs and Latrunculin-B treated C-peptide-EGFP labelled ISGs

ers, but a clear fingerprint shift for the membrane marker the phogrin-FP was observed. The size effect is consistent with steric hindrance due to protein over-expression (and accumulation) on the granule membrane. However, the change in mobility appears to be linked to phogrin-dependent depolymerization of the membrane actin meshwork, based on data reported above. Worthy of mention, it was recently proposed that phogrin is able to reduce plasma membrane phosphatidylinositol 4,5-bisphosphate (PI(4,5)P₂) abundance, which, in turn, induces actin depolymerization. The structural and dynamic parameters measured in phogrin-FP labelled cells are consistent with the secretion data which show that phogrin overexpression induces a substantial decrease ($\sim 30\%$) of insulin secretion under high glucose stimulation. Still, it is not clear how to reconcile existing contradictory literature in which different cell lines and experimental conditions have been tested, and phogrin overexpression was alternatively associated with suppression of glucose-stimulated insulin secretion, its stimulation, or even with no substantial effect [134]. The decreased insulin secretion from stably transfected cells reported here suggests that the impact of phogrin overexpression is limited to the impairment of cell responsiveness at high glucose concentrations. By contrast, a phogrin-dependent effect at low protein concentrations is not observed and that may also explain some of the contrasting results reported in the literature. Reported data suggest that it will be useful to re-interpret and evaluate many previously published results. The expectation is that the information obtained by the *i*MSD analysis can be further increased by combining such output with the use of "intelligent" dyes/proteins to simultaneously probe specific parameters on the structure of interest (e.g. pH, membrane order, etc.). Such implementation could transform the basic strategy presented here in a flexible, multiplexed platform to quantitatively address the complex regulation of insulin granule trafficking.

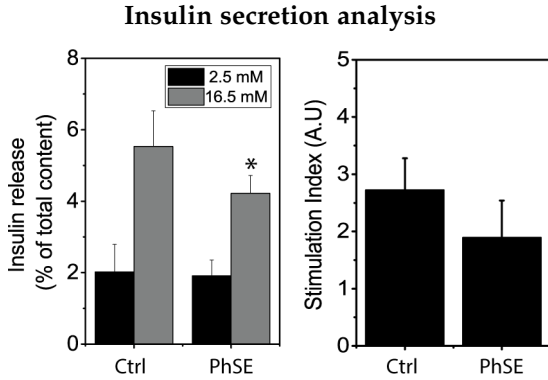


FIGURE 4.9: Insulin release (expressed as % of total insulin content) from non-transfected INS-1E cells (Ctrl) and stably expressing phogrin-EGFP INS-1E cells (Phogrin stable) exposed to low glucose concentration (2.8 mM, grey bar) and high glucose concentration (16.7 mM, black bar). * $p < 0.05$ for Kolmogorov-Smirnov test ($n=6$). Stimulation index (i.e. ratio between insulin release in high and low glucose condition) for non-transfected INS-1E (Ctrl) and stably expressing phogrin-EGFP (Phogrin stable) INS-1E.

4.4 WHICH FUTURE FOR LABEL-FREE IMAGING OF ISGS IN LIVING MATTER?

Although the use of fluorescent proteins to study ISGs dynamic remains - as a matter of fact - essential, it cannot be excluded that label-free imaging approaches could come into play and definitely tackle the need for protein over-expression. In this regard, light scattering was recently proposed as an intrinsic indicator for pancreatic islet mass and secretion performances [135]. The ISG, in particular, was proposed to be a reasonable candidate as the main intracellular source of scattered light due to the densely-packed insulin semi-crystal in the granule lumen. This scenario, if confirmed, would pave the way to new exciting possibilities for single-granule imaging, tracking, and analysis in live cells and tissues, with no need to over-express fluorescently-tagged granule proteins.

This scenario motivated my research group to investigate the intrinsic optical properties of single ISGs in single live cells by means of a combination of multi-channel imaging of scattering and fluorescence (from selectively labelled ISGs), co-localization assays, spatiotemporal cross-correlation analysis, and comparison between β -like (INS-1E) and non β -like (CHO) cell

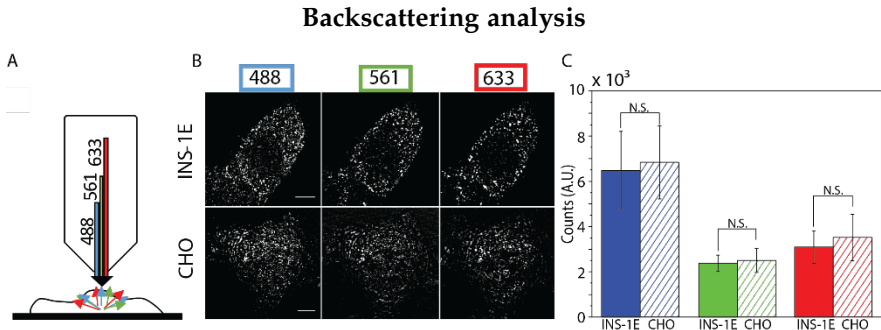


FIGURE 4.10: **A)** schematic representation of backscattering signal acquisition. **B)** Backscattering signal of INS-1E cell and CHO-K1 cells measured at three different wavelengths: 488 nm, 561 nm and 633 nm. Scale bar: 5 μm . **C)** Comparison of average backscattering signal at the three selected wavelengths of CHO-K1 ($n=10$ cells) and INS-1E ($n=12$ cells). No statistically significant differences (N.S.) according to Kolmogorov-Smirnov test (significance level: 0.001) are present.

lines. In particular, the backscattering signal at various laser illumination wavelengths was recorded (as schematized in Fig. 4.10.A), that is: a unique detection signal peaking at the incident light wavelength. As can be clearly discerned from Fig. 4.10.B, at any incident wavelength, INS-1E cells show scattering signal as a punctuate pattern, mostly excluded from the cell nuclei, in keeping with previously reported results [135]. Quite surprisingly, CHO-K1 cells show a similar overall level of scattering as compared to INS-1E and an analogous punctuate pattern of scattering signal at the intracellular level (Fig. 4.10.B-C).

4.4.1 Comparison between the light scattering properties of ISGs and lysosomes.

To assess the identity of the scattering sources within tested cells, we performed experiments in presence of fluorescent markers of specific intracellular structures. As shown in Fig. 4.11.A, we first labelled ISGs in INS-1E cells by transient transfection of the phogrin-mCherry protein. Despite the well-characterized negative impact that a phogrin overexpression exerts on ISGs features, in this case phogrin was chosen for its transmembrane localization that does not perturb the insulin intra-granular dense-core crystal, i.e. the putative source of scattered light. In a single-wavelength (i.e. 561 nm), dual channel experiment we combined the simultaneous detection

of scattering and fluorescence signals from ISGs. As control, a similar experiment was performed on fluorescently-labelled lysosomes, a well-known intracellular source of scattered light [136]. Worthy of note, already from visual inspection of the two channels (and their superimposition), it is quite clear that punctuate scattering signal from INS-1E cytoplasm does not convincingly correspond to labelled granules. By contrast, in keeping with expectations, lysosomes appear as quite highly-refractive intracellular organelles.

A standard co-localization analysis of the scattering and fluorescence signals (e.g. by calculation of Manders' coefficients) would quantitatively support, in principle, visual inspection. Still, it would be prone to artifacts due to the presence of a background of "speckle"-like scattering from the cell [137]. To tackle this issue, we performed spatiotemporal cross-correlation analysis on time-lapse imaging of scattering and fluorescence signals. In particular, by using cross-STICS (Spatio-Temporal Image Correlation Spectroscopy) [113, 138], we can highlight the possible dynamic co-localization of signals, i.e. the presence of intracellular dynamic structures which retain both the scattering and fluorescence signals while moving (a feature that does not apply to speckle-like signal). On this basis, we probed fluorescent ISGs and, as a reference, stained lysosomes (Fig. 4.11.A). As better described in the Appendix A (Methods section), the amount of cross-correlation measured was used to classify cells as "positive" or "negative", in terms of the dynamic co-localization of signals (Fig. 4.11.B). As reported in the histograms in Fig. 4.11.C, only a relatively low amount of measurement on ISGs (about 30%) showed positive cross-correlation with scattering signals. By contrast, almost 70% of the measurements showed positive dynamic co-localization of labelled lysosomes with scattered signals. In general, these results point out that scattering from ISGs, if present, does not afford a dominant contribution to the total cellular refractive properties.

4.5 CONCLUDING REMARKS.

In this Chapter, the structural and dynamic features of whole cell populations of trafficking granules are measured under different labelling condition (i.e. protein overexpression) by means of high-throughput screening provided by the *i*MSD method. All luminal FP-markers have similar *i*MSD-derived clusters (size, D_m , α), but a clear shift in the shape and position of the phogrin-FP cluster has emerged. Phogrin-FP induces a

Cross-correlation analysis

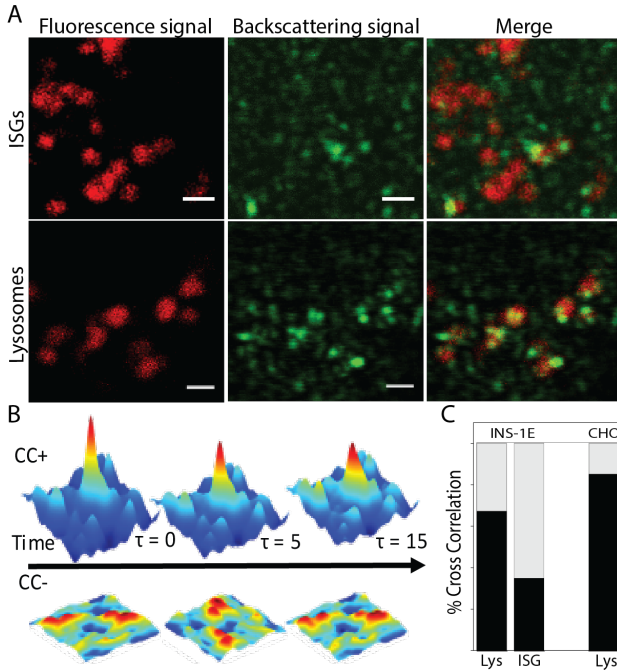


FIGURE 4.11: **A**) Static co-localization between fluorescence signals of ISGs labelled with phogrin-mCherry (top row) and lysosomes labelled with LysoTracker RedDND-99 (lower row) or with the respective backscattering signal (BS) at 561 nm in INS-1E cells. Scale bar: $1 \mu\text{m}$. **B**) Spatiotemporal cross correlation functions for three different time delays ($t=0\text{s}$, $t=5\text{s}$, $t=15\text{s}$) showing an exemplary experimental case of positive dynamic colocalization (or cross-correlation, CC+) and negligible dynamic colocalization (or cross-correlation, CC-) between fluorescence signal of labelled organelles and backscattering signal (see Methods for further details). **C**) Percentage of positive (black bar) and negative (grey bar) dynamic colocalization acquisitions of fluorescent labelled lysosome ($n=67$) and ISGs ($n=65$) in INS-1E cells and labelled lysosome ($n=85$) in CHO cells with backscattering signal.

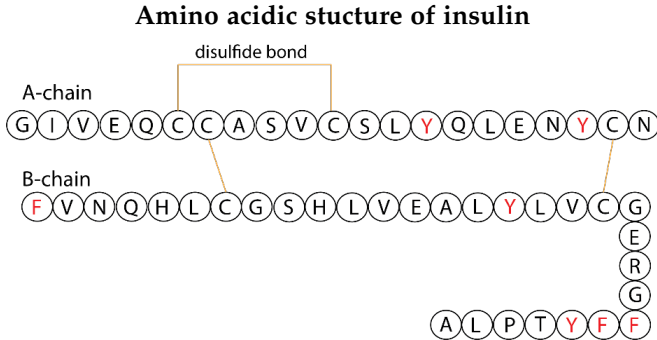


FIGURE 4.12: Amino acidic primary structure of human insulin molecule. The fluorescent amino acids are highlighted in red.

concentration-dependent increase in both granule size and mobility. The size effect is consistent with steric hindrance due to protein overexpression on the membrane. However, the change in mobility appears to be linked to phogrin-dependent depolymerization of the membrane actin meshwork. It has been proposed that phogrin functions to reduce plasma membrane phosphatidylinositol 4,5-bisphosphate (PI(4,5)P₂) abundance, which, in turn, induces actin depolymerization [123, 139]. Moreover, phogrin overexpression induces a substantial decrease (~30%) of insulin secretion under high glucose stimulation.

In addition, we demonstrated that ISGs are not a primary source of scattering in immortalized β -like cells, at least not quantitatively superior to several other intracellular organelles/structures, such as lysosomes and internal membranes. Collectively, these results do not question the conclusions of previous reports and, in particular, the proposed idea to use the light scattered from 3D Langerhans islets as versatile and noninvasive characterization of islet morphology and plasticity as well as hormone secretory status. Still, what observed here suggests caution in the identification of an exclusive sub-cellular source of scattering within β - and β -like cells and, consequently, a careful re-thinking of the possibility to use scattering for label-free specific imaging of insulin secretory granules. Still, the label-free approach for studies on granule properties in living cells does probably not end here.

In fact, in the aminoacidic primary structure of the human insulin molecule (Fig 4.12), there are 4 tyrosine (Y, 5 in the rat sequence) and

Amino acid	Excitation (nm)	Emission (nm)	Quantum yield
Tryptophan	280	350	0.2
Phenylalanine	260	280	0.04
Tyrosine	275	300	0.14

Optical properties of the principal fluorescent amino acids

TABLE 4.3: Optical properties of the principal fluorescent amino acids present in protein

3 phenylalanine (F) [140]. These amino-acids, together with tryptophan, are able to emit fluorescence in the range 280-380 nm when excited in the UV (~ 270 nm, Table 4.3) [141]. The optical properties of these amino acids can be affected by a number of environmental factors, such as temperature, pH, ionic strength, non-covalent interaction and, in general, are characterized by a low quantum yield (Table 4.3). Still, it is worth noting that each ISG hosts ~ 200.000 insulin molecule packed in semi-crystallin hexamers, for an estimated final concentration around 40 mM (inside each granule) [38].

This high concentration could, in principle, allow to overcome the aforementioned imaging limitations and be exploited for label-free multiphoton imaging of granules, similarly to what demonstrated years ago for another hormone, serotonin [142].

TOWARDS MULTIPLEXED BIOPHYSICAL ANALYSES IN THE LIVING ISLET

Some of the results presented here are part of a paper in preparation:

- Effects of GLP-1R agonists on cell survival, function and granule motility.

Ferri G., Bugliani M., Marchetti P., Cardarelli F.

"In the past we have mostly been using cells from rodents, which we have discovered are quite different to human β -cells. We are different from mice and as my clinical friends often remind me, **rodent diabetes is not a major clinical problem!** So if we want to understand human diabetes we should work on human β -cells and that is the only way of moving forward"

said Patrik Rorsman, Professor of Diabetic Medicine at the Oxford Centre for Diabetes, Endocrinology and Metabolism (OCDEM). These words point out one of the major critical issues in Diabetes research. In fact, in the field of β -cell physiopathology, considerable results have been achieved using clonal β -cell lines derived from rodent insulinomas (such as INS-1E): these cell lines have proven to be a great asset in Diabetes research but the selection of the most appropriate rodent β -cell line is often challenging, and no single cell line entirely recapitulates the properties of a human β -cell. However, access to human Langerhans Islets is not trivial from both an ethical and technical point of view. To tackle this challenging roadblock, I exploited the precious collaboration with Prof. Piero Marchetti and his research group at the Department of Clinical and Experimental Medicine (Islet Cell Laboratory) of University of Pisa and Cisanello Hospital. They provided cells and tissues, together with the fundamental expertise in the field of β -cell and Langerhans Islets physiopathology. In this final Chapter initial steps towards the application of a "broad range" biophysical analysis on human Islet (HI) will be described. Following the two main pillar

this thesis, i.e. glucose-activated metabolism and granule's movements, Phasor-FLIM on NAD(P)H signal and *i*MSD analysis have been applied to HIs with preliminary results, mostly oriented to gain knowledge and to characterize such a complex sample.

5.1 PHASOR-FLIM ANALYSIS ON HIS.

Thanks to a collaboration established with the Islet Cell Laboratory guided by Prof. Marchetti at Cisanello Hospital (Pisa), I could perform experiments on HI harvested from pancreas of brain-dead organ donors. Our collaborators isolated human islets from the pancreas of non-diabetic organ donors by collagenase digestion and density gradient purification then cultivated in M199 medium [143]. With a 2-photon excitation beam tuned to 710 nm and the emission signal collected in the 400-500 nm range (NAD(P)H emission), the fluorescence signal coming from HI is measured and reported in Fig. 5.1.A. It derives mainly from cytoplasmic regions, which appear with a uniform staining. Cell nuclei can be easily distinguished as ellipsoidal regions with a sensibly lower fluorescence signal. Overall, the presence of brighter spots scattered throughout the sample is observed. Parallel to previously reported experiments (Chapter 2) on INS-1E cells, a step towards an application of Phasor-FLIM approach to the study of metabolic fingerprint of HI was done. Phasor analysis on the mixture of lifetimes measured on the sample has reported in Fig. 5.1.B (a zoomed area of HI of Fig. 5.1.A) colored according to NAD(P)H free and bound lifetimes.

5.1.1 *Characterization of autofluorescence signal and lifetime in isolated human pancreatic islets.*

Due to the extreme complexity of this kind of tissue/micro-organs, a preliminary characterization of autofluorescence signals and relative lifetimes is essential to build a framework of knowledge to interpret different metabolic states. For example, the formation of cross-linked protein aggregates such as lipofuscin is an accepted hallmark of cellular aging and is inversely related to longevity. Lipofuscin is an intralysosomal aggregate, composed mainly of cross-linked proteins and formed due to oxidative processes [144–146]. It is expected to find such aggregates in human sample, especially from aged donors, as lipofuscin is degradable and cannot be

Phasor FLIM analysis on HIs

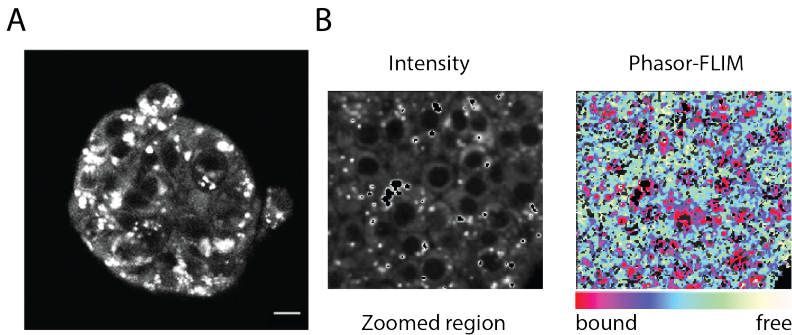


FIGURE 5.1: **A)** Two-photon intensity image of autofluorescence signal arising from an intact human Langerhans islet. Scale bar: 10 μm . **B)** Zoomed area of (A) and Phasor-FLIM analysis colored according scale bar below.

removed via exocytosis. Lipofuscin accumulation is specific of post-mitotic and senescent cells, such as neurons [147] and skeletal muscle cells [153], whereas proliferative cells dilute it during division. Adult pancreatic α - and β -cells are also considered to be long-living cells with a very low proliferation rate.

In Fig. 5.2 it is possible to note the partial overlap between emission spectra of NAD(P)H and lipofuscin. Despite this complex autofluorescence pattern, (Fig. 5.3) it is possible to isolate lipofuscin contribution from the whole signal by Phasor-FLIM analysis [71]. In Fig. 5.3.A a zoomed area is reported of a HI. According to emission spectra of Fig. 5.2 in the 400-500 nm interval the collected signal is a convolution of NAD(P)H and lipofuscin signals. The corresponding phasor plot (Fig. 5.3.B) shows that most of the pixels in the image contain complex lifetimes (located within the universal circle) close to the typical position of bound NAD(P)H. Exploiting the phasor properties (see Chapter 2), it is possible to highlight NAD(P)H signal by selecting its specific position in the plot: as shown in Fig. 5.3.C with the red cursor, this corresponds to cytoplasmic areas and nuclei, as expected. Similarly, with the green cursor an elongated feature of the phasor is highlighted, which correspond (Fig. 5.3.C) to the brightest regions of the intensity image of Fig. 5.3.A. If it is impossible to separate intensity emission of NAD(P)H and lipofuscin in the emission interval of 400-500 nm, it is possible to isolate only lipofuscin contribution to autofluorescence

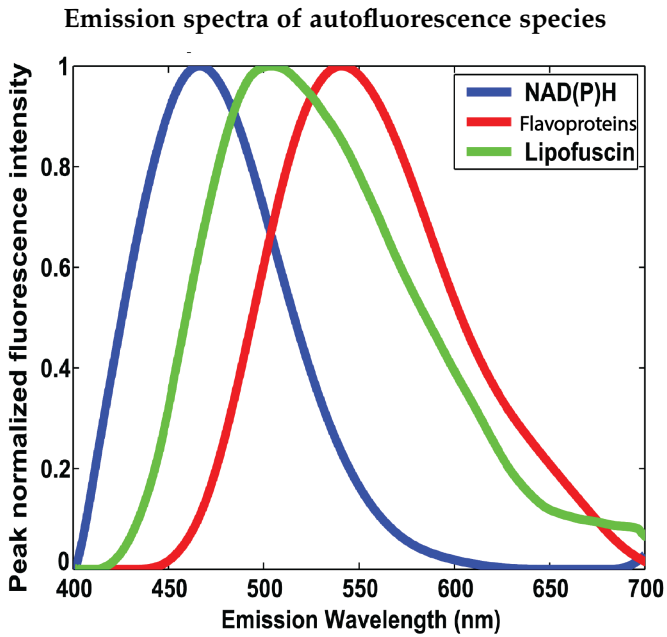


FIGURE 5.2: Emission spectra of three intracellular species contributing to total autofluorescence signal

signal from NAD(P)H, changing the collected emission interval to 600-650 nm. In fact, in this emission interval, only the signal from lipofuscin is present (Fig. 5.3.D) and corresponds to bright spots also present in Fig. 5.3.A. Red and green cursors are used again to isolate lifetimes in phasor plot (Fig. 5.3.E). This time, most of the pixels of the image show lifetimes limited in the green cursor, which can be definitively attributed to lipofuscin (Fig. 5.3.F).

The ultimate goal remains applying the phasor-FLIM approach to describe the metabolic shifts that a whole, intact, HI experiences during glucose stimulation, as previously done for INS-1E cells. Along this path, it should be kept in mind that, contrary to isolated cells, an intact islet is essentially an "organ inside an organ (the pancreas)", composed by different cell types, among which β -cells represent the majority but not the totality. If successful at this stage, this would represent a remarkable step forward in the comprehension of the physiology of the GSIS process in its native context and, most importantly, of its alteration in Diabetes.

5.2 STRUCTURAL-DYNAMIC FINGERPRINT OF ISGS IN DISPERSED HI CELLS.

As already discussed, the dynamic behavior of granules represents the other key process of the β -cells investigated in this thesis. For this purpose, the same approach applied to INS-1E cells was applied here to HIs upon transfection of a fluorescent chimeric protein to label ISGs. Unfortunately, the use of conventional transfection methods (i.e. lipofection) does not guarantee the same high efficiency observed in isolated cells. To overcome this issue, HIs were first treated with digestion enzymes to disperse the cells, then cells were let adhere on standard glass-made supports. Finally, disaggregated and adherent cells were transfected with syncollin-EGFP by standard procedures (Fig. 5.4.A). Transfected cells were also fixed and immunostained against insulin to distinguish β -cells from non- β -cells (Fig. 5.4.B, picture). This control experiment assures that nearly 75% of syncollin-EGFP expressing cells are true β -cells, as they are positive for insulin antibodies (Fig. 5.4, plot). It should be noted that syncollin-EGFP overexpression, based on previous results on INS-1E cells described in Chapter 4, does not significantly alter ISG structural and dynamic properties.

By means of *i*MSD analysis, the granules' average diffusion law and parameters describing granules motility (i.e. the local and the anomalous

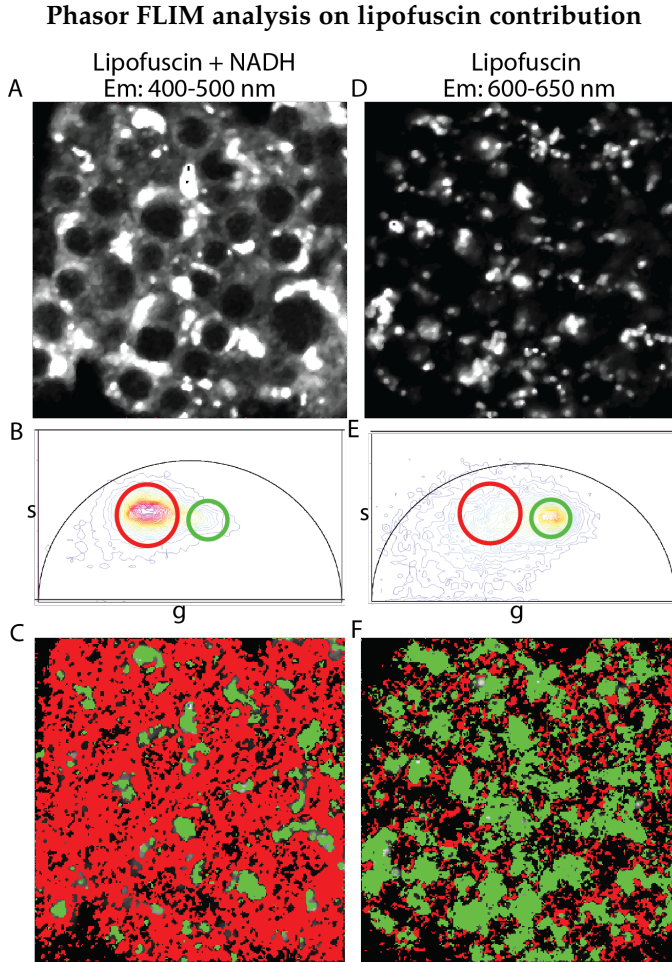


FIGURE 5.3: **A)** Two-photon fluorescence intensity imaging of intact HI obtained exciting the sample at 700 nm and collecting the emitted signal at 400-500 nm. **B)** FLIM phasor plot of cell autofluorescence. **C)** FLIM maps obtained applying for each pixel the color defined in circles in (B). **D)** Two-photon fluorescence intensity imaging of intact HI obtained exciting the sample at 700 nm and collecting the emitted signal at 600-6500 nm. **E)** FLIM phasor plot of cell autofluorescence. **F)** FLIM maps obtained applying for each pixel the color defined in circles in (E).

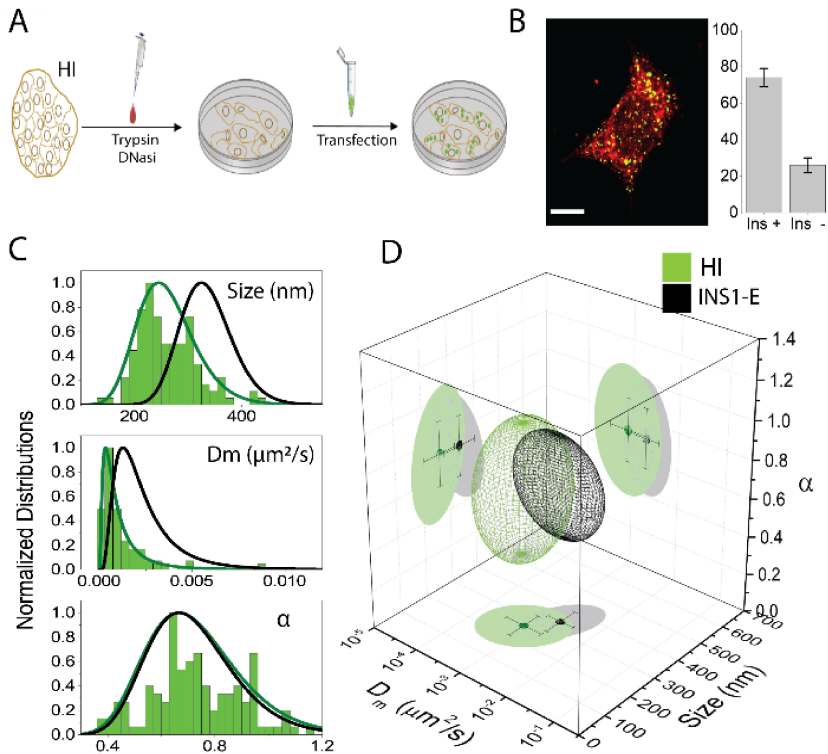
iMSD-based screening of ISGs in dispersed human β -cells

FIGURE 5.4: **A)** Schematic representation of human Langerhans islets disaggregation and transfection. **B)** Exemplary image of immunostaining with Alexa 541 Anti-insulin Ab (red) on disaggregated cells transfected with syncollin-EGFP (green). Scale bar: 5 μm . Plot showing the percentage of Insulin-Ab positive ($\sim 75\%$) and negative transfected cells ($\sim 25\%$) in $N=3$ samples. **C)** Normalized distributions of the three relevant parameters (Size, D_m and α) of $n=48$ acquisitions of INS1-E ISGs (black curve and bars) and $n=120$ of syncollin-EGFP ISGs in dispersed human islets (green curve and bars). **D)** 3D parametric plot showing the fingerprint of dispersed HI syncollin-EGFP transfected granules (green) in comparison with fingerprint of INS-1 E syncollin-EGFP transfected ISGs (represented as 68% confidential ellipsoid in black). Here, for instance, cluster similarity analysis yields a value of statistical cluster distance (SCD) of 0.536, indicating a partial superimposition of the two clusters (SCD=0 total superimposition, SCD=1 absence of superimposition)

Cell	Size (nm)	D_m ($\mu\text{m}^2 \setminus \text{s}$) $\times 10^{-3}$	α	N	SCD
INS-1E	340 \pm 60	2.4 \pm 1.8	0.71 \pm 0.16	48	/
HI	263 \pm 58	1.2 \pm 1.4	0.71 \pm 0.17	124	0.54

Summary of *i*MSD-derived parameters for HIs cells

TABLE 5.1: Summary of *i*MSD-derived parameters for HIs dispersed cells

(α) diffusion coefficients) were extracted. This approach allows to measure the structural and dynamic properties of granules on primary human β -cells (Table 5.1). Moreover, it permits the comparison between structural and dynamic properties of primary human insulin granules and granules from INS-1E (Fig. 5.4 and Table 5.1). Despite the undeniable usefulness of immortalized models, in fact, it is important to understand how much they are affordable/predictive models of their primary (possibly human) counterparts. Here, for instance, the *i*MSD analysis reveals that the granule fingerprint in human-derived β -cells is substantially different from that of immortalized INS-1E cells (Fig. 5.4.C-D). In particular, the average characteristic size of ISGs is nearly 30% smaller in primary human -cells as compared to INS-1E cells (see Table 5.1), in accordance with previous TEM-based results [60, 148]. At the same time, ISGs from primary human β -cells show a 2-fold lower local diffusivity ($1.2 \times 10^{-3} \mu\text{m}^2/\text{s}$) as compared to their immortalized counterparts ($2.4 \times 10^{-3} \mu\text{m}^2/\text{s}$), although the mean values of anomalous coefficients α are nearly identical (~ 0.7).

The need to precisely identify the β -cell among the cell types populating the HI remains, however, a fundamental requisite for the next future. In this regard, lentiviral transduction would be the election method to achieve transgene expression in the HI by means, for example, of third-generation self-inactivating lentiviral vectors containing proinsulin-(C-peptide)-EGFP under the control of a human insulin promoter (HIP) [149]. The possibility to label specifically the β -cells with this system would in turn allow several cell-specific biophysical analyses in the living islet and more reliable conclusions on β -cell functionality.

5.3 CONCLUDING REMARKS.

In spite of the crucial role played by β -cells in systemic glucose homeostasis, a detailed comprehension of the mechanisms regulating their metabolic

response to blood glucose is far from being reached. The matter becomes even more delicate if we consider the high socio-health impact that pathologies related to the β -cell – Type 1 and Type 2 Diabetes above all – have worldwide. Therefore, it is clear that quantitative and non-invasive methods to study the key process of the pathophysiology of the β -cell are highly desirable. In this Thesis I described the implementation of selected state-of-the-art biophysical approaches to address two main pillars of β -cell function, i.e. its peculiar metabolic response to glucose and the subsequent mobilization of the vast population of insulin-containing granules towards secretion. In the first experimental Chapter, the Phasor-FLIM approach was used to address the first pillar: the intrinsic signal of NAD(P)H was exploited to demonstrate how β -cells respond to glucose stimulation (differently from cell lines not specifically committed to secretion), switching their metabolic state from a "glycolytic"-like one towards an "oxidative"-like one to trigger insulin release. The same approach was used to monitor the effect of glucotoxicity on the β -cell response and the consequent production of ROS and ROS-induced damages. These results lay the ground for rapid and label-free investigations on the progression from the physiologic to the pathologic condition which is typical of Diabetes. The second pillar identified in my Thesis, i.e. the ISGs trafficking within the cell cytoplasm, was addressed by spatiotemporal fluctuation spectroscopy. A straightforward fluctuation-based algorithm, named *iMSD*, was adapted and used to extract granule structural and dynamic properties from simple time-lapse imaging of fluorescently-labelled ISGs. First, *iMSD* applicability to the granule-case was tested, a standard imaging protocol set and a reference created using C-peptide-EGFP under basal culture condition. Then, the same approach was used to rapidly and quantitatively screen the effect of labelling by the most widely used granule-specific protein markers (tagged to FPs) on granule structure and dynamics. Strikingly, profound structural and dynamic alterations of granules induced by expression of the granule transmembrane protein phogrin were found, with a concomitant impact on actin cytoskeleton integrity and overall β -cell secretion capability. This evidence calls into question the interpretation of a significant amount of previous data from living β -cells produced by using this granule protein as marker. In the last Chapter, I collected some preliminary data obtained in intact human pancreatic islets. This peculiar and precious sample will represent the most promising experimental platform to address the pathophysiology of Diabetes in the next (near) future. Phasor-FLIM analysis on the complex intrinsic fluorescence signal coming from HIs has already per-

mitted to isolate the contribution of lipofuscin (an intracellular aggregate, often associated to post-mitotic and senescent cells) from the total signal and distinguish it from NAD(P)H. The ISGs trafficking in HI was also investigated and ISGs structural-dynamic fingerprint was defined using human-derived primary β -cells disaggregated starting from whole islets. Of note, the human ISG shows neat differences in size (they are smaller) and dynamics (they are slower) as compared to ISGs from immortalized cell lines. Again, these preliminary results pave the way to the next step, i.e. complete structural/dynamic fingerprinting directly within intact living islets.

In my opinion, future investigations shall move towards obtaining a multiplexed biophysical analysis in the islet, by coupling multiphoton microscopy with both intrinsic and exogenous fluorescent probes. The goal would be to perform optical microscopy for quantitative live-tissue imaging combined with new promising strategies to selectively identify the β -cell. If successful, this will represent a paradigmatic shift in the way we describe biological processes within islets and β -cells, bearing the potential to unveil new molecular determinants of β -cell physiology and the pattern of their mis-regulation that is characteristic of the pathological state.

MATERIALS AND METHODS

A.1 CELL CULTURES.

INS-1E cells [88] were maintained in culture at 37 ° C, 5% CO₂ in RPMI 1640 medium containing 11.1 mM D-glucose, 10 mM HEPES, 2 mM L-Glutamine, 100 U/ml penicillin-streptomycin, 1 mM sodium-pyruvate, 50 μM tissue culture grade β-mercaptoethanol (all purchased from Life Technologies, Thermo Fisher). Before live-cell imaging, cells were plated onto IbiTreat β-Dish 35 mm, high walls, 1.5 polymer coverslip, tissue culture treated, sterilized and fluorescence microscopy suitable (Ibidi, Martinsried, Germany). CHO-K1 cells were provided by American Type Culture Collection (CCL-61 ATCC) and grown in Dulbecco's modified Eagle medium F-12 nutrient mix supplemented with 10% FBS, 100 U/ml penicillin, and 100 mg/ml streptomycin (TermoFisher Scientific). Before live cell imaging cells were plated onto IbiTreat μ-Dish 35 mm, high walls, 1.5 polymer coverslip, tissue culture treated, sterilized and fluorescence microscopy suitable (Ibidi, Martinsried, Germany). A549 and HEK-293 were maintained respectively in complete RPMI 1640 medium (10 % FBS, 11.1 mM D-glucose, 10 mM HEPES, 2 mM L-Glutamine, 100 U/ml penicillin-streptomycin, 1 mM sodium-pyruvate) and complete DMEM high glucose medium (10 % FBS, 22 mM D-glucose, 10 mM HEPES, 2 mM L-Glutamine, 100 U/ml penicillin-streptomycin, 1 mM sodium-pyruvate).

A.2 TRANSFECTIONS AND PLASMIDS.

All cells were transfected using lipofectamine 2000 reagent as per manufacturer's instructions and using Optimem culture medium (Life Technologies, Thermo Fisher). Phogrin-mCherry plasmids were a kind gift from Zeno Lavagnino (Piston Lab, Cell Biology & Physiology, Washington University in St. Louis). Phogrin-EGFP plasmid was obtained subcloning EGFP coding sequence from EGFP-N₃ plasmid (Clonotech) by PCR and introducing AgeI (ACCGGT) and BsrGI (TGTACA) restriction enzyme sites at 5' and 3' ends, respectively. (Forward primer: 5'-gactggACCGGTcgccaccatggtgagcaaggcgagg-

3′; Reverse primer: 5′-cctgggTGTAAGctcgtccatgccgagag-3′). These sites were used to clone the fragment in phogrin-mCherry plasmid by double-digestion with the same enzymes to remove mCherry sequence and subsequent ligation. Syncollin-EGFP plasmid was a kind gift of Michael Edwardson (Department of Pharmacology, University of Cambridge). IAPP-EGFP plasmid was a kind gift of Erik Renström (Department of Clinical Sciences, Lunds University). EGFP-Phogrin plasmid was cloned starting from Phogrin cDNA sequence, EGFP was inserted three amino acid before the KK cleavage site by PCR. To generate a stably phogrin-EGFP expression line of INS-1E, cells were transfected with Lipofectamine 2000, with phogrin-EGFP plasmid, carrying NeoR gene which confers resistance to Geneticin (G₄₁₈). 48 h after transfection, the medium was replaced with fresh complete medium supplemented with G₄₁₈ at 50 μg/mL and a 15 days selection allowed obtaining a stable polyclonal cell population expressing phogrin-EGFP localized in ISGs. After selection, G₄₁₈ concentration was reduced at 10 μg/mL as maintenance for 1 week. The day before experiment, 5×10^5 stably transfected cells were seeded onto IbiTreat μ-Dish in complete medium devoid of G₄₁₈.

A.3 HUMAN PANCREATIC ISLETS CELLS.

Human pancreata were harvested from brain-dead organ donors after informed written consent was obtained from family members and processed for islet isolation (if not suitable for clinical whole-organ purposes). In more detail, human islets were isolated from the pancreas of non-diabetic organ donors by collagenase digestion and density gradient purification. Then they were cultured for two days in M199 medium supplemented with 10% bovine serum and antibiotics at 37°C in 5% CO₂. Afterwards, the islets were incubated with Accutase (Sigma-Aldrich S.r.l, Milan, Italy) at 37°C until complete dissociation. The dispersed islet cells were plated on sterile 35 mm, high walls, 1.5 polymer coverslips (Ibidi, Martinsried, Germany), suitable for fluorescence microscopy, previously treated with components of the extracellular matrix (ECM) from Engelbreth-Holm-Swarm mouse sarcoma (Sigma-Aldrich S.r.l.). All methods described here were performed in accordance with the relevant guidelines and regulations approved by the Ethics Committee of the University of Pisa (Pisa, Italy).

A.4 CELLULAR STAINING.

For actin staining experiments, cells were fixed with 4% paraformaldehyde (PFA) 24 hours after transfection and stained for actin cytoskeleton with Phalloidin-647 (Life Technologies, Thermo Fisher) following standard protocol. In case of Latrunculin-B treatment, cells were incubated with 10 μ M Latrunculin-B for 40 minutes prior to fixation. Immunostaining on dispersed HI cells was performed with a guinea pig polyclonal antibody against insulin (ab7842 from Abcam, Cambridge, UK) and revealed with an Alexa Fluor 594-conjugated donkey anti-guinea pig antibody (Jackson ImmunoResearch Laboratories, Inc, West Grove, PA, USA).

A.5 DRUGS TREATMENTS.

For cholesterol overloading, cells were incubated with 5 mM cholesterol-M β CD complex (soluble cholesterol from Sigma; 1 g of this complex contains approximately 40 mg cholesterol) at 37°C for 1 hour. In order to disrupt the actin meshwork at the plasma membrane, transfected cells were treated with 10 μ M Latrunculin-B (Sigma-Aldrich) for 15 minutes before live cell imaging.

A.6 INSULIN SECRETION ASSAY.

Insulin release was evaluated as previously described in Ref [92]. In brief, INS-1E cells were pre-incubated in Krebs' solution containing 2.5 mM glucose for 30 minutes, then cells were exposed to the same medium at 2.5 or 16.7 mM glucose for 45 min. At the end, the supernatant was collected and stored at -20 °C until insulin measurement. Insulin levels were quantified by the High Range Rat Insulin ELISA kit following the manufacturer's protocol (Mercodia AB, Uppsala, Sweden) Data are represented as ng of released insulin normalized by the amount of cells.

A.7 FLUORESCENCE CONFOCAL MICROSCOPY.

Fluorescence microscopy experiments on INS-1E transfected cells, bathed in 11 mM glucose RPMI-1640 complete medium, were carried out with a Leica SP5 inverted confocal microscope. Images were acquired illuminating the sample with a 488 nm laser for EGFP excitation and 561 nm laser for

mCherry excitation, using a 40x (N.A. 1.27) oil-immersion objective. EGFP fluorescence was collected between 500 and 600 nm, while mCherry fluorescence was collected between 570 and 670 nm. Each acquisition consists in a collection of 500 frames 256x256 pixel at a sampling frequency of 1400 Hz/lines ($\sim 3 \mu\text{s}$ pixel) and with a pixel size of 50 nm. Pinhole aperture was set to 1 Airy. Photobleaching experiments were carried out before the acquisition of individual plates to determine the optimal excitation intensity on the sample. Imaging experiments on actin cytoskeleton stained with Phalloidin-647 were performed on Zeiss LSM 800, using a 63x/1.47 Oil objective and collecting fluorescence emission of transfected ISGs (EGFP) on 500–600 nm interval and on 650–750 nm interval for Phalloidin-647 emission. In all experiments, a low laser illumination power at the objective was used (typically 0.5–1 μW) to keep phototoxicity under control. Backscatter signal images were collected using a 40x(N.A. 1.27) oil-immersion objective, exciting the sample with different wavelengths (488 nm, 561 nm, 633 nm) laser beam and with a detection band centered at the same wavelength as the incident laser $\pm 3\text{nm}$, setting acousto optic beam splitter (AOBS) in reflection mode.

A.8 *i*MSD ANALYSIS.

Briefly, each time-lapse acquisition ($N = 500$ frames) was analyzed using a custom script working on MATLAB (MathWorks Inc., Natick, Ma) which computes by Fast Fourier methods the spatiotemporal correlation function, defined as follows:

$$g(\xi, \eta, \tau) = \frac{\langle i(x, y, t) i(x + \xi, y + \eta, t + \tau) \rangle}{\langle i(x, y, y) \rangle^2} - 1 \quad (\text{A.1})$$

$g(\xi, \eta, \tau)$ can be fitted with a standard Gaussian function of the form:

$$g(\xi, \eta, \tau) = g_0 + g_1(\tau) \exp \left\{ - \frac{(\xi - v_\xi \tau)^2 + (\eta - v_\eta \tau)^2}{\sigma^2(\tau)} \right\} \quad (\text{A.2})$$

whose variance $\sigma^2(\tau)$ is analogous to the mean square displacement extracted directly from imaging, *i*MSD. Each *i*MSD curve was fitted with the following equations to define the diffusion law and to extract the diffusion parameters α , D_m , and σ^2 . Please note, that in all the experiments on labelled granules the peak of the spatiotemporal correlation function remains

centered at $(0, 0)$ while increasing in width. This reflects the diffusive behavior of granules, while excluding net collective movements, such as those eventually produced by whole-sample drifts:

$$\sigma_r^2(\tau) = \kappa\tau^\alpha + \sigma_0^2 \quad (\text{A.3})$$

$$\sigma_r^2(\tau) = L^{2/3} \left(1 - \exp\left(-\frac{\tau}{\tau_c}\right) \right) + 4D_M\tau + \sigma_0^2 \quad (\text{A.4})$$

With eq.(A.3)) the ISG's motion is categorized according to the value of α in ($\alpha=1$) isotropic diffusion, ($\alpha < 1$) anomalous diffusion, ($\alpha > 1$) guided diffusion. In case of (partially) confined diffusion eq.(A.4) is used to fit $\sigma^2(\tau)$ trend, where L defines the linear size of the confinement area, τ_c is an index of how fast confinement occurs, D_M is the diffusivity at large time scale and represents $1/4$ of the derivative of σ_2 for $\tau \rightarrow \infty$. D_m is calculated by the slope of σ^2 for $\tau \rightarrow 0$, it represents the diffusivity inside the confinement area and is defined by the following relation:

$$D_m = D_M + \frac{L^2}{12\tau_c} \quad (\text{A.5})$$

In both eq.s (A.3) and (A.4), σ_0^2 is the intercept value which is related to the average particle size, (as discussed in [64] and in Appendix??). In particular, the apparent particle size could be calculated using:

$$Size_{app} = \sqrt{\sigma_0^2} \quad (\text{A.6})$$

In this case, $Size_{app}$ (apparent) represents the average diameter of imaged ISGs, i.e. the real size of the ISGs convolved with instrument's PSF. For the derivation of the actual size, refer to equations presented in Appendix B. The PSF at 488 nm was calibrated using 30-nm fluorescent beads and resulted to be 270 nm.

A.9 CLUSTER SIMILARITY ANALYSIS.

The measured parameters (i.e. the short-scale diffusion coefficient D , the i MSD intercept value σ_0^2 and the anomalous coefficient α of each image-stack define a data point in a 3-dimensional space. Thus, the set of data points corresponding to the dynamics of a specific system is a 3D multivariate

distribution of the measured values. To quantify a degree of similarity among the investigated dynamics, we calculated the statistical difference d between two distributions, as follows:

$$d = \sqrt{C (\mu_1 - \mu_2)^T \Sigma^{-1} (\mu_1 - \mu_2)} \quad (\text{A.7})$$

where C is a scale factor, μ_1 and μ_2 are three-component vectors representing the mean values of the first and second distribution, respectively. Σ is defined in terms of the corresponding covariance matrices, Σ_1 and Σ_2 :

$$\Sigma = \frac{(\Sigma_1 + \Sigma_2)}{2} \quad (\text{A.8})$$

Eq. (A.7) generalizes the Mahalanobis distance between a point and a distribution and represents a measurement of statistical distance that take into accounts extents, relative positions and orientations of the observed distributions in the parameter-space. For a single distribution, a confidence volume can be computed from the covariance matrix and is represented as an ellipsoid. The ellipsoid is therefore defined by the distribution itself; its location, size and orientation, depend on averages and standard deviations of the observed variables. The scale factor in eq.(A.7) is related to the dimensionality of the problem and can be normalized (i.e. $C = 1.1396$) to ensure that the statistical meaning of the ellipsoid represent the 3D generalization of the error bars, which are usually employed for 1D distribution. In other words, 68% of the observed data falls within the ellipsoid. In terms of statistical distance, with this normalization, two distributions with the same mean values have $d = 0$, independently of their covariance matrices. If the average values are different and the corresponding ellipsoids intersect each other, then $0 < d < 1$. If the ellipsoids are externally tangent, then $d = 1$. If the distributions are far enough that there is no intersection between the ellipsoids, then $d > 1$. Finally, an overlap coefficient between two distributions can be estimated. We employed the definition of the Szymkiewicz-Simpson coefficient CIT and calculated the overlap as follows:

$$s = \frac{\Omega_0}{\min[\Omega_1, \Omega_2]} \quad (\text{A.9})$$

where Ω_1 and Ω_2 are the volumes of the two ellipsoids and Ω_0 represents the volume of their intersection.

A.10 FLUORESCENCE-BASED EXPRESSION LEVEL ANALYSIS.

Average fluorescence intensity was calculated on the first frame of each acquired movie, by means of ImageJ plugin Analyze Particles, used to isolate ISGs fluorescence spots. The obtained value was normalized based on the laser intensity and PMT gain of each acquisition using green Autofluorescent Plastic Slides from CHROMA as a reference.

A.11 TRAJECTORY ANALYSIS.

Trajectories analysis was performed using TrackMate plugin for ImageJ. LogDetector algorithm was used to detect fluorescence spots; Lap Tracker algorithm was used to perform the analysis of trajectories. MSDs were computed using a custom made Matlab tool.

A.12 GRANULE MORPHOMETRIC ANALYSIS FROM TEM MICROGRAPHS.

INS-1E cells were grown on Petri dishes till confluence. For the ultra-structural analysis of insulin granules produced by cells we developed a conventional embedding procedure. Briefly INS-1E cells monolayers were fixed in a 1.5% glutaraldehyde solution in Na cacodylate buffer 0.1M pH 7.4, for 1 hour at room temperature. Next, cells were scraped, collected and centrifuged at 13200 rpm and RT for 15 minutes in the same fixative solution, until a visible pellet was obtained, and kept in new fixative solution overnight at 4°C. Then samples were post-fixed with reduced osmium tetroxide (1% OsO₄ plus 1% K₃Fe(CN)₆ in the same buffer, rinsed, stained and bloc with 3% solution of uranyl acetate in 20% ethanol, dehydrated and embedded in epoxy resin (Epon 812, Electron Microscopy Science, Hatfield, PA, USA) that was then baked for 48 hours at 60°C. For the TEM analysis, thin 90-nm sections were cut using a UC7 (Leica Microsystems, Vienna, Austria). Sections were examined with a Zeiss LIBRA 120 plus transmission electron microscope equipped with an in-column omega filter. Electron digital micrographs (2048 x 2048 16-bit) were used for the evaluation insulin granules diameter using the software Fiji.

A.13 TWO-PHOTON MICROSCOPY AND PHASOR-FLIM MEASUREMENTS.

Phasor FLIM measurements were carried out with the ISS Flimbox system (ISS, Illinois) embedded in an Olympus FluoView 1000-ASW-2.0 confocal laser microscope coupled with a two-photon Ti:sapphire laser with 80 MHz repetition rate (Chameleon Vision, Coherent). A 690 BS was used to separate excitation and emission from label free sample. NAD(P)H was excited at 710 nm and the emission was collected by using a 60x planApo water immersion objective (N.A. = 1.2) in the 400-500 nm range. Calibration of the Flimbox system was performed by measuring the known mono-exponential lifetime decay of Fluorescein at pH 11 (i.e. 4 ns upon excitation at 710 nm, collection range: 500-600 nm). A stock of 100 mM Fluorescein solution in EtOH was prepared and diluted in NaOH at pH 11 for each calibration measurement. For each measurement FLIM data are collected until about 100 counts are acquired on the average in the 256x256-pixels image. The final acquisition time was typically in the order of 1-2 minutes, depending on the signal intensity from the sample.

A.14 DATA ANALYSIS ON FLIM DATA.

The theory behind phasor FLIM has been described previously in [54]. In brief, each pixel in phasor plots is defined by coordinates g and s , calculated from the fluorescence intensity decay of each pixel of the FLIM image by using the transformations defined in [79], considering the first harmonic (i.e. 80 MHz) of the laser repetition rate. Every possible lifetime measured in samples is mapped into the phasor plot. The semi-circle depicted around phasor plot is called universal circle which represents all of the possible single exponential lifetimes which may be calculated. For a multi-exponential lifetime, within the distribution plot of the phasor the lifetimes appear as a linear combination of the expected single exponential lifetimes (NAD(P)H free and bound forms, in this case), making the plot lie inside the universal circle. All possible weighting of the two molecular species give phasors distributed along a straight line joining the phasors of the two species. In the case of three molecular species, all the possible combinations are contained in a triangle where the vertices correspond to the phasor of the pure species. For two and three component analysis of fractional NAD(P)H distribution and LLS identification we followed detailed steps reported in [79]. All phasor transformation and the data

analysis of FLIM data are performed using SimFCS v. 4 software developed at the LFD (Laboratory for Fluorescence Dynamics, Irvine, California).

A.15 CROSS-STICS ANALYSIS.

For dynamic colocalization experiments a two channels movie of 100 frames at 204 ms/frame of a portion of cytoplasm (256×256 pixel, 50 nm/pixel) of INS-1E was acquired. 561 nm laser beam was used to excite fluorescence (mCherry or Lysotracker) that was collected in one channel (600–700 nm), and in the same time backscatter signal was collected in another channel (558–564 nm). Each movie was analyzed by STICCS, using SimFCS (). The acquired movies were then analyzed according to the following workflow: 1) definition of a 32×32 pixels ROI centered on the 0,0 of the spatiotemporal correlation function. 2) Calculating the maximum value of the correlation function in the center ROI. 3) Calculating the maximum value of the correlation function outside the center ROI. 4) If the maximum value within the ROI is greater than the outside maximum value, the acquisition was evaluated as "positive" in case of dynamic colocalization; negative in the opposite case.

B

IMSD PLOT: Y-AXIS INTERCEPT AND OBJECT SIZE

B.1 INSTRUMENTAL WAIST.

A Gaussian point spread function (PSF) is defined as:

$$W(\xi, \eta, \zeta) = \frac{1}{\omega^2 \omega_z^2 (2\pi)^{3/2}} \exp \left\{ -2 \left(\frac{\xi^2 + \eta^2}{\omega^2} + \frac{\zeta^2}{\omega_z^2} \right) \right\} \quad (\text{B.1})$$

Where ω and ω_z represent the waist of the PSF along radial and axial direction, respectively. Fig. B.1 shows (left panel) the section of the PSF over the plane $\zeta = 0$ and (right panel) the profile $W(\xi, 0, 0)$. The radial waist ω is indicated as a red segment and can be regarded as the “size” of the PSF on the focal plane.

B.2 INTERCEPT OF THE *i*MSD CURVE.

$g(\xi, \eta, \zeta, \tau)$ is defined as the spatiotemporal image correlation, as function of the spatial lag-variable ξ, η, ζ and the temporal lag-variable τ . We can define the position vector $\vec{\rho} \equiv (\xi, \eta, \zeta)$ and – for point-like particles - we can express $g(\vec{\rho}, \tau)$ as:

$$g(\vec{\rho}, \tau) \propto P(\vec{\rho}, \tau) \otimes [W(\vec{\rho}) \otimes W(\vec{\rho})] \quad (\text{B.2})$$

Where $P(\vec{\rho}, \tau)$ is the probability density function of particle displacement, it depends on the investigated dynamics and determines the time evolution of g . $W(\vec{\rho})$ is the PSF and its Gaussian approximation is given in eq.(B.1). For 2D motion, g can be approximated as a Gaussian surface of variance $\sigma^2(\tau)$. Under this assumption, $P(\vec{\rho}, \tau)$ regulates the trend of $\sigma^2(\tau)$, whose boundary value $\sigma^2(0)$ is fixed by $W(\vec{\rho})$ through the radial waist of the PSF. In other words,

$$g(\vec{\rho}, 0) \propto \left\{ \frac{-\rho^2}{\sigma^2(0)} \right\} = \exp \left\{ \frac{-\rho^2}{\omega^2} \right\} \propto W(\vec{\rho}) \otimes W(\vec{\rho}) \quad (\text{B.3})$$

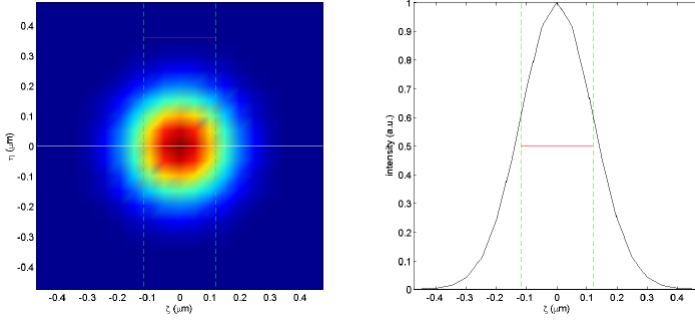


FIGURE B.1: (left) Representative PSF on the plane $\zeta = 0$ and (right) profile of the PSF along a radial direction. The red segment indicates the radial waist ω (here $\omega = 238nm$).

Eq.(B.3) can be evaluated by combining eq.(B.2) and eq.(B.1) and by considering that $P(\vec{\rho}, 0) = \delta(\vec{\rho})$, where δ is the Dirac delta function. Hence, the intercept of the $iMSD$ curve is $\sigma^2(0) = \omega^2$.

B.3 CONTRIBUTION OF THE PARTICLE SIZE.

When the particle under study has more than one fluorophore and its size is not negligible, $g(\zeta, \eta, \tau)$ must include also the spatial extension of the particle itself. If we define $S(\vec{\rho})$ as the spatial distribution of the fluorophores on the particle surface,

$$g(\vec{\rho}, \tau) \propto P(\vec{\rho}, \tau) \otimes [W_1(\vec{\rho}) \otimes W_1(\vec{\rho})] \quad (\text{B.4})$$

where

$$W_1(\vec{\rho}) = W(\vec{\rho}) \otimes S(\vec{\rho}) \quad (\text{B.5})$$

And W is the PSF. For 2D motion, we can focus on a radial profile, then generalize the solution over the (ζ, η) -plane. In this regard, by assuming a uniform distribution of the fluorophores, $S(\zeta, 0)$ can be written as:

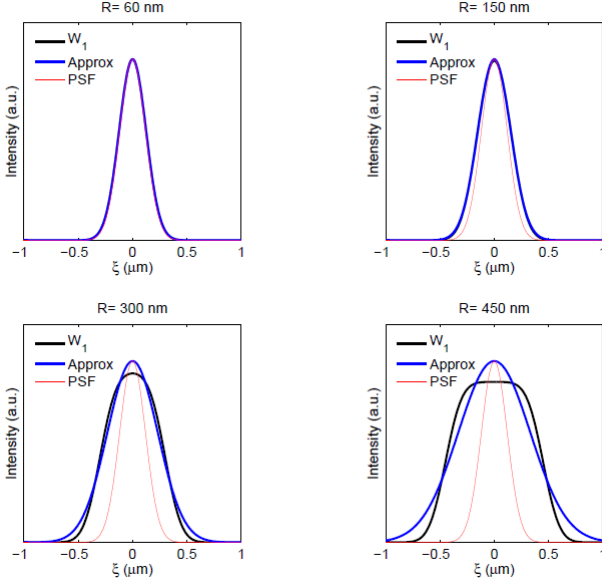


FIGURE B.2: W_1 (black lines) and corresponding Gaussian approximation (blue lines) for different R values. The red lines indicate the PSF (i.e. W).

$$S(\xi, 0) = \begin{cases} \kappa, & \text{for } |\xi| < R \\ 0, & \text{otherwise} \end{cases} \quad (\text{B.6})$$

Where R is the particle radius and κ is a constant normalization factor. By combining eq.s (B.1),(B.5) and (B.6), we obtain:

$$\begin{aligned} W_1(\xi, 0) &= W(\xi, 0) \otimes S(\xi, 0) = \\ &= \kappa \int_{-R}^R \exp\left\{-2\frac{(\xi + \xi')^2}{\omega^2}\right\} d\xi' \propto \left\{ \text{erf}\left[\frac{\sqrt{2}(\xi + R)}{\omega}\right] - \left[\frac{\sqrt{2}(\xi + R)}{\omega}\right] \right\} \end{aligned} \quad (\text{B.7})$$

Where the integral arises from the convolution of the involved functions and its analytic solution involves the error function. The last row of eq. (B.7) can be approximated by the Gaussian function:

$$W_1(\xi, 0) \propto \exp\left\{-\frac{2\xi^2}{\omega_1^2}\right\} \quad (\text{B.8})$$

In this regard, Fig. B.2 shows the analytic solution of W_1 (black lines) and the corresponding Gaussian fitting curve (blue line) for different R values. Under this approximation, the waist ω_1 is:

$$\omega_1^2 = \omega^2 + 2R^2 \quad (\text{B.9})$$

Finally, by combining eq.s (B.1), (B.8), (B.9) and evaluating g at zero time-lag, follows that the intercept of the *i*MSD curve reads $\sigma^2 = \omega_1^2$, thus the particle radius can be estimated as:

$$R^2 = \frac{\sigma^2(0) - \omega^2}{2} \quad (\text{B.10})$$

BIBLIOGRAPHY

1. Federation., I. D. *IDF Diabetes Atlas, 9th edn* 2019.
2. Hills, S. & Halban, P. A. DIAMAP: A Road Map for Diabetes Research in Europe. *Journal of Diabetes Science and Technology* **5**, 794 (2011).
3. *Pancreatic Beta Cell in Health and Disease* (eds Seino, S. & Bell, G. I.) (Springer Japan, Tokyo, 2008).
4. Pandol, S. J. *The Exocrine Pancreas* eng (Morgan & Claypool Life Sciences, San Rafael (CA), 2010).
5. Gromada, J., Franklin, I. & Wollheim, C. B. α -Cells of the Endocrine Pancreas: 35 Years of Research but the Enigma Remains. *Endocrine Reviews* **28**, 84 (2007).
6. Rorsman, P. & Huising, M. O. The somatostatin-secreting pancreatic δ -cell in health and disease. eng. *Nature Reviews. Endocrinology* **14**, 404 (2018).
7. Brereton, M. F., Vergari, E., Zhang, Q. & Clark, A. α -, δ - and PP-cells: Are They the Architectural Cornerstones of Islet Structure and Co-ordination? eng. *The Journal of Histochemistry and Cytochemistry: Official Journal of the Histochemistry Society* **63**, 575 (2015).
8. Bakhti, M., Böttcher, A. & Lickert, H. Modelling the endocrine pancreas in health and disease. *Nature Reviews Endocrinology* **15**, 155 (2019).
9. Efrat, S. & Russ, H. A. Making beta cells from adult tissues. *Trends in Endocrinology & Metabolism* **23**, 278 (2012).
10. Cnop, M., Welsh, N., Jonas, J.-C., Jorns, A., Lenzen, S. & Eizirik, D. L. Mechanisms of Pancreatic β -Cell Death in Type 1 and Type 2 Diabetes: Many Differences, Few Similarities. *Diabetes* **54**, S97 (2005).
11. Katsarou, A., Gudbjörnsdottir, S., Rawshani, A., Dabelea, D., Bonifacio, E., Anderson, B. J., Jacobsen, L. M., Schatz, D. A. & Lernmark, Å. Type 1 diabetes mellitus. *Nature Reviews Disease Primers* **3** (2017).
12. Remedi, M. S. & Emfinger, C. Pancreatic β -cell identity in diabetes. *Diabetes, Obesity and Metabolism* **18**, 110 (2016).

13. DeFronzo, R. A., Ferrannini, E., Groop, L., Henry, R. R., Herman, W. H., Holst, J. J., Hu, F. B., Kahn, C. R., Raz, I., Shulman, G. I., Simonson, D. C., Testa, M. A. & Weiss, R. Type 2 diabetes mellitus. *Nature Reviews Disease Primers* **1** (2015).
14. Kozakova, M., Morizzo, C., Goncalves, I., Natali, A., Nilsson, J. & Palombo, C. Cardiovascular organ damage in type 2 diabetes mellitus: the role of lipids and inflammation. *Cardiovascular Diabetology* **18** (2019).
15. Hou, J. C., Min, L. & Pessin, J. E. in *Vitamins & Hormones* 473 (Elsevier, 2009).
16. Suckale, J. & Solimena, M. The insulin secretory granule as a signaling hub. *Trends in Endocrinology & Metabolism* **21**, 599 (2010).
17. Li, Y. V. Zinc and insulin in pancreatic β -cells. *Endocrine* **45**, 178 (2014).
18. Tokarz, V. L., MacDonald, P. E. & Klip, A. The cell biology of systemic insulin function. *The Journal of Cell Biology* **217**, 2273 (2018).
19. Csorba, T. R. Proinsulin: Biosynthesis, conversion, assay methods and clinical studies. *Clinical Biochemistry* **24**, 447 (1991).
20. Liu, M., Hodish, I., Rhodes, C. J. & Arvan, P. Proinsulin maturation, misfolding, and proteotoxicity. *Proceedings of the National Academy of Sciences* **104**, 15841 (2007).
21. Barg, S., Huang, P., Eliasson, L., Nelson, D. J., Obermüller, S., Rorsman, P., Thévenod, F. & Renström, E. Priming of insulin granules for exocytosis by granular Cl(-) uptake and acidification. *Journal of Cell Science* **114**, 2145 (2001).
22. Orci, L., Ravazzola, M., Storch, M.-J., Anderson, R., Vassalli, J.-D. & Perrelet, A. Proteolytic maturation of insulin is a post-Golgi event which occurs in acidifying clathrin-coated secretory vesicles. *Cell* **49**, 865 (1987).
23. Davidson, H. W., Rhodes, C. J. & Hutton, J. C. Intraorganellar calcium and pH control proinsulin cleavage in the pancreatic β cell via two distinct site-specific endopeptidases. *Nature* **333**, 93 (1988).
24. Du, W., Zhou, M., Zhao, W., Cheng, D., Wang, L., Lu, J., Song, E., Feng, W., Xue, Y., Xu, P. & Xu, T. HID-1 is required for homotypic fusion of immature secretory granules during maturation. *eLife* **5** (2016).

25. Hutton, J. C. The insulin secretory granule. eng. *Diabetologia* **32**, 271 (1989).
26. Brunner, Y., Couté, Y., Iezzi, M., Foti, M., Fukuda, M., Hochstrasser, D. F., Wollheim, C. B. & Sanchez, J.-C. Proteomics Analysis of Insulin Secretory Granules. *Molecular & Cellular Proteomics* **6**, 1007 (2007).
27. Straub, S. G., Shanmugam, G. & Sharp, G. W. Stimulation of Insulin Release by Glucose Is Associated With an Increase in the Number of Docked Granules in the β -Cells of Rat Pancreatic Islets. *Diabetes* **53**, 3179 (2004).
28. Dean, P. M. Ultrastructural morphometry of the pancreatic β -cell. *Diabetologia* **9**, 115 (1973).
29. Dunn, M. F. Zinc–Ligand Interactions Modulate Assembly and Stability of the Insulin Hexamer – A Review. *BioMetals* **18**, 295 (2005).
30. Guest, P. C. in *Reviews on Biomarker Studies of Metabolic and Metabolism-Related Disorders* (ed Guest, P. C.) Series Title: Advances in Experimental Medicine and Biology, 17 (Springer International Publishing, Cham, 2019).
31. Cornu, M., Yang, J.-Y., Jaccard, E., Poussin, C., Widmann, C. & Thorens, B. Glucagon-like peptide-1 protects β -cells against apoptosis by increasing the activity of an IGF-2/IGF-1 receptor autocrine loop. eng. *Diabetes* **58**, 1816 (2009).
32. Åkesson, B., Panagiotidis, G., Westermark, P. & Lundquist, I. Islet amyloid polypeptide inhibits glucagon release and exerts a dual action on insulin release from isolated islets. *Regulatory Peptides* **111**, 55 (2003).
33. Mueckler, M. & Thorens, B. The SLC2 (GLUT) family of membrane transporters. *Molecular Aspects of Medicine* **34**, 121 (2013).
34. Matschinsky, F. M. & Wilson, D. F. The Central Role of Glucokinase in Glucose Homeostasis: A Perspective 50 Years After Demonstrating the Presence of the Enzyme in Islets of Langerhans. *Frontiers in Physiology* **10** (2019).
35. Kaufman, B. A., Li, C. & Soleimanpour, S. A. Mitochondrial regulation of β -cell function: maintaining the momentum for insulin release. eng. *Molecular Aspects of Medicine* **42**, 91 (2015).

36. Barlow, J., Solomon, T. P. J. & Affourtit, C. Pro-inflammatory cytokines attenuate glucose-stimulated insulin secretion from INS-1E insulino-ma cells by restricting mitochondrial pyruvate oxidation capacity – Novel mechanistic insight from real-time analysis of oxidative phosphorylation. *PLOS ONE* **13** (ed Kanzaki, M.) e0199505 (2018).
37. Jitrapakdee, S., Wutthisathapornchai, A., Wallace, J. C. & MacDonald, M. J. Regulation of insulin secretion: role of mitochondrial signalling. *Diabetologia* **53**, 1019 (2010).
38. Fu, Z., Gilbert, E. R. & Liu, D. Regulation of insulin synthesis and secretion and pancreatic β -cell dysfunction in diabetes. *Current Diabetes Reviews* **9**, 25 (2013).
39. Seino, S., Shibasaki, T. & Minami, K. Dynamics of insulin secretion and the clinical implications for obesity and diabetes. *Journal of Clinical Investigation* **121**, 2118 (2011).
40. Rorsman, P. & Renström, E. Insulin granule dynamics in pancreatic β cells. *Diabetologia* **46**, 1029 (2003).
41. Rorsman, P. & Braun, M. Regulation of Insulin Secretion in Human Pancreatic Islets. *Annual Review of Physiology* **75**, 155 (2013).
42. Varadi, A. Involvement of conventional kinesin in glucose-stimulated secretory granule movements and exocytosis in clonal pancreatic β -cells. *Journal of Cell Science* **115**, 4177 (2002).
43. Barg, S., Olofsson, C. S., Schriever-Abeln, J., Wendt, A., Gebre-Medhin, S., Renström, E. & Rorsman, P. Delay between Fusion Pore Opening and Peptide Release from Large Dense-Core Vesicles in Neuroendocrine Cells. *Neuron* **33**, 287 (2002).
44. Olofsson, C. S., Göpel, S. O., Barg, S., Galvanovskis, J., Ma, X., Salehi, A., Rorsman, P. & Eliasson, L. Fast insulin secretion reflects exocytosis of docked granules in mouse pancreatic B-cells. *Pflügers Archiv* **444**, 43 (2002).
45. Ohara-Imaizumi, M., Fujiwara, T., Nakamichi, Y., Okamura, T., Akimoto, Y., Kawai, J., Matsushima, S., Kawakami, H., Watanabe, T., Akagawa, K. & Nagamatsu, S. Imaging analysis reveals mechanistic differences between first- and second-phase insulin exocytosis. *Journal of Cell Biology* **177**, 695 (2007).

46. Ohara-Imaizumi, M., Nishiwaki, C., Kikuta, T., Nagai, S., Nakamichi, Y. & Nagamatsu, S. TIRF imaging of docking and fusion of single insulin granule motion in primary rat pancreatic β -cells: different behaviour of granule motion between normal and Goto-Kakizaki diabetic rat β -cells. *Biochemical Journal* **381**, 13 (2004).
47. Thurmond, D. C., Gonelle-Gispert, C., Furukawa, M., Halban, P. A. & Pessin, J. E. Glucose-Stimulated Insulin Secretion Is Coupled to the Interaction of Actin with the t-SNARE (Target Membrane Soluble N -Ethylmaleimide-Sensitive Factor Attachment Protein Receptor Protein) Complex. *Molecular Endocrinology* **17**, 732 (2003).
48. Wang, Z. & Thurmond, D. C. Mechanisms of biphasic insulin-granule exocytosis - roles of the cytoskeleton, small GTPases and SNARE proteins. *Journal of Cell Science* **122**, 893 (2009).
49. Eizirik, D. L., Colli, M. L. & Ortis, F. The role of inflammation in insulinitis and β -cell loss in type 1 diabetes. *Nature Reviews Endocrinology* **5**, 219 (2009).
50. Halban, P. A., Polonsky, K. S., Bowden, D. W., Hawkins, M. A., Ling, C., Mather, K. J., Powers, A. C., Rhodes, C. J., Sussel, L. & Weir, G. C. β -Cell Failure in Type 2 Diabetes: Postulated Mechanisms and Prospects for Prevention and Treatment. *The Journal of Clinical Endocrinology & Metabolism* **99**, 1983 (2014).
51. Zhao, Y., Hu, Q., Cheng, F., Su, N., Wang, A., Zou, Y., Hu, H., Chen, X., Zhou, H.-M., Huang, X., Yang, K., Zhu, Q., Wang, X., Yi, J., Zhu, L., Qian, X., Chen, L., Tang, Y., Loscalzo, J. & Yang, Y. SoNar, a Highly Responsive NAD⁺/NADH Sensor, Allows High-Throughput Metabolic Screening of Anti-tumor Agents. *Cell Metabolism* **21**, 777 (2015).
52. Tantama, M., Martínez-François, J. R., Mongeon, R. & Yellen, G. Imaging energy status in live cells with a fluorescent biosensor of the intracellular ATP-to-ADP ratio. *Nature Communications* **4**, 2550 (2013).
53. Patterson, G. H., Knobel, S. M., Arkhammar, P., Thastrup, O. & Piston, D. W. Separation of the glucose-stimulated cytoplasmic and mitochondrial NAD(P)H responses in pancreatic islet - cells, 5.

54. Stringari, C., Cinquin, A., Cinquin, O., Digman, M. A., Donovan, P. J. & Gratton, E. Phasor approach to fluorescence lifetime microscopy distinguishes different metabolic states of germ cells in a live tissue. *Proceedings of the National Academy of Sciences* **108**, 13582 (2011).
55. Bogan, J. S., Xu, Y. & Hao, M. Cholesterol accumulation increases insulin granule size and impairs membrane trafficking. *Traffic* **13**, 1466 (2012).
56. Fava, E., Deghany, J., Ouwendijk, J., Müller, A., Niederlein, A., Verkade, P., Meyer-Hermann, M. & Solimena, M. Novel standards in the measurement of rat insulin granules combining electron microscopy, high-content image analysis and in silico modelling. *Diabetologia* **55**, 1013 (2012).
57. Ma, L., Bindokas, V. P., Kuznetsov, A., Rhodes, C., Hays, L., Edvardson, J. M., Ueda, K., Steiner, D. F. & Philipson, L. H. Direct imaging shows that insulin granule exocytosis occurs by complete vesicle fusion. *Proceedings of the National Academy of Sciences* **101**, 9266 (2004).
58. Tabei, S. M. Intracellular transport of insulin granules is a subordinated random walk. *Proc Natl Acad Sci Usa* **110**, 4911 (2013).
59. Heaslip, A. T., Nelson, S. R., Lombardo, A. T., Previs, S. B., Armstrong, J. & Warshaw, D. M. Cytoskeletal Dependence of Insulin Granule Movement Dynamics in INS-1 β -Cells in Response to Glucose. *PLOS ONE* **9**, e109082 (2014).
60. Hoboth, P., Müller, A., Ivanova, A., Mziaut, H., Deghany, J., Sönmez, A., Lachnit, M., Meyer-Hermann, M., Kalaidzidis, Y. & Solimena, M. Aged insulin granules display reduced microtubule-dependent mobility and are disposed within actin-positive multigranular bodies. *Proceedings of the National Academy of Sciences* **112**, E667 (2015).
61. Ivarsson, R., Obermüller, S., Rutter, G. A., Galvanovskis, J. & Renström, E. Temperature-Sensitive Random Insulin Granule Diffusion is a Prerequisite for Recruiting Granules for Release: Temperature-Sensitive Insulin Granule Diffusion. *Traffic* **5**, 750 (2004).
62. Hao, M., Li, X., Rizzo, M. A., Rocheleau, J. V., Dawant, B. M. & Piston, D. W. Regulation of two insulin granule populations within the reserve pool by distinct calcium sources. *Journal of Cell Science* **118**, 5873 (2005).

63. Di Rienzo, C., Piazza, V., Gratton, E., Beltram, F. & Cardarelli, F. Probing short-range protein Brownian motion in the cytoplasm of living cells. *Nat Commun* **5**, 5891 (2014).
64. Di Rienzo, C., Gratton, E., Beltram, F. & Cardarelli, F. Fast spatiotemporal correlation spectroscopy to determine protein lateral diffusion laws in live cell membranes. *Proc Natl Acad Sci Usa* **110**, 12307 (2013).
65. Digiacomio, L., Digman, M. A., Gratton, E. & Caracciolo, G. Development of an image Mean Square Displacement (iMSD)-based method as a novel approach to study the intracellular trafficking of nanoparticles. *Acta Biomaterialia* **42**, 189 (2016).
66. Digiacomio, L. Dynamic fingerprinting of sub-cellular nanostructures by image mean square displacement analysis. *Sci Rep* **7**, 14836 (2017).
67. Marx, V. It's free imaging — label-free, that is. *Nature Methods* **16**, 1209 (2019).
68. Schaefer, P. M., Kalinina, S., Rueck, A., Arnim, C. A. F. v. & Einem, B. v. NADH Autofluorescence—A Marker on its Way to Boost Bioenergetic Research. *Cytometry Part A* **95**, 34 (2019).
69. Chance, B. & Lieberman, M. Intrinsic fluorescence emission from the cornea at low temperatures: Evidence of mitochondrial signals and their differing redox states in epithelial and endothelial sides. *Experimental Eye Research* **26**, 111 (1978).
70. Chance, B. & Baltscheffsky, H. Respiratory enzymes in oxidative phosphorylation. VII. Binding of intramitochondrial reduced pyridine nucleotide. eng. *The Journal of Biological Chemistry* **233**, 736 (1958).
71. Berezin, M. Y. & Achilefu, S. Fluorescence lifetime measurements and biological imaging. eng. *Chemical Reviews* **110**, 2641 (2010).
72. Huang, S., Heikal, A. A. & Webb, W. W. Two-Photon Fluorescence Spectroscopy and Microscopy of NAD(P)H and Flavoprotein. *Biophysical Journal* **82**, 2811 (2002).
73. Yuan, Y., Yan, Z., Miao, J., Cai, R., Zhang, M., Wang, Y., Wang, L., Dang, W., Wang, D., Xiang, D., Wang, Y., Zhang, P., Cui, Y., Bian, X. & Ma, Q. Autofluorescence of NADH is a new biomarker for sorting and characterizing cancer stem cells in human glioma. *Stem Cell Research & Therapy* **10** (2019).

74. Lakowicz, J. R., Szmajcinski, H., Nowaczyk, K. & Johnson, M. L. Fluorescence lifetime imaging of free and protein-bound NADH. eng. *Proceedings of the National Academy of Sciences of the United States of America* **89**, 1271 (1992).
75. Kierdaszuk, B., Malak, H., Gryczynski, I., Callis, P. & Lakowicz, J. R. Fluorescence of reduced nicotinamides using one- and two-photon excitation. eng. *Biophysical Chemistry* **62**, 1 (1996).
76. Meleshina, A. V., Dudenkova, V. V., Shirmanova, M. V., Shcheslavskiy, V. I., Becker, W., Bystrova, A. S., Cherkasova, E. I. & Zagaynova, E. V. Probing metabolic states of differentiating stem cells using two-photon FLIM. *Scientific Reports* **6**, 21853 (2016).
77. Buschhaus, J. M., Gibbons, A. E., Luker, K. E. & Luker, G. D. Fluorescence Lifetime Imaging of a Caspase-3 Apoptosis Reporter. eng. *Current Protocols in Cell Biology* **77**, 21.12.1 (2017).
78. Digman, M. A., Caiolfa, V. R., Zamai, M. & Gratton, E. The Phasor Approach to Fluorescence Lifetime Imaging Analysis. *Biophysical Journal* **94**, L14 (2008).
79. Ranjit, S., Malacrida, L., Jameson, D. M. & Gratton, E. Fit-free analysis of fluorescence lifetime imaging data using the phasor approach. *Nature Protocols* **13**, 1979 (2018).
80. Leben, Köhler, Radbruch, Hauser & Niesner. Systematic Enzyme Mapping of Cellular Metabolism by Phasor-Analyzed Label-Free NAD(P)H Fluorescence Lifetime Imaging. *International Journal of Molecular Sciences* **20**, 5565 (2019).
81. Stringari, C., Edwards, R. A., Pate, K. T., Waterman, M. L., Donovan, P. J. & Gratton, E. Metabolic trajectory of cellular differentiation in small intestine by Phasor Fluorescence Lifetime Microscopy of NADH. *Scientific Reports* **2** (2012).
82. Malacrida, L., Jameson, D. M. & Gratton, E. A multidimensional phasor approach reveals LAURDAN photophysics in NIH-3T3 cell membranes. *Scientific Reports* **7** (2017).
83. Gregg, T., Poudel, C., Schmidt, B. A., Dhillon, R. S., Sdao, S. M., Truchan, N. A., Baar, E. L., Fernandez, L. A., Denu, J. M., Eliceiri, K. W., Rogers, J. D., Kimple, M. E., Lammig, D. W. & Merrins, M. J. Pancreatic β -Cells From Mice Offset Age-Associated Mitochondrial

- Deficiency With Reduced K_{ATP} Channel Activity. *Diabetes* **65**, 2700 (2016).
84. Gregg, T., Sdao, S. M., Dhillon, R. S., Rensvold, J. W., Lewandowski, S. L., Pagliarini, D. J., Denu, J. M. & Merrins, M. J. Obesity-dependent CDK1 signaling stimulates mitochondrial respiration at complex I in pancreatic β -cells. *Journal of Biological Chemistry* **294**, 4656 (2019).
 85. Neuman, J. C., Schaid, M. D., Brill, A. L., Fenske, R. J., Kibbe, C. R., Fontaine, D. A., Sdao, S. M., Brar, H. K., Connors, K. M., Wienkes, H. N., Eliceiri, K. W., Merrins, M. J., Davis, D. B. & Kimple, M. E. Enriching Islet Phospholipids With Eicosapentaenoic Acid Reduces Prostaglandin E₂ Signaling and Enhances Diabetic β -Cell Function. *Diabetes* **66**, 1572 (2017).
 86. Skelin, M., Rupnik, M. & Cencič, A. Pancreatic β cell lines and their applications in diabetes mellitus research. *ALTEX - Alternatives to animal experimentation* **27**, 105 (2010).
 87. Santerre, R. F., Cook, R. A., Crisel, R. M., Sharp, J. D., Schmidt, R. J., Williams, D. C. & Wilson, C. P. Insulin synthesis in a clonal cell line of simian virus 40-transformed hamster pancreatic β -cells. *Proceedings of the National Academy of Sciences* **78**, 4339 (1981).
 88. Asfari, M., Janjic, D., Meda, P., Li, G., Halban, P. A. & Wollheim, C. B. Establishment of 2-mercaptoethanol-dependent differentiated insulin-secreting cell lines. *Endocrinology* **130**, 167 (1992).
 89. Green, A. D., Vasu, S. & Flatt, P. R. Cellular models for β -cell function and diabetes gene therapy. *Acta Physiologica* **222**, e13012 (2018).
 90. Haythorne, E., Rohm, M., van de Bunt, M., Breerton, M. F., Tarasov, A. I., Blacker, T. S., Sachse, G., Silva dos Santos, M., Terron Exposito, R., Davis, S., Baba, O., Fischer, R., Duchon, M. R., Rorsman, P., MacRae, J. I. & Ashcroft, F. M. Diabetes causes marked inhibition of mitochondrial metabolism in pancreatic β -cells. *Nature Communications* **10** (2019).
 91. Koopitwut, S. High glucose-induced impairment in insulin secretion is associated with reduction in islet glucokinase in a mouse model of susceptibility to islet dysfunction. *Journal of Molecular Endocrinology* **35**, 39 (2005).

92. Ciregia, F., Bugliani, M., Ronci, M., Giusti, L., Boldrini, C., Mazzoni, M. R., Mossuto, S., Grano, F., Cnop, M., Marselli, L., Giannaccini, G., Urbani, A., Lucacchini, A. & Marchetti, P. Palmitate-induced lipotoxicity alters acetylation of multiple proteins in clonal β cells and human pancreatic islets. *Scientific Reports* **7** (2017).
93. Bensellam, M., Laybutt, D. R. & Jonas, J.-C. The molecular mechanisms of pancreatic β -cell glucotoxicity: Recent findings and future research directions. *Molecular and Cellular Endocrinology* **364**, 1 (2012).
94. Stancill, J. S., Broniowska, K. A., Oleson, B. J., Naatz, A. & Corbett, J. A. Pancreatic β -cells detoxify H_2O_2 through the peroxiredoxin/thioredoxin antioxidant system. *Journal of Biological Chemistry* **294**, 4843 (2019).
95. Špaček, T., Šantorová, J., Zacharovová, K., Berková, Z., Hlavatá, L., Saudek, F. & Ježek, P. Glucose-stimulated insulin secretion of insulinoma INS-1E cells is associated with elevation of both respiration and mitochondrial membrane potential. *The International Journal of Biochemistry & Cell Biology* **40**, 1522 (2008).
96. Datta, R., Alfonso-García, A., Cinco, R. & Gratton, E. Fluorescence lifetime imaging of endogenous biomarker of oxidative stress. *Scientific Reports* **5** (2015).
97. Schuit, F., De Vos, A., Farfari, S., Moens, K., Pipeleers, D., Brun, T. & Prentki, M. Metabolic Fate of Glucose in Purified Islet Cells: GLUCOSE-REGULATED ANAPLEROSIS IN β CELLS. *Journal of Biological Chemistry* **272**, 18572 (1997).
98. Zhao, C., Wilson, M. C., Schuit, F., Halestrap, A. P. & Rutter, G. A. Expression and Distribution of Lactate/Monocarboxylate Transporter Isoforms in Pancreatic Islets and the Exocrine Pancreas. *Diabetes* **50**, 361 (2001).
99. Brun, T. & Maechler, P. β -cell mitochondrial carriers and the diabetogenic stress response. *Biochimica et Biophysica Acta (BBA) - Molecular Cell Research* **1863**, 2540 (2016).
100. Sekine, N., Cirulli, V., Regazzi, R., Brown, L. J., Gine, E., Tamarit-Rodriguez, J., Girotti, M., Marie, S., MacDonald, M. J. & Wollheim, C. B. Low lactate dehydrogenase and high mitochondrial glycerol phosphate dehydrogenase in pancreatic β -cells. Potential role in nutrient sensing. *The Journal of Biological Chemistry* **269**, 4895 (1994).

101. Noda, M., Yamashita, S., Takahashi, N., Eto, K., Shen, L.-M., Izumi, K., Daniel, S., Tsubamoto, Y., Nemoto, T., Iino, M., Kasai, H., Sharp, G. W. G. & Kadowaki, T. Switch to Anaerobic Glucose Metabolism with NADH Accumulation in the β -Cell Model of Mitochondrial Diabetes: CHARACTERISTICS OF β HC₉ CELLS DEFICIENT IN MITOCHONDRIAL DNA TRANSCRIPTION. *Journal of Biological Chemistry* **277**, 41817 (2002).
102. Antinozzi, P. A., Ishihara, H., Newgard, C. B. & Wollheim, C. B. Mitochondrial Metabolism Sets the Maximal Limit of Fuel-stimulated Insulin Secretion in a Model Pancreatic β Cell: A SURVEY OF FOUR FUEL SECRETAGOGUES. *Journal of Biological Chemistry* **277**, 11746 (2002).
103. Fu, J., Cui, Q., Yang, B., Hou, Y., Wang, H., Xu, Y., Wang, D., Zhang, Q. & Pi, J. The impairment of glucose-stimulated insulin secretion in pancreatic β -cells caused by prolonged glucotoxicity and lipotoxicity is associated with elevated adaptive antioxidant response. *Food and Chemical Toxicology* **100**, 161 (2017).
104. Hirst, J., King, M. S. & Pryde, K. R. The production of reactive oxygen species by complex I. *Biochemical Society Transactions* **36**, 976 (2008).
105. Roche, E., Farfari, S., Witters, L. A., Assimacopoulos-Jeannet, F., Thumelin, S., Brun, T., Corkey, B. E., Saha, A. K. & Prentki, M. Long-term exposure of β -INS cells to high glucose concentrations increases anaplerosis, lipogenesis, and lipogenic gene expression. *Diabetes* **47**, 1086 (1998).
106. Robertson, R. P. Chronic Oxidative Stress as a Central Mechanism for Glucose Toxicity in Pancreatic Islet β Cells in Diabetes. *Journal of Biological Chemistry* **279**, 42351 (2004).
107. Luo, X., Li, R. & Yan, L.-J. Roles of Pyruvate, NADH, and Mitochondrial Complex I in Redox Balance and Imbalance in β Cell Function and Dysfunction. *Journal of Diabetes Research* **2015**, 1 (2015).
108. Elson, E. L. Fluorescence Correlation Spectroscopy: Past, Present, Future. *Biophysical Journal* **101**, 2855 (2011).
109. Elson, E. L. & Magde, D. Fluorescence correlation spectroscopy. I. Conceptual basis and theory. *Biopolymers* **13**, 1 (1974).
110. Ries, J. & Schwille, P. Fluorescence correlation spectroscopy. *BioEssays* **34**, 361 (2012).

111. Rossow, M. J., Sasaki, J. M., Digman, M. A. & Gratton, E. Raster image correlation spectroscopy in live cells. *Nature protocols* **5**, 1761 (2010).
112. Kulkarni, R. P., Wu, D. D., Davis, M. E. & Fraser, S. E. Quantitating intracellular transport of polyplexes by spatio-temporal image correlation spectroscopy. *Proceedings of the National Academy of Sciences* **102**, 7523 (2005).
113. Hebert, B., Costantino, S. & Wiseman, P. W. Spatiotemporal Image Correlation Spectroscopy (STICS) Theory, Verification, and Application to Protein Velocity Mapping in Living CHO Cells. *Biophysical Journal* **88**, 3601 (2005).
114. Potvin-Trottier, L., Chen, L., Horwitz, A. R. & Wiseman, P. W. A nu-space for ICS: characterization and application to measure protein transport in live cells. *New journal of physics* **15** (2013).
115. Brown, C. M., Hebert, B., Kolin, D. L., Zareno, J., Whitmore, L., Horwitz, A. R. & Wiseman, P. W. Probing the integrin-actin linkage using high-resolution protein velocity mapping. *Journal of Cell Science* **119**, 5204 (2006).
116. Toplak, T., Pandzic, E., Chen, L., Vicente-Manzanares, M., Horwitz, A. R. & Wiseman, P. W. STICCS Reveals Matrix-Dependent Adhesion Slipping and Gripping in Migrating Cells. *Biophysical Journal* **103**, 1672 (2012).
117. Storti, B., Di Rienzo, C., Cardarelli, F., Bizzarri, R. & Beltram, F. Unveiling TRPV1 Spatio-Temporal Organization in Live Cell Membranes. *PLoS ONE* **10** (2015).
118. Durso, W., D'Autilia, F., Amodeo, R., Marchetti, L. & Cardarelli, F. Probing labeling-induced lysosome alterations in living cells by imaging-derived mean squared displacement analysis. *eng. Biochemical and biophysical research communications* **503**, 2704 (2018).
119. Martos, G., Muñoz, A. & González, J. in *Progress in Pattern Recognition, Image Analysis, Computer Vision, and Applications* (eds Hutchison, D., Kanade, T., Kittler, J., Kleinberg, J. M., Mattern, F., Mitchell, J. C., Naor, M., Nierstrasz, O., Pandu Rangan, C., Steffen, B., Sudan, M., Terzopoulos, D., Tygar, D., Vardi, M. Y., Weikum, G., Ruiz-Shulcloper, J. & Sanniti di Baja, G.) 125 (Springer Berlin Heidelberg, Berlin, Heidelberg, 2013).

120. Schubert, S., Knoch, K.-P., Ouwendijk, J., Mohammed, S., Bodrov, Y., Jäger, M., Altkrüger, A., Wegbrod, C., Adams, M. E., Kim, Y., Froehner, S. C., Jensen, O. N., Kalaidzidis, Y. & Solimena, M. β 2-Syntrophin Is a Cdk5 Substrate That Restrains the Motility of Insulin Secretory Granules. *PLoS ONE* **5** (ed Maedler, K.) e12929 (2010).
121. Nishi, M., Sanke, T., Nagamatsu, S., Bell, G. & Steiner, D. F. Islet amyloid polypeptide. A new beta cell secretory product related to islet amyloid deposits. *Journal of Biological Chemistry* (1990).
122. Hays, L. B., Wicksteed, B., Wang, Y., McCuaig, J. F., Philipson, L. H., Edwardson, J. M. & Rhodes, C. J. Intragranular targeting of syncollin, but not a syncollinGFP chimera, inhibits regulated insulin exocytosis in pancreatic β -cells. *Journal of Endocrinology* **185**, 57 (2005).
123. Caromile, L. A., Oganessian, A., Coats, S. A., Seifert, R. A. & Bowen-Pope, D. F. The Neurosecretory Vesicle Protein Phogrin Functions as a Phosphatidylinositol Phosphatase to Regulate Insulin Secretion. *Journal of Biological Chemistry* **285**, 10487 (2010).
124. Higham, C. E., Hull, R. L., Lawrie, L., Shennan, K. I. J., Morris, J. F., Birch, N. P., Docherty, K. & Clark, A. Processing of synthetic pro-islet amyloid polypeptide (proIAPP) 'amylin' by recombinant prohormone convertase enzymes, PC2 and PC3, in vitro: Pro-islet amyloid polypeptide proteolysis in vitro. *European Journal of Biochemistry* **267**, 4998 (2000).
125. Westermark, P., Andersson, A. & Westermark, G. T. Islet Amyloid Polypeptide, Islet Amyloid, and Diabetes Mellitus. *Physiological Reviews* **91**, 795 (2011).
126. Hayden, M. R. Islet amyloid, metabolic syndrome, and the natural progressive history of type 2 diabetes mellitus. eng. *JOP: Journal of the pancreas* **3**, 126 (2002).
127. Lorenzo, A., Razzaboni, B., Weir, G. C. & Yankner, B. A. Pancreatic islet cell toxicity of amylin associated with type-2 diabetes mellitus. *Nature* **368**, 756 (1994).
128. Bach, J.-P., Borta, H., Ackermann, W., Faust, F., Borchers, O. & Schrader, M. The Secretory Granule Protein Syncollin Localizes to HL-60 Cells and Neutrophils. *Journal of Histochemistry & Cytochemistry* **54**, 877 (2006).

129. Geisse, N. A., Wäsle, B., Saslowsky, D. E., Henderson, R. M. & Edwardson, J. M. Syncollin homo-oligomers associate with lipid bilayers in the form of doughnut-shaped structures. eng. *The Journal of Membrane Biology* **189**, 83 (2002).
130. Wäsle, B., Turvey, M., Larina, O., Thorn, P., Skepper, J., Morton, A. J. & Edwardson, J. M. Syncollin is required for efficient zymogen granule exocytosis. *Biochemical Journal* **385**, 721 (2005).
131. Smith, P. D., Barker, K. T., Wang, J., Lu, Y.-J., Shipley, J. & Crompton, M. R. ICAAR, a Novel Member of a New Family of Transmembrane, Tyrosine Phosphatase-like Proteins. *Biochemical and Biophysical Research Communications* **229**, 402 (1996).
132. Li, Q., Borovitskaya, A. E., DeSilva, M. G., Wasserfall, C., Maclaren, N. K., Notkins, A. L. & Lan, M. S. Autoantigens in insulin-dependent diabetes mellitus: molecular cloning and characterization of human IA-2 beta. eng. *Proceedings of the Association of American Physicians* **109**, 429 (1997).
133. Hiddinga, H. J. & Eberhardt, N. L. Intracellular Amyloidogenesis by Human Islet Amyloid Polypeptide Induces Apoptosis in COS-1 Cells. *The American Journal of Pathology* **154**, 1077 (1999).
134. Hu, Y., Nishimura, T., Zhang, A. & Notkins, A. L. Comment on: Torii et al. (2009) Gene Silencing of Phogrin Unveils Its Essential Role in Glucose-Responsive Pancreatic -Cell Growth. *Diabetes* **58**:682-692. *Diabetes* **58**, e8 (2009).
135. Ilegems, E., van Krieken, P. P., Edlund, P. K., Dicker, A., Alanentalo, T., Eriksson, M., Mandic, S., Ahlgren, U. & Berggren, P.-O. Light scattering as an intrinsic indicator for pancreatic islet cell mass and secretion. eng. *Scientific Reports* **5**, 10740 (2015).
136. Wilson, J. D., Giesselman, B. R., Mitra, S. & Foster, T. H. Lysosome-damage-induced scattering changes coincide with release of cytochrome c. *Optics Letters* **32**, 2517 (2007).
137. Rabal, H. J. & Hector J. Rabal, R. A. B. J. *Dynamic Laser Speckle and Applications*

138. Deville, S., Penjweini, R., Smisdom, N., Notelaers, K., Nelissen, I., Hooyberghs, J. & Ameloot, M. Intracellular dynamics and fate of polystyrene nanoparticles in A549 Lung epithelial cells monitored by image (cross-) correlation spectroscopy and single particle tracking. *Biochimica et Biophysica Acta (BBA) - Molecular Cell Research* **1853**, 2411 (2015).
139. Sengelaub, C. A., Navrazhina, K., Ross, J. B., Halberg, N. & Tava-zoie, S. F. PTPRN2 and PLC 1 promote metastatic breast cancer cell migration through PI(4,5)P2-dependent actin remodeling. *The EMBO Journal* **35**, 62 (2016).
140. Nicol, D. S. H. W. & Smith, L. F. Amino-Acid Sequence of Human Insulin. *Nature* **187**, 483 (1960).
141. Ghisaidoobe, A. & Chung, S. Intrinsic Tryptophan Fluorescence in the Detection and Analysis of Proteins: A Focus on Förster Resonance Energy Transfer Techniques. *International Journal of Molecular Sciences* **15**, 22518 (2014).
142. Maiti, S. Measuring Serotonin Distribution in Live Cells with Three-Photon Excitation. *Science* **275**, 530 (1997).
143. Qi, M., Barbaro, B., Wang, S., Wang, Y., Hansen, M. & Oberholzer, J. Human pancreatic islet isolation: Part I: digestion and collection of pancreatic tissue. eng. *Journal of Visualized Experiments: JoVE* (2009).
144. Cnop, M., Hughes, S. J., Igoillo-Esteve, M., Hoppa, M. B., Sayyed, F., van de Laar, L., Gunter, J. H., de Koning, E. J. P., Walls, G. V., Gray, D. W. G., Johnson, P. R. V., Hansen, B. C., Morris, J. F., Pipeleers-Marichal, M., Cnop, I. & Clark, A. The long lifespan and low turnover of human islet β cells estimated by mathematical modelling of lipofuscin accumulation. *Diabetologia* **53**, 321 (2010).
145. Koenig, J., Press, M., Grune, T. & Hoehn, A. β -cells accumulate the age-related protein aggregate lipofuscin - Impact on functionality. *Free Radical Biology and Medicine* **112**, 52 (2017).
146. Cnop, M., Igoillo-Esteve, M., Hughes, S. J., Walker, J. N., Cnop, I. & Clark, A. Longevity of human islet α - and β -cells. *Diabetes, Obesity and Metabolism* **13**, 39 (2011).
147. Moreno-García, A., Kun, A., Calero, O., Medina, M. & Calero, M. An Overview of the Role of Lipofuscin in Age-Related Neurodegeneration. eng. *Frontiers in Neuroscience* **12**, 464 (2018).

148. Rosengren, A. H., Braun, M., Mahdi, T., Andersson, S. A., Travers, M. E., Shigeto, M., Zhang, E., Almgren, P., Ladenvall, C., Axelsson, A. S., Edlund, A., Pedersen, M. G., Jonsson, A., Ramracheya, R., Tang, Y., Walker, J. N., Barrett, A., Johnson, P. R. V., Lyssenko, V., McCarthy, M. I., Groop, L., Salehi, A., Gloyn, A. L., Renstrom, E., Rorsman, P. & Eliasson, L. Reduced Insulin Exocytosis in Human Pancreatic -Cells With Gene Variants Linked to Type 2 Diabetes. *Diabetes* **61**, 1726 (2012).
149. Shaw, K. L., Pais, E., Ge, S., Hardee, C., Skelton, D., Hollis, R. P., Crooks, G. M. & Kohn, D. B. Lentiviral vectors with amplified β -cell-specific gene expression. *eng. Gene Therapy* **16**, 998 (2009).